A COMPRESSIBLE LAGRANGIAN FRAMEWORK FOR THE SIMULATION OF UNDERWATER IMPLOSION PROBLEMS

KAZEM KAMRAN

SUPERVISORS:
Prof. Eugenio Oñate
Prof. Sergio Rodolfo Idelsohn

A thesis submitted in partial fulfillment of the requirements for the degree of
Doctor of Philosophy

Departamento de Resistència de Materials i Estructures a l'Enginyeria
Escola Tècnica Superior d'Enginyers de Camins, Canals i Ports de Barcelona
Universitat Politècnica de Catalunya

Barcelona   Octobre 2012

To my parents.

ABSTRACT

The development of efficient algorithms to understand implosion dynamics presents a number of challenges. The foremost challenge is to efficiently represent the coupled compressible fluid dynamics of internal air and surrounding water. Secondly, the method must allow one to accurately detect or follow the interface between the phases. Finally, it must be capable of resolving any shock waves which may be created in air or water during the final stage of the collapse. We present a fully Lagrangian compressible numerical framework for the simulation of underwater implosion. Both air and water are considered compressible and the equations for the Lagrangian shock hydrodynamics are stabilized via a variationally consistent multiscale method [109]. A nodally perfect matched definition of the interface is used [57, 25] and then the kinetic variables, pressure and density, are duplicated at the interface level. An adaptive mesh generation procedure, which respects the interface connectivities, is applied to provide enough refinement at the interface level. This framework is then used to simulate the underwater implosion of a large cylindrical bubble, with a size in the order of *cm*. Rapid collapse and growth of the bubble occurred on very small spatial (0.3*mm*), and time (0.1*ms*) scales followed by Rayleigh-Taylor instabilities at the interface, in addition to the shock waves traveling in the fluid domains are among the phenomena that are observed in the simulation. We then extend our framework to model the underwater implosion of a cylindrical aluminum container considering a monolithic fluid-structure interaction (FSI). The aluminum cylinder, which separates the internal atmospheric-pressure air from the external high-pressure water, is modeled by a three node rotation-free shell element. The cylinder undergoes fast transient deformations, large enough to produce self-contact along it. A novel elastic frictionless contact model is used to detect contact and compute the non-penetrating forces in the discretized domain between the mid-planes of the shell. Two schemes are tested, implicit using the predictor/multi-corrector Bossak scheme, and explicit, using the forward Euler scheme. The results of the two simulations are compared with experimental data.

RESUMEN

El desarrollo de métodos eficientes para modelar la dinámica de implosión presenta varios desafíos. El primero es una representación eficaz de la dinámica del sistema acoplado de aire-agua. El segundo es que el método tiene que permitir una detección exacta o un seguimiento adecuado de la interfase entre ambas fases. Por último el método tiene que ser capaz de resolver cualquier choque que podría generar en el aire o en el agua, sobre todo en la última fase del colapso.

Nosotros presentamos un método numérico compresible y totalmente Lagrangiano para simular la implosión bajo el agua. Tanto el aire como el agua se consideran compresibles y las ecuaciones Lagrangianos para la hidrodinámica del choque se estabilizan mediante un método multiescala que es variacionalmente consistente [109]. Se

utiliza una definición de interfase que coincide perfectamente con los nodos [57, 25]. Ésta, nos facilita duplicar eficazmente las variables cinéticas como la presión y la densidad en los nodos de la interfase. Con el fin de obtener suficiente resolución alrededor de la interfase, la malla se genera de forma adaptativa y respetando la posición de la interfase. A continuación el método desarrollado se utiliza para simular la implosión bajo el agua de una burbuja cilíndrica del tamaño de un centímetro. Varios fenómenos se han capturado durante el colapso: un ciclo inmediato de colapso-crecimiento de la burbuja que ocurre en un espacio ($0.3mm$) y tiempo ($0.1ms$) bastante limitado, aparición de inestabilidades de tipo Rayleigh-Taylor en la interfase y formaron de varias ondas de choque que viajan tanto en el agua como en el aire. Después, seguimos el desarrollo del método para modelar la implosión bajo el agua de un contenedor metálico considerando una interacción monolítica de fluido y estructura. El cilindro de aluminio, que a su vez contiene aire a presión atmosférica y está rodeada de agua en alta presión, se modelando con elementos de lámina de tres nodos y sin grados de libertad de rotación. El cilindro se somete a deformaciones transitorias suficientemente rápidos y enormes hasta llegar a colapsar. Un nuevo modelo elástico de contacto sin considerar la fricción se ha desarrollado para detectar el contacto y calcular las fuerzas en el dominio discretizado entre las superficies medianas de las laminas. Dos esquemas temporales están considerados, uno es implícito utilizando el método de Bossak y otro es explícito utilizando Forward Euler. Al final los resultados de ambos casos se comparan con los resultados experimentales.

PUBLICATIONS

I   A Compressible Lagrangian framework for the simulation of the underwater implosion of large air bubbles. K. Kamran, R. Rossi, E. Oñate and S.R. Idelsohn. *Computer Methods in Applied Mechanics and Engineering*, 225(1): 210-225, March 2013. http://dx.doi.org/10.1016/j.cma.2012.11.018

II A Compressible Lagrangian framework for modeling the fluid-structure interaction in the underwater implosion of an aluminum cylinder. K. Kamran, R. Rossi, E. Oñate and S.R. Idelsohn. *Mathematical Models and Methods in Applied Sciences*, 23(2), February 2013. 10.1142/S021820251340006X

III A contact algorithm for shell problems via Delaunay-based meshing of the contact domain. K. Kamran, R. Rossi and E. Oñate, *Computational Mechanics*, September 2012. 10.1007/s00466-012-0791-x

ACKNOWLEDGMENTS

CONTENTS

LIST OF FIGURES

LIST OF TABLES

INTRODUCTION

Cavitation is normally defined as the formation of bubbles filled with vapour/ gas or their mixture and subsequent activities (such as growth, collapse and rebound) in liquids. According to the content of bubbles, cavitation can be classified as *vaporous cavitation* and *gaseous cavitation*. It is a phenomenon directly related to the pressure reduction below a certain critical value. In this way the formation of bubbles is not considered cavitation.

Usually there are two ways by which the pressure reduction is caused. One is by reduction of pressure in some zones of a fluid flow which is often referred to as *hydrodynamic cavitation*. The other is by an acoustic field, which is often referred to as *acoustic cavitation*. However, there are also other cavitations generated either by photons of laser light or by other elementary particles (e.g. protons in a bubble chamber). These cavitations are achieved in nature by local energy deposit rather than by tension in liquid. Therefore, they are often referred to as *optical cavitation* and *particle cativation*, respectively.

If pressure inside the bubble is less than the external pressure, the inrush of the momentum of the external liquid can cause considerable *condensation* of mater and energy, something that is referred to as *implosion*. Furthermore, it may happen that the inside low pressure gas is separated from the outside high pressure flow by means of a separating structure. The general expression of *underwater implosion* is used for these cases to distinguish them in the cavitation study.

In the following some applications of this phenomenon in science and engineering is presented. Although, the first studies on this field were motivated by the damages produced by the cavitation, recently some desirable applications of cavitation damage have arisen.

1.1 CAVITATION DAMAGE

Cavitaion erosion is observed over a wide range of scales and in different engineering applications. One of the most spectacular examples is the cavitation erosion sustained by the passage of a large flood through a spillway or the outlet of a dam. Turbomachines, on the other hand, constitute another field where cavitation plays a deleterious role (Figure 1.1). In certain flows of liquid through rotating machines such as pumps and turbines cavitation can not be avoided [72]. The operation of valves and nozzles may also be affected by cavitation, due to changes in the velocity of the liquid passing through them. Thus, care must be taken in the design of such instruments in order to minimize the destructive action of cavitation [9].

Figure 1.1: Cavitation damage in a propeller.

Furthermore, cavitation damage is not restricted to flows of water. Haines et al [40] have reported that intense proton beam-induced heating of the spallation neutron source mercury target will cause pressure spikes that lead to the formation of cavitation bubbles in the mercury. Erosion of the mercury container walls caused by violent collapse of bubbles could potentially limit its service lifetime. On a smaller scale, examples of cavitation damage to red blood cells in artificial heart valves are reported [137].

1.2 SONOLUMINESCENCE (SL)

Extreme physics may be observed during the process of the collapse of a bubble in a liquid. From its maximum radius to final collapse, the volume of the cavitation bubble decreases rapidly by several orders of magnitude. As the nearly adiabatic compression occurs, the pressure and temperature within the cavity reach high values and shockwaves are emitted.

In particular, If a gas bubble in water is subjected to a periodic spherical sound wave of ultrasonic frequency, the acoustic energy can be concentrated by over 12 orders of magnitude in very small volume. During the rarefaction part of the acoustic cycle the bubble absorbs energy from the sound wave, and the subsequent compressional portion of the sound field causes the collapse. The resulting excitation and heating of the gas inside the bubble may lead to UV-light emission of picoseconds duration.

SL happens in a narrow range of external parameters and is so sensitive to the test parameters. Usually the emission of light takes place when the amplitude of the sound wave exceeds the edge of SL; if the sound intensity increases further, beyond a threshold, the light is quenched. In sonoluminescence, temperatures up to 15,000 K and pressures greater than 0.37 GPa [33] have been measured in experiments, thus demonstrating the tremendous destructive potential of cavitation bubbles (Figure 1.2).

The similar phenomena, sonochemistry [118], is used in chemistry to substantially improve the chemical reactions rates. Suslick [118] truly remarks that by using conventional ultrasound equipment to drive a bubble to oscillate near its natural frequency,

> ...one can create the temperature of the sun's surface, the pressure of deep oceanic trenches, and the cooling rate of molten metal splatted onto a liquid-helium-cooled surface!
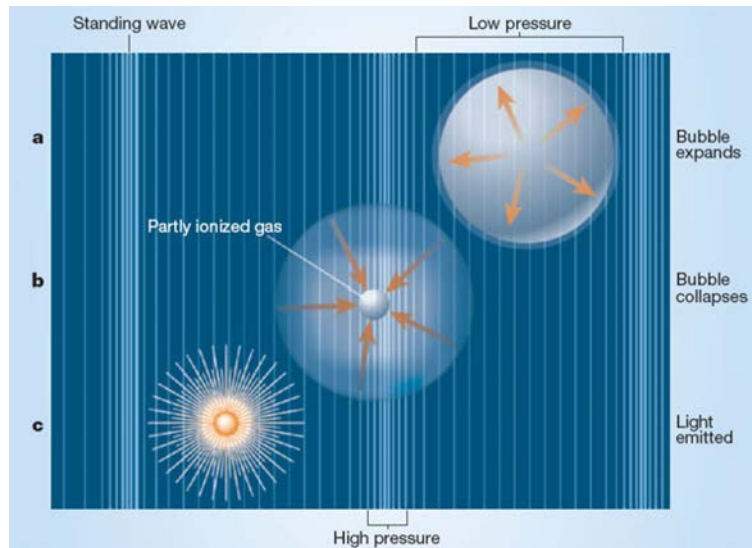
Figure 1.2: Bubble sonoluminescence. Bubbles are driven by sound waves to emit light. a) At low sound-wave pressure, a gas bubble expands until (b) an increase in pressure triggers its collapse. During collapse, temperatures can soar to 15,000 K, as it is observed from spectra of light [33] emitted from the bubble (c).Analysis of the emission spectra also provides direct evidence for the existence of a plasma inside the collapsing bubbles. [73]

1.3 BIO-MEDICAL APPLICATIONS

Several bio-medical applications use cavitation in a deliberate and controlled fashion. In dentistry, plaque is removed using an ultrasonically vibrating probe; cavitation occurring in the cooling water supply as it passes over the tip contributes to the plaque removal process. Such research has translated into the mainstream sonic toothbrush and, more recently, into its ultrasonic sibling.

In cataract surgery, the eye's natural lens is emulsified and removed in a process called phacoemulsification (Packer et al. [95]).

Bubbles also play an important role in one of the most common treatment of kidney stone; *shockwave lithotripsy* (SWL). In this method the patient is typically immersed in a water bath, while shockwaves generated underwater are focused onto the kidney stone in an attempt to break them. Current devices include electrohydraulic lithotripters, in which the shock is generated using electrodes and is focused using a reflector, electromagnetic lithotripters, in which acoustic pulses are focused using a paraboloid reflector or a lens, and piezoelectric lithotripters, which consist of an array of spherically aligned piezoelectric elements.
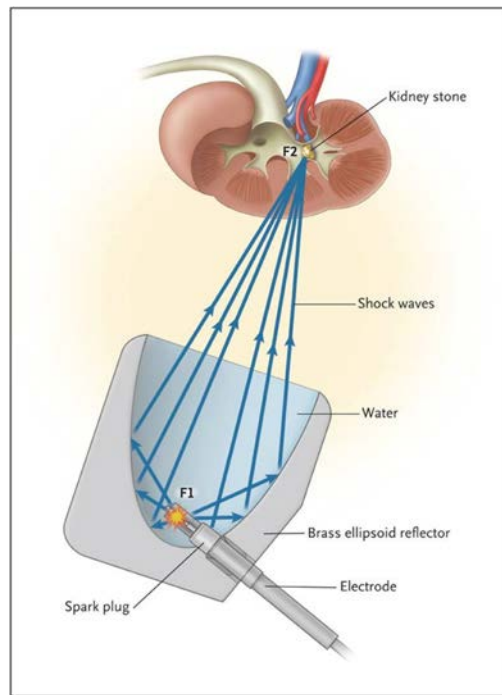
Figure 1.3: Schematic of the set-up for SWL using an electrohydraulic lithotripter [96].

A typical electrohydraulic lithotripter consists of a reflector in the shape of a truncated ellipsoid, with a sparkplug in one focus. The patient is immersed in a water bath, such that the kidney stone is located at the second focus, as shown in Figure 1.3. When the spark is generated, a shockwave propagates radially outwards, and, upon reflection, is focused onto the kidney stone. In a typical procedure, several hundreds to thousands of shockwaves are fired at a rate of approximately 0.5 Hz. As a result, the stones are broken into fragments small enough that they can be passed naturally by the human body. The main reason for the popularity of SWL is the fact that surgery is avoided altogether. In addition to kidney stones, shockwave lithotripsy has been used to treat gall stones, pancreatic stones, salivary stones and bone fracture.

The lithotripter pulse in the focal region consists of a steep compressive front followed by a long expansion tail with a tensile component (Figure 1.4). Since kidney stones are typically immersed in urine and possibly in pooled blood, this tension leads to the formation of bubbles at nuclei sites near the stone. Experimental findings suggest that the combined effect of the internal stress waves and cavitation erosion pulverizes the stones [140]; if either cavitation or the wave propagation within the stone are inhibited, the comminution efficiency decreases. Though repeated bubble collapse may lead to significant structural damage, the individual impact of bubble dynamics on stone comminution is still unclear. After the passage of a lithotripter pulse, bubbles generally gather in clusters that grow and collapse near the stone surface, thus generating shockwaves [136].

The effect of bubble clouds in SWL has been studied numerically by [121], who showed that there exists an optimal bubble population for which the damage potential is maximized, while stone shielding is minimized. A study of non-spherical bubble collapse performed by Johnsen [63] shows that shock-induced collapse has
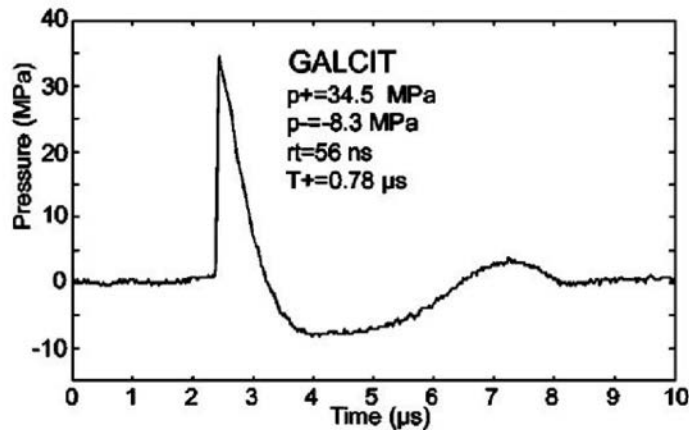
Figure 1.4: Pressure profile in the focal region of a lithotripter [63].

tremendous potential for damage not only along the stone surface, but also within kidney stones.

1.4 UNDERWATER IMPLOSION AND SUBMARINE DESIGN

Today's submarines are required to perform more specialized mission than in the past. These new missions required additional equipments that need to be either integrated into the original submarine design or mounted on the submarine hull. However, the additional equipment has a potential to fail or implode before the submarine hull since each piece of equipment has its own design constraints which may differ from those of the submarine hull.

Implodable volumes are defined as:

> any non-compensated pressure housing containing a compressible fluid at a pressure below the external ambient sea pressure (at any depth down to maximum operating depth) which has the potential to collapse [128].

Volumes external to the pressure hull, designed to maintain a static, dry, nominally one atmosphere environment within the volume for the purpose of protecting pressure-sensitive components are usually classified as implodables [128]. Examples include the Universal Modular Mast, Unmanned Undersea Vehicles (UUV) more commonly called drones, and even lighting equipment.

The number of these air-filled structures is expected to increase int he future while their potential collapse damage to nearby structures is not very well understood. The Lack of accurate understanding of the underwater explosion and implosion is shown in the work of Wardlaw [133]. It was shown that in the case of underwater explosion close enough to a structure, the physics of the problem are not only governed by the interaction of the shock and the structure, but also by the interaction between the shock reflected off the structure and the explosion bubble. As the resulting expansion wave further decreases the pressure in the region between the structure and the bubble, tensile rupture of the water is favored potentially leading to the formation of a new bubble. The subsequent collapse of this bubble can have more destructive effects than the shock induced by the explosion.

Because the collapse of implodable volumes can have devastating consequences, it is essential to improve the understanding of the underlying physics of implosion problems in order to better define design constraints for both submarine hulls and implodable volumes.

The structural failure of an implodable volume leads to the compression of the air inside. The pressure then rapidly increases to the thousand times of the initial pressure and even much greater than the hydrostatic pressure. The differential of pressures between the air and the water forces the air bubble to expand, generating a shock wave that travels throughout the water. Since the implodable volumes are usually mounted to the submarine hull, the shock waves' emission point is very close to the submarine and its strength is only slightly decreased before it reaches the submarine hull. Thus, it may be the effect of the implosion that lead to the failure of the submarine hull rather than the initial shock wave induced by the explosion.

The main characteristics of these implosion problems are first the violent nature of the phenomenon and second the strong interactions between the different mechanical systems i.e. the structures and the fluids. Furthermore, the air, water and gaseous products of explosives, interact not only with each other but also with one or more structures. Strong pressure waves travel through all media leading to large deformations of structures, in very small time scales, that may lead to failure in the form of cracks or collapse.

These violent motions of the flow occurs at the vicinity of the structure. At the same time, other regions of the flow are unperturbed. Hence, implosions form a complex system to study as they involve the strong interactions of systems with very different behaviors and in a vast range of regimes.

1.5   CURRENT WORK MOTIVATION AND THESIS OUTLINE

The main motivation of this work is to develop a compressible Lagrangian framework for the simulation of underwater implosion. In particular two problems are studied; First the collapse and growth of *cm* size cylindrical bubbles and second the underwater implosion of an aluminum cylinder.

The development of efficient algorithms to understand rapid bubble dynamics presents a number of challenges. The foremost challenge is to efficiently represent the coupled compressible fluid dynamics of internal air and surrounding water. Secondly, the method must allow one to accurately detect or follow the interface between the phases. Finally, it must be capable of resolving any shock waves which may be created in air or water during the final stage of the collapse. Chapter three, essentially, explains our suggestion "a la PFEM" for modeling of the bubble collapse.

Concerning the underwater implosion of an aluminum cylinder, the main challenges are; appropriate coupling of the fluid and structure subdomains, providing enough resolution at the zones where large deformations appear and last but not least treat the self-contact at the final stage of the collapse.

In the next chapter the dynamics of the simple bubble is reviewed. In particular, the fast dynamics of the collapse and rebound and the appearance of instabilities at the final stage of the collapse that makes the symmetric analysis invalid are highlighted. The PFEM as a powerful tool to model different physical phenomenon are presented

at the end of this chapter.

In chapter three the Euler equations that governs the fast dynamics of the inviscid flows is studied. A stabilized variational multi-scaled method developed by Scovazzi [109] is taken as the core of the compressible solver. Our main contribution in this section is to extend this solver for the two-phase flows. This is done first by introducing an interface following technique presented by Idelsohn et al [57, 25] to best follow the position of the interface distortions and second by enriching the pressure at the interface level. Large deformation of the mesh at some specific zones of the fluid necessitates the regeneration of the mesh. An adaptive mesh generation that respects the interface connectivities completed our Lagrangian compressible framework. Later various examples are solved and then the implosion of the large, *cm* size, cylindrical bubble is modeled. The appearance of the RT instabilities at the final stage of the collapse and the rupture of the bubble after a cycle of expansion and contraction are the outcomes of this study.

Chapter four is dedicated to a new contact algorithm that is developed for the shell-to-shell frictionless contact. The final stage in the implosion of closed containers usually consists of the total collapse of the containers. It is, therefor, inevitable to introduce a self-contact scheme to model the collapse. Our proposed method belongs to the contact domain methods in which the volume between the contacting bodies is discretized by a finite element mesh. A simple contact criteria is verified for each contact element to determine the active contact elements and then the contact forces are calculated. We finish this chapter by a set of examples to verify different aspects of the method.

Chapter five is dedicated to present a fully Lagrangian monolithic fluid-structure interaction scheme to solve the underwater implosion of an aluminum cylinder. The main features of this framework are the monolithic coupling of the fluid and structure subsystems, the discontinuous treatment of the pressure and density at the interface and the possibility of providing the desired mesh resolution when large displacements occur. The monolithic FSI system is solved using an implicit predictor/multi-corrector Bossak scheme at each step. An explicit forward Euler solution of this system is also provided and both results are then compared with experimental data.

All simulations are provided using the free source parallel multi-physics platform of KRATOS [24, 23] developed at CIMNE. The pre and post processing of data is provided by GID [36] software.

<div style="text-align: right; font-size: 3em;">2</div>

BUBBLE DYNAMICS

We devote this chapter to the fundamental dynamics of a growing or collapsing bubble in an infinite domain of liquid that is at rest far from the bubble . While the assumption of spherical symmetry is violated in several important processes, it is necessary to first develop this baseline.

2.1 RAYLEIGH-PLESSET EQUATION

Consider a spherical bubble of radius, $R(t)$ (where t is time), in an infinite domain of liquid whose temperature and pressure far from the bubble T_∞ and $p_\infty(t)$, respectively. The temperature, T_∞, is considered constant since temperature gradients are not considered. On the other hand, the pressure, $p_\infty(t)$, is assumed to be a known input that regulates the collapse or growth of the bubble.

Though compressibility of the liquid can be important in the context of bubble collapse, it will, for the present, be assumed that the liquid density, ρ_L, is a constant. Furthermore the dynamic viscosity, ν_L, is assumed constant and uniform. It will also be assumed that the contents of the bubble are homogeneous and that the temperature, $T_B(t)$, and pressure, $p_B(T)$, within the bubble are always uniform. These assumptions may not be justified in circumstances that will be identified as the analysis proceeds.

The radius of the bubble, $R(t)$, will be one of the primary results of the analysis. As indicated in Figure 2.1, radial position within the liquid will be denoted by the distance, r, from the center of the bubble; the pressure, $p(r,t)$, radial outward velocity, $u(r,t)$, and temperature, $T(r,t)$, within the liquid will be so designated. Conservation of mass requires that [9]

$$u(r,t) = \frac{F(t)}{r^2} \tag{2.1}$$

where $F(t)$ is related to $R(t)$ by a kinematic boundary condition at the bubble surface. In the idealized case of zero mass transport across the interface, it is clear that $u(r,t) = dR/dt$ and hence

$$F(t) = R^2 \frac{dR}{dt} \tag{2.2}$$

This is often a good approximation even when evaporation or condensation is occurring at the interface provided the vapor density is much smaller than the liquid density. Assuming a Newtonian liquid, the Navier-Stokes equation for motion in the

<div style="text-align: right;">9</div>
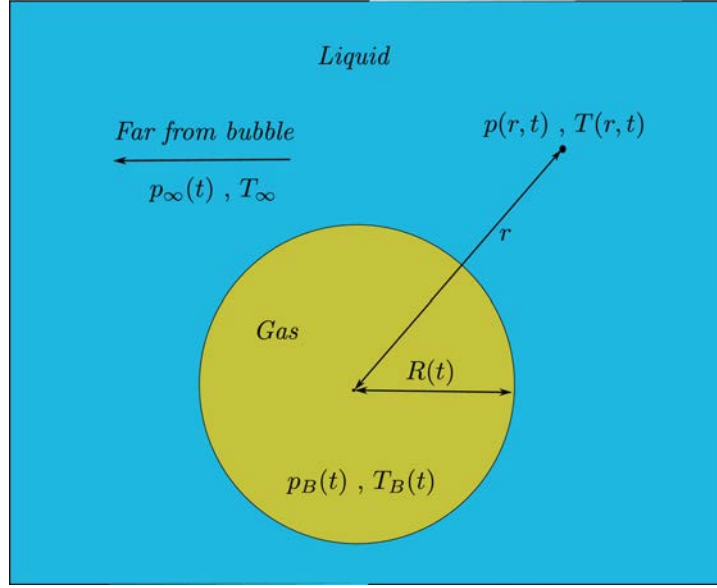
Figure 2.1: A spherical bubble in an infinite liquid.

r direction,

$$\frac{\partial u}{\partial t} + u\frac{\partial u}{\partial r} - \nu_L\left(\frac{1}{r^2}\frac{\partial}{\partial r}(r^2\frac{\partial u}{\partial r}) - \frac{2u}{r^2}\right) + \frac{1}{\rho_L}\frac{\partial p}{\partial r} = 0 \tag{2.3}$$

yield after substituting for u from $u = F(t)/r^2$:

$$\frac{1}{r^2}\frac{dF}{dt} - \frac{2F^2}{r^5} + \frac{1}{\rho_L}\frac{\partial p}{\partial r} = 0 \tag{2.4}$$

Note that the viscous terms vanish. Indeed, the only viscous contribution to the Rayleigh-Plesset equation (2.8) comes from the dynamic boundary condition at the bubble surface. Equation 2.4 can be integrated in space to give

$$\frac{1}{r}\frac{dF}{dt} - \frac{1}{2}\frac{F^2}{r^4} = \frac{p - p_\infty}{\rho_L} \tag{2.5}$$

after application of the condition $p \to p_\infty$ as $r \to r_\infty$.

To complete this part of the analysis a dynamic boundary condition on the bubble surface must be constructed. For this purpose consider a control volume consisting of a small, infinity thin lamina containing a segment of interface (Figure 2.2). The net force on this lamina in the radially outward direction per unit area is

$$(\sigma_{rr})_{r=R} + p_B - \frac{2S}{R} \tag{2.6}$$

where S is the surface tension. Since $\sigma_{rr} = -p + 2\nu_L \partial u/\partial r$, the force per unit area is

$$p_B - (p)_r = R - \frac{4\nu_L}{R}\frac{dR}{dt} - \frac{2S}{R} \tag{2.7}$$
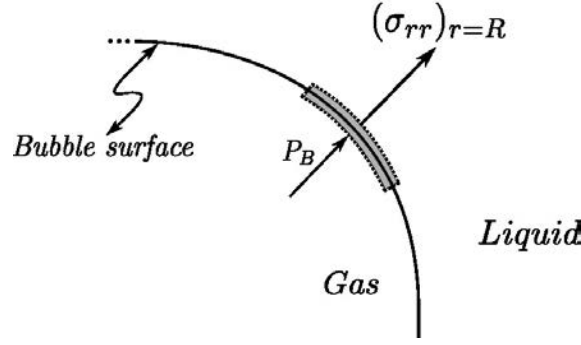
Figure 2.2: Portion of the bubble surface

In the absence of mass transport across the boundary (evaporation or condensation) this force must be zero, and substitution of the value for $p|_r = R$ from equation (2.5) with $F = R^2 dR/dt$ yields the generalized Rayleigh-Plesset equation for bubble dynamics:

$$\frac{p_B - p_\infty}{\rho_L} = \frac{d^2 R}{dt^2} R + \frac{3}{2}\left(\frac{dR}{dt}\right)^2 + \frac{4\nu}{R}\frac{dR}{dt} + \frac{2S}{\rho_L R} \tag{2.8}$$

Given $p_\infty(t)$ this represents an equation that can be solved to find $R(t)$ provided $p_B(t)$ is known. In the absence of the surface tension and the viscous terms, it was first derived and used by Rayleigh [102]. Plesset [97] first applied the equation to the problem of traveling cavitation bubbles. To be fairly general, it is assumed that the bubble contains some quantity of non-condensible gas whose partial pressure is p_{G_0} at some reference size, R_0, and temperature, T_∞. Then if there is no appreciable mass transfer of gas to or from the liquid, it follows that

$$p_B(t) = p_V(T_B) + p_{G_0}\left(\frac{T_B}{T_\infty}\right)\left(\frac{R_0}{R}\right)^3 \tag{2.9}$$

It remains to determine $T_B(t)$. This is not always necessary since the difference between the unknown T_B and the known T_∞ is negligible. But there are also circumstances in which the temperature difference is important and the effects caused by this difference dominate the bubble dynamics. It is therefore instructive to substitute equation (2.9) into (2.8) and therefore write the Rayleigh-Plesset equation in the following general form:

$$\frac{p_V(T_\infty) - p_\infty(t)}{\rho_L} + \frac{p_V(T_B) - p_V(T_\infty)}{\rho_L} + \frac{p_{G_0}}{\rho_L}\left(\frac{T_B}{T_\infty}\right)\left(\frac{R_0}{R}\right)^3$$
$$= \frac{d^2 R}{dt^2} R + \frac{3}{2}\left(\frac{dR}{dt}\right)^2 + \frac{4\nu}{R}\frac{dR}{dt} + \frac{2S}{\rho_L R} \tag{2.10}$$

2.2   GROWTH

The first term is the instantaneous tension or driving term determine by the conditions far from the bubble. The second term is the *thermal term* and very different bubble dynamics can be expected depending on the magnitude of this term. In the absence

of any significant thermal effect, the bubble dynamics behavior is termed *inertially controlled* to distinguish it from *thermally controlled*. In the latter case, the temperature in the liquid is assumed uniform and therefor the second term in the Rayleigh-Plesset equation (2.10) is zero. For simplicity, it will be assumed that the behavior of the gas in the bubble is polytropic so that

$$p_G = p_{G_0} \left(\frac{R_0}{R} \right)^{3k} \tag{2.11}$$

where *k* is approximately constant. Clearly $k = 1$ implies a constant bubble temperature and $k = \gamma$ would model adiabatic behavior. It should be understood that accurate evaluation of the behavior of the gas in the bubble requires the solution of the mass, momentum and energy equations for the bubble contents combined with appropriate boundary conditions that will include a thermal boundary condition at the bubble wall.

With these assumptions the Rayleigh-Plesset equation becomes

$$\frac{p_V(T_\infty) - p_\infty(t)}{\rho_L} + \frac{p_{G_0}}{\rho_L} \left(\frac{R_0}{R} \right)^{3k} = \frac{d^2R}{dt^2} R + \frac{3}{2} \left(\frac{dR}{dt} \right)^2 + \frac{4\nu}{R} \frac{dR}{dt} + \frac{2S}{\rho_L R} \tag{2.12}$$

Equation (2.12) without the viscous term was first derived and used by Noltingk and Neppiras [82]; the viscous term was investigated first by Poritsky [100]. Equation (2.12) can be readily integrated numerically to find $R(t)$ given the input $p_\infty(t)$, the temperature T_∞, and the other constants. In the context of cavitating flows, it is appropriate to assume that the bubble begins as a micro-bubble of radius R_0 in equilibrium at $t = 0$ at a pressure $p_\infty(0)$ so that

$$p_{G_0} = p_\infty(0) - p_V(T_\infty) + \frac{2S}{R_0} \tag{2.13}$$

and the bubble is consider at rest at $t = 0$; $dR/dt = 0$. A typical solution for equation (2.12) under these conditions is shown in figure 2.3. The bubble in this case experiences a a pressure, $p_\infty(t)$, that first decreases below $p_\infty(0)$ and then recovers to its original value. The general features of this solution are characteristic of the response of a bubble as it passes through any low pressure region; they also reflect the strong nonlinearity of equation (2.12). The growth is fairly smooth and the maximum size occurs after the minimum pressure. The collapse process is quite different. The bubble collapses catastrophically, and this is followed by successive rebounds and collapses. In the absence of dissipation mechanisms such as viscosity these rebounds would continue indefinitely without attenuation. Analytical solution to the equation (2.12) are limited to the case of a step function change in p_∞. Nevertheless, these solutions reveal some of the characteristics of more general pressure histories. Considering inviscid flow, isothermal gas behavioral and with $k = 1$ the behavior for bubble growth phase can be easily obtained. This study [9], reveals that for a constant drop of pressure in the growing phase, $p_\infty(t > 0) = p_\infty^*$ and $p_\infty^* < p_\infty(0)$, equation (2.12) shows that the asymptotic growth rate for $R \gg R_0$ is given by

$$\dot{R} \to \left[\frac{2}{3} \frac{p_V - p_\infty^*}{\rho_L} \right]^{\frac{1}{2}} \tag{2.14}$$
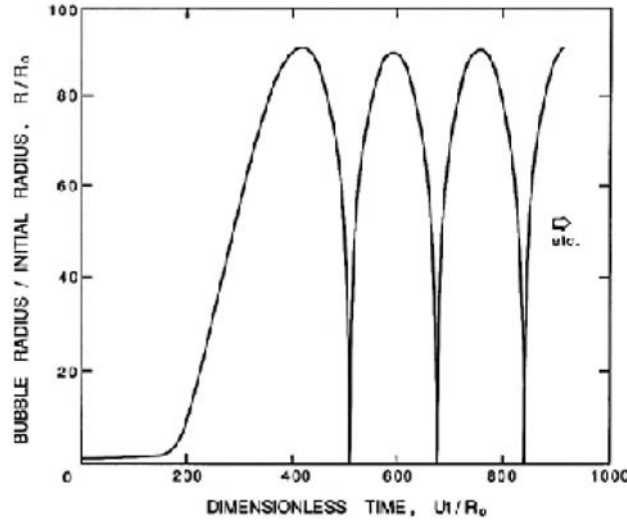
Figure 2.3: Typical solution of the Rayleigh-Plesset equation for spherical bubble size/ initial size, R/R0. The nucleus enters a low-pressure region at a dimensionless time of 0 and is convected back to the original pressure at a dimensionless time of 500. The low-pressure region is sinusoidal and symmetric about 250 [9].

Thus, following an initial period of acceleration, the velocity of the interface is relatively constant. It should be emphasized that equation (2.14) implies explosive growth of the bubble, in which the volume displacement is increasing like t^3.

2.3 COLLAPSE

In case that $R \ll R_0$, equation (2.12) yields

$$\dot{R} \to - \left(\frac{R_0}{R} \right)^{3/2} \left[\frac{2(p_\infty^* - p_V)}{3\rho_L} + \frac{2S}{\rho_L R_0} - \frac{2p_{G_0}}{3(k-1)\rho_L} \left(\frac{R_0}{R} \right)^{3(k-1)} \right]^{1/2} \tag{2.15}$$

in contrary to the growth phase, p_∞^* indicates a constant *jump* in the pressure. In the case of $k = 1$ the gas term can be simplified, however, most bubble collapse motion becomes so rapid that the gas behavior is much closer to adiabatic than isothermal and we therefore assume $k \neq 1$.

For a bubble with a substantial gas content the asymptotic collapse velocity given by equation (2.16) will not be reached and the bubble will simply oscillate about a new, but smaller, equilibrium radius. On the other hand, when the bubble contains very little gas, the inward velocity will continually increase (as $R^{-3/2}$) until the last term within the curly brackets reaches a magnitude comparable to the other terms. The collapse velocity then decreases and a minimum size given by

$$R_{min} = R_0 \left[\frac{1}{(k-1)} \frac{p_{G_0}}{p_\infty^* - p_V - p_{G_0} + 3S/R_0} \right]^{\frac{1}{3(k-1)}} \tag{2.16}$$

will be reached, following which the bubble will rebound. Note that if p_{G_0} is small R_{min} could be very small indeed. The pressure and temperature in the bubble at the minimum radius are then given by p_m and T_m where

$$p_m = p_{G_0}[(k-1)(p_\infty^* - p_V + 3S/R_0)/p_{G_0}]^{k/(k-1)} \tag{2.17}$$
$$T_m = T_0[(k-1)(p_\infty^* - p_V + 3S/R_0)/p_{G_0}] \tag{2.18}$$

The case of zero gas content presents a special albeit somewhat a hypothetical problem, since the bubble will reach zero size and at that time will have an infinite inward velocity. In the absence of both surface tension and gas content, Rayleigh (1917) was able to integrate equation (2.12) to obtain the time, t_{tc}, required for total collapse from $R = R_0$ to $R = 0$:

$$t_{tc} = 0.915 \left(\frac{\rho_L R_0^2}{p_\infty^* - p_V} \right)^{\frac{1}{2}} \tag{2.19}$$

It is important at this point to emphasize that while the results for bubble growth are quite practical, the results for bubble collapse may be quite misleading. Apart from the neglect of thermal effects, the analysis was based on two other assumptions that may be violated during the collapse:

1. The final stages of collapse may involve such high velocities (and pressures) that the assumption of liquid incompressibility is no longer appropriate.

2. It transpires that a collapsing bubble loses its spherical symmetry in ways that can have important engineering consequences.

The stability to non-spherical disturbances has been investigated from a purely hydrodynamic point of view by Birkhoff [6] and Plesset and Mitchell [98], among others. These analysis essentially examine the spherical equivalent of the Rayleigh-Taylor instability; they do not include thermal effects.

Neglecting the inertia of the gas in the bubble, then the amplitude, $a(t)$, of a spherical harmonic distortion of order n ($n > 1$) will be governed by the equation:

$$\frac{d^2a}{dt^2} + \frac{3}{R}\frac{dR}{dt}\frac{da}{dt} - \left[\frac{(n-1)}{R}\frac{d^2R}{dt^2} - (n-1)(n+1)(n+2)\frac{S}{\rho_L R^3} \right] a = 0 \tag{2.20}$$

It is clear from this equation that the most unstable circumstances occur when $\dot{R} < 0$ and $\ddot{R} >= 0$. These conditions will be met just prior to the rebound of a collapsing cavity. On the other hand the most stable circumstances occur when $\dot{R} > 0$ and $\ddot{R} < 0$, which is the case for growing bubble as they approach their maximum size. As the bubble grows the wavelength on the surface increases, and hence the growth of the amplitude is lessened. The reverse occurs during collapse. In any real scenario of the bubble growth, the initial acceleration phase for which $\ddot{R} >= 0$ and therefore vulnerable to instability, is of limited duration, so the issue will be whether or not the instability has sufficient time during the acceleration phase for significant growth to occur.

Plesset and Mitchell performed hand calculations of equation (2.20) for small n and found only minor amplification during growth. However, as can be anticipated from this equation, the amplitude may be much larger for large n. In any case, the last phase
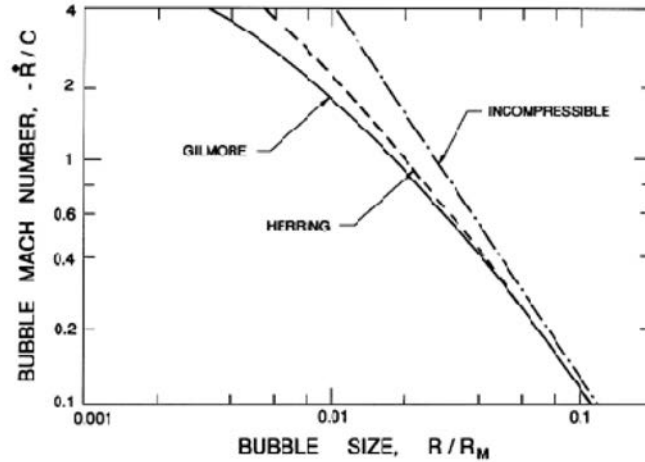
Figure 2.4: The bubble surface Mach number, $-\dot{R}/c$, plotted against the bubble radius (relative to the initial radius) for a pressure difference, $p_\infty - P_{GM}$, of 0.517 bar. Results are shown for the incompressible analysis and for the methods of Herring [45] and Gilmore [37]. Schneider's [108] numerical results closely follow Gilmore's curve up to a Mach number of 2.2 [9].

of the growth phase, in which $\dot{R} > 0$ and $\ddot{R} < 0$, is stable to all spherical harmonic perturbations. So, if inadequate time is available for growth of the perturbations during the acceleration phase, then the bubble will remain unperturbed throughout its growth.

In their experiments on underwater explosions, Reynolds and Berthoud [103] observed bubble surface instabilities during the acceleration phase that did correspond to fairly large n of the order of 10. Their bubbles become smooth again in the second, deceleration phase of growth. The bubble examined by Reynolds and Berthoud where fairly large, 2.5 *cm* to 4.5 *cm* in radius. The similar behavior has not been reported for the smaller bubbles. This could either be the result of a brief acceleration phase or the greater stabilizing effect of surface tension in smaller bubbles.

2.4 ABOUT THE BUBBLE COLLAPSE

When a cavitation bubble grows from a small nucleus to many times its original size, the collapse will begin at a maximum radius, R_M, with a very small partial pressure of gas, P_{GM}. In a typical cavitating flow, R_M is of the order of 100 times the original nuclei size, R_0. Consequently if the original partial pressure of gas inside the bubble is around 1 *bar* it would reduce to 10^{-6} *bar* at the beginning of the collapse.

Considering a pressure drop of 0.1 *bar* in the fluid, $p_\infty^* - p_V$, it follows from equation (2.17) that the maximum pressure generated during the collapse would be about 10^{10} *bar* and the maximum temperature would be 4×10^4 times the ambient temperature! Many factors including the diffusion of gas from the liquid into the bubble and the effect of liquid compressibility, mitigate this result. Nevertheless, the calculation illustrates the potential for the generation of high pressures and temperatures during collapse and the potential for the generation of shock waves and noise.

First inclusion of compressibility for low Mach number, $|dR/dt|/c$, was done by Herring [45]. The gas was considered condensible, thermal effects were neglected and therefore the pressure in the bubble remains constant. Schneider [108] and later Gilmore [37], treated the same highly idealized problem for cases in which the Mach number of collapse reaches up to 2.2. Figure 2.4 demonstrates how, in the idealized problem, the Mach number of the bubble surface increases as the bubble radius decreases. The slope is approximately $-3/2$ since $|dR/dt| \propto R^{-\frac{3}{2}}$. Note that compressibility tends to lessen the velocity of collapse.

In the absence of thermal, viscous and surface tension effects Keller and Kolodner [69] modified the RP equation (2.8) to incorporate the effects of compressibility and proposed

$$
\left(1 - \frac{1}{c}\frac{dR}{dt}\right) R \frac{d^2R}{dt^2} + \frac{3}{2}\left(1 - \frac{1}{3c}\frac{dR}{dt}\right)\left(\frac{dR}{dt}\right)^2
$$
$$
= \left(1 + \frac{1}{c}\frac{dR}{dt}\right)\frac{1}{\rho_L}[p_B - p_\infty - p_c(t + R/c)] + \frac{R}{\rho_L c}\frac{dp_B}{dt} \tag{2.21}
$$

$p_c(t)$ denotes the variable part of the pressure in the liquid at the location of the bubble center in the absence of the bubble. Other modified versions of the RP equation have been also presented and most are shown to be equivalent [101]. It has also been demonstrated that for Mach number higher than 0.3 the modification are no longer accurate and the compressible liquid field equation must be solved to obtain acceptable solution.

The primary importance of liquid compressibility is not the effect it has on the bubble dynamics, but the role it plays in the formation of shock waves during the rebounding phase that follows collapse.

Hickling and Plesset [46] were the first to make use of numerical solutions of the compressible flow equations to explore the formation of pressure waves or shock during the rebound phase. Figure 2.5 presents the variation of pressure distribution before and after the moment of minimum size. The graph on the right clearly shows the propagation of a pressure pulse or shock wave from the bubble following the minimum size. As it is indicated the pressure pulse exhibits a geometric attenuation (r^{-1}) as it propagates away from the bubble. Among many calculations carried on later, Ivany and Hammitt [61] confirmed that neither surface tension nor viscosity play a significant role in the problem. It appears that, in most cases, the pressure pulse radiated into the liquid has a peak pressure amplitude, p_P, which is given roughly by

$$
p_P \approx 100 R_M p_\infty / r \tag{2.22}
$$

This equation gives an insight on the strength of pressure pulse, which might impinge on a solid surface a few radii away. For example, a pressure pulse of 100 *bar* is to be expected at a distance $r = R_M$ and with far field liquid pressure, p_∞, of 1 *bar*. All of these analyses assumes spherical symmetry, something which may be violated during the collapse or rebound phase.
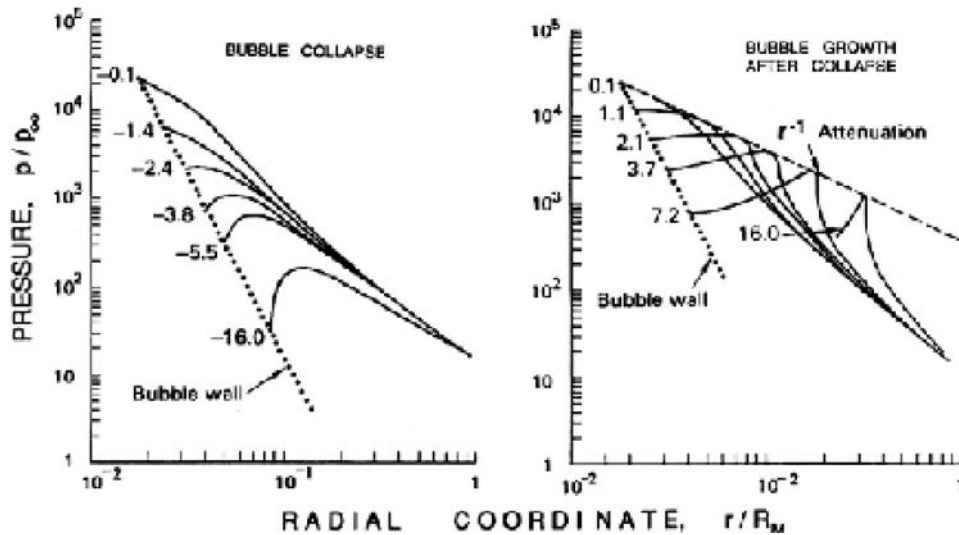
Figure 2.5: Typical results of Hickling and Plesset [46] for the pressure distributions in the liquid before collapse (left) and after collapse (right) (without viscosity or surface tension). The parameters are $p_\infty = 1$ *bar*, $\gamma = 1.4$, and the initial pressure in the bubble was 10^{-3} *bar*. The values attached to each curve are proportional to the time before or after the minimum size [9].

2.5 ESSENTIALS OF THE BUBBLE DYNAMICS

Studies on the 1D bubble dynamics, as presented up to now, suggest that for a realistic modeling of the bubble behavior following considerations are crucial:

1. Both internal air and external water have to be modeled as *compressible* to correctly represent the damped radial oscillation of the pressure wave.

2. At the final stage of the collapse *instabilities*, of both shape and surface types, appear and therefore the symmetry assumption is no more valid. Although these instabilities may appear for a very short period, they severely affect the intensity of the emitted shock waves.

3. Lack of symmetry and the possibility of the shock presence necessitate the solution of the full hydrodynamics set of equations. Challenges appear in this case are:

   - Efficiently represent the coupled compressible fluid dynamics of both phases(liquid and gas).

   - Accurately track the interface between the phases. This is important to study the instabilities that may appear.

   - Appropriately resolve any shock waves which may be created in one or both phases during the final stage of bubble implosion.

4. The initial size of the bubble and the initial external and internal pressures have crucial effects both on the bubble oscillation modes and on the shape/surface instabilities.

In this work we choose the Lagrangian description of the hydrodynamic equations for the simulation of underwater implosion. Numerical schemes in Lagrangian coordinates, by construction, are capable of precisely capturing and tracking contact discontinuities without adding any numerical dissipation. Furthermore, recent developments in Lagrangian shock hydrodynamics algorithms, *hydrocodes*, have improved the robustness of simulation with respect to mesh distortion, while maintaining second-order accuracy in smooth regions of the flow.

We close this section by referencing the Lagrangian frameworks and in particular the Particle Finite Element Method (PFEM) as one of the most renown one.

2.6   LAGRANGIAN FRAMEWORK

PFEM belongs to the family of *particle methods* in which all kinetic and kinematic informations are carried by fluid particles. Gingold [38] pioneered the first attempts in this approach to treat astrophysical hydrodynamic problems which lead to the so-called *Smooth Particle Hydrodynamics Method (SPH)* that later was generalized to fluid mechanics problem [8, 26]. Kernel approximation are used in the SPH method to interpolate the unknowns. It must be noted that the particle methods may be used with either mesh-base or meshless shape functions.

In the field of meshless methods various formulation have been developed for the fluid and structure problems. All these methods use the idea of a polynomial interpolant that fits a number of points minimizing the distance between the interpolated function and the value of the unknown point. These ideas were proposed first by Nayroles *et al* [79] which were later used by Belytschko *et al* [2] for structural problems. Oñate *et al* [90, 58] proposed the *Finite Point Method* (FPM) [90] for convection-diffusion in fluid flow problems and then generalized it by Idelsohn *et al* to the *Meshless Finite Element Method* (MFEM) [58]. MFEM uses the extended Delaunay tessellation to build a mesh combining elements of different polygonal shapes in a computing time which is linear with the number of nodal points.

PFEM treats the mesh nodes in either fluid or solid domains as particles which can freely move an even separate from the main fluid domain representing, for instance, the effect of drops (Figure 2.6). A finite element mesh connects the nodes defining the discretized domain where the governing equations are solved in the standard FEM fashion. The same elements and shape function as of the MFEM are used in the first versions of the PFEM but later standard simple elements (triangles or tetrahedra) with standard shape functions were used.

An obvious advantage of the Lagrangian formulation is that the convective terms disappear from the fluid equations, however, the difficulty is transfered to the problem of particles final positions. Indeed for large mesh motions, re-meshing may be a frequent necessity along the time solution.

In the opinion of the author, this is one of the main drawbacks of the method as it becomes quite time consuming, comparing to the solve and build, especially by the raise of massive parallel solvers. To this end and also to be able to perform real time simulation, Idelsohn *et al* [55] have recently proposed a new PFEM that liberates the need to mesh generation and indeed improve particle motion by integrating along the streamlines.

As an overview, the main properties of the PFEM can be summarized as :

a) t = 0 sec.

b) t = 0.2 sec.

c) t = 0.4 sec.

d) t = 0.6 sec.

e) t = 0.8 sec.

f) t = 1.1 sec.
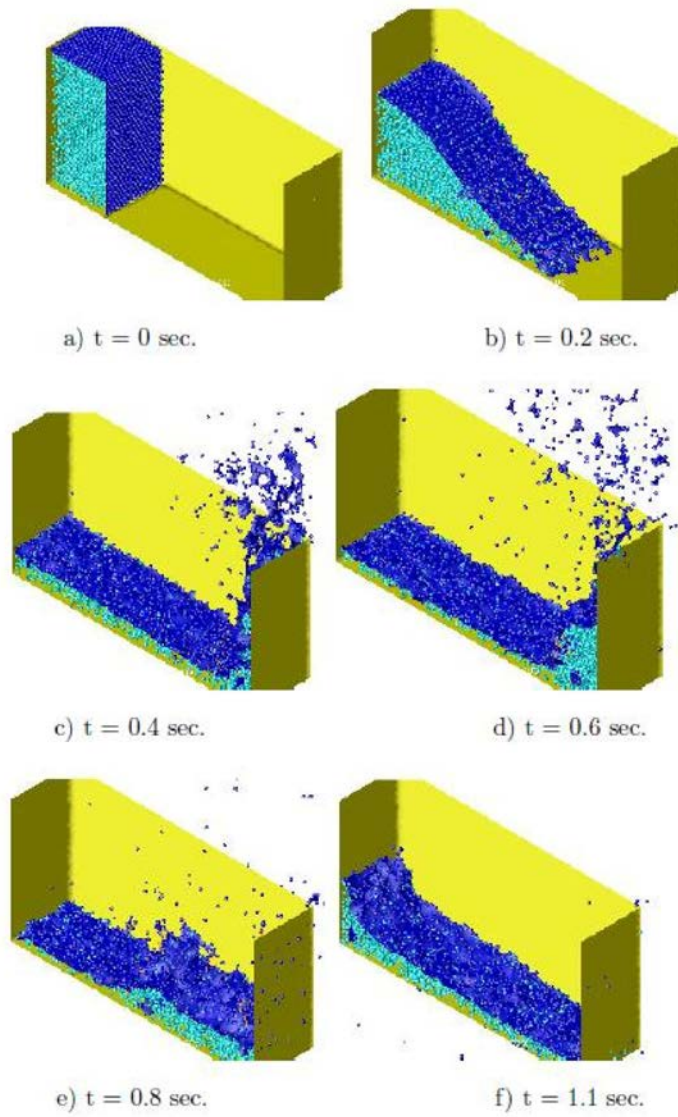
Figure 2.6: 3D dambreak modelled in the PFEM [92].
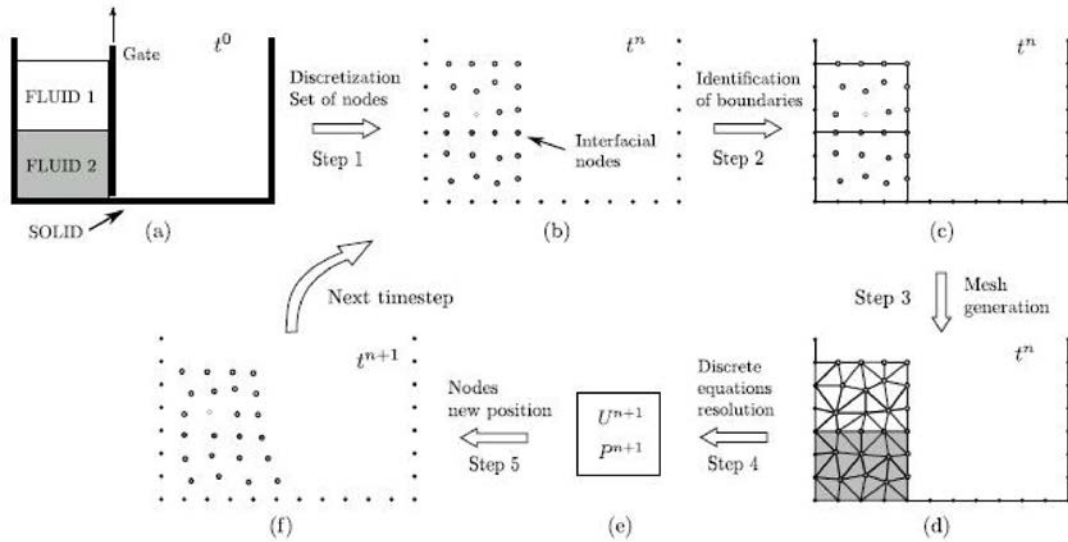
Figure 2.7: PFEM solution steps illustrated in a simple dam break example. As the gate of the dam is removed the water begins to flow. (a) Continuous problem (b) Step 1, discretization in cloud of nodes at time tn; (c) Step 2, boundary and interface recognition; (d) Step 3, mesh generation; (e) Step 4, resolution of the discrete governing equations; (f) Step 5, nodes moved to new position for time t_{n+1} [25].

1. Lagrangian description of the governing equations.

2. Particle-based discretization of the kinematic and kinetic variables.

3. Generation of the mesh and identification of the domain boundaries.

The most crucial characteristic of the PFEM and any other particle method is that there is not a specified solution domain. The domain is defined by the particle positions and hence, there is not a boundary surface or line. This is the reason why, when a differential equation is to be solved, in order to evaluate the forces, the boundary surface need to be identified to impose the boundary conditions. PFEM uses an alpha-shape technique [29], to recognize the external boundary after the triangulation or tetrahedralization of the domain. Base on this method the error in the definition of the boundary surface is proportional to the element size. Figure 2.7 depicts the various steps involves in a typical PFEM solution step. In summery a typical solution with the PFEM involves the following steps:

1. A cloud of particles, mesh nodes, that descritize all the interested media involved in the simulation is given.

2. External and internal boundaries are recognized. Exterior boundaries, if are not fixed, are obtained using the alpha-shape technique and the internal ones are marked by the interface following or capturing technique.

3. The new mesh is generated either by using the same cloud of particle as step 1 or by an enriched cloud of node interpolated upon the base cloud of particles.

4. Solution of the Lagrangian governing set of equations together with the boundary and interface conditions. It results in the updated set of nodal variables that are stored in the particles.

5. Moving the mesh nodes, particles, to the new position obtained from the solution step.

6. Go back to step 1 and repeat the solution. Note that in case of small deformations the same mesh can be used for the new step.

One of our goals in this work is to improve the current state of the art in *hyrdrocodes* for flows with large deformations. As it is already mentioned, current Lagrangian shock hydrodynamics algorithms are capable of treat cases with large distortions of the mesh but few works are able to solve highly deformed flows where the initial FEM mesh is no more suitable. The approach followed in this thesis is simply equip the hydrocodes with the adaptive mesh generating module of the PFEM and then improve it for the case of two-fluid flows by precisely following the interface and duplicating the kinetic variables at the interface level. Next chapter is devoted to the step-by-step build up of this approach.

3

GOVERNING EQUATIONS

The material of this section is taken from our paper *A Compressible Lagrangian framework for the simulation of the underwater implosion of large air bubbles* [68]. we present a fully Lagrangian shock hydrodynamics framework to solve two-phase flow problems with large distortions at the interface and big pressure and density jumps. To solve the hydrodynamic set of equations in each phase the stabilized variational multiscale method presented by Scovazzi et al [109] is adopted. Later we improve the interface detecting technique proposed by Idelsohn et al [57, 56], by conserving the interface connectivities. This method is then extended to compressible multi-fluid flows by considering a discontinuous representation of the kinetic variables, i.e. pressure and density, at the interface level. The simulation of the large-bubble implosion using the proposed framework allows to identify, to our best knowledge for the first time, the appearance of the RT instabilities in these bubbles, at the final stage of the collapse. The possibility of the appearance of such instabilities has been reported by many authors [46, 48, 7, 77, 9]. We continue the simulation during the rebounce phase till instabilities disappear and the second collapse occurs. The second collapse ends up with the rupture of the air bubble.

3.1 INTRODUCTION

As explained in the previous chapter, the underwater implosion of air-filled bubbles has been studied by many authors in the last century due to its main role in a number of phenomena in science, like sonoluminescence, sonochemistry and sonofusion and a series of applications in engineering like cavitation damages, seabed detection and structure safety in the vicinity of the imploded volumes.

Historically, the first work on the cavitation and bubble dynamic was done by Rayleigh [102], who considered the collapse of both empty and gas filled cavities in an inviscid incompressible liquid. Plesset extended his work by adding surface tension and viscous effects that resulted in the famous Rayleigh-Plesset equation [46]. The presence of high pressures in liquid near the interface in addition to the damping oscillations of the bubble lead many authors to take into account for the compressibility of the surrounding liquid in their analysis [69, 45, 101]. Depending on the initial radius of the bubble and external driving pressure two types of behavior are observed in the bubble motion, namely *weakly oscillating* and *strongly collapsing*.

In physics, violent collapse of μm size bubbles excited by the sound waves may lead to UV-light emission of picoseconds duration that is known as sonoluminescence, SL [48]. Super compression of the internal air and high velocities obtained during the final stage of the violent collapse put in doubt the stability of the bubble. Later stud-

ies on the shape stability of the bubble [99, 7] revealed that the spherical symmetry assumption can not be rigorously correct especially in the final stage of the violent collapse. Bogoyavlenskiy [7] demonstrated that time derivatives of shape perturbations grow significantly as the bubble radius vanishes. In general two different types of instabilities are prone to be excited during this stage, (i) interfacial instabilities, i.e. Rayleigh-Taylor (RT) instabilities, which occur when a gas is strongly accelerated into the liquid, and (ii) shape instabilities due the excitation of non-spherical modes causing the bubble to take on a non spherical shape. The shape instability is well shown in the DNS results provided by Nagrat et al [77] for a micron-size bubble implosion. Although they predict the RT instabilities during the very short time interval that the bubble radius is near its minimum, no numerical evidence is presented in their results.

In engineering applications, on the other hand, larger size bubbles, in the order of *cm*, are of interest. Acoustic waves emanated from broken glass spheres are used to indicate the contact of the equipment with the seabed. Orr et al [94] have reported the pressure signatures and energy-density spectra for a series of preweakend hollow glass spheres imploded at ocean depths of approximately 3 km. The signature of all implosions have many features in common. Basically each consists of a low flat negative-pulse followed by a sharp positive-pressure spike of roughly 0.2 ms duration. Different pressure signature is reported for shallow depth implosion, less than 300 m. Here linear oscillation, resembling a strongly damped sinusoid with damping factor of *e* per oscillation cycle occurs. McDonald et al [75] propose turbulent instabilities excited by the shape oscillation of the bubble as the decay mechanism in shallow depth. Recently, Turner [129] studied the influence of the structure failure on the pressure pulse. Four glass spheres of diameter 7.62 cm were imploded in a pressure vessel at a hydrostatic pressure of 6.996 MPa and the pressure-time histories were compared with numerical results obtained from different failure rates. He reported an error of 44% for models that do not account for structure failure.

The development of efficient algorithms to understand rapid bubble dynamics presents a number of challenges. The foremost challenge is to efficiently represent the coupled compressible fluid dynamics of internal air and surrounding water. Secondly, the method must allow one to accurately detect or follow the interface between the phases. Finally, it must be capable of resolving any shock waves which may be created in air or water during the final stage of the collapse. Regarding the Eulerian approach and for small bubbles, μm-size, Nagrat et al [77] proposed a DNS solution of the full hydrodynamics set of equations stabilized by the SUPG method. The interface is tracked by a modified level-set method and a DC operator is added to provide smooth transition in shock zones. Surface tension is also included to see its influence on the final shape of the bubble. Concerning large bubbles, in the order of *cm*, Farhat et al [31] solved the Euler equation for the multi-fluid problem using a ghost fluid method for the poor (GFMP) generalized for an arbitrary equation of state (EOS). Viscous effect and surface tension are neglected due to the size of the bubbles and an exact Riemann solver is used to resolve the shock at the interface.

Lagrangian frameworks to solve the Euler equations in the presence of the shock waves and with large mesh movement have been developed by different authors. Efforts have been dedicated to improve the robustness of the simulation with respect to mesh distortion, while maintaining second order accuracy in smooth regions of the

flow [109, 1, 13]. Scovazzi et al [109] developed a robust second-order FEM method with continuous linear approximation of kinematic and kinetic variables that is stabilized by operators driven from the variational multiscale paradigm. In moving Lagrangian curvilinear coordinates, traditional staggered grid hydro (SGH) methods, that use continuous linear representation for kinematic variables and discontinuous constant field for thermodynamic variables, have been extended for higher order elements [27].

All of the above mentioned Lagrangian methods are able to treat air or water phase as well as to represent shock waves in them. None of them, however, is designed to capture possible distortions of the interface that appear in multi-fluid flow. The recent developments in the Particle Finite Element Method (PFEM) [59, 92, 57, 56] to deal with multi-fluid flows provide a good basis to capture interface instabilities in the final stage of the collapse. In particular, Idelsohn et al [57, 56] successfully track the interface in an incompressible heterogeneous flows in the presence of large density and viscosity jumps. Interface is forced to match the nodes and due to the jump in pressure gradient across the interface, a discontinuous pressure gradient projection is necessary to stabilize the flow near the interface.

In the next section a review of the stabilized variational multiscale method developed by Scovazzi et al [109] to solve the Euler hydrodynamic set of equations is presented. Then, the interface-following technique proposed by Idelsohn et al [57, 56] is presented and extended for compressible flow, emphasizing on the use of a discontinuous pressure along the interface. In the final section we present some numerical examples that verify the method and show its potential for simulating the implosion of a large size cylindrical bubble.

3.2 GOVERNING EQUATIONS

3.2.1 *Euler equations*

Let us define the admissible transformation Φ, figure 3.1, from a reference configuration, $\mathbf{X}$, to the current configuration, $\mathbf{x}$, as,

$$\Phi : \mathbb{R}^{n_d} \rightarrow \mathbb{R}^{n_d}$$
$$\mathbf{X} \mapsto \mathbf{x} = \Phi(\mathbf{X}, t)$$

where n_d is the spatial dimension, the deformation gradient, $\mathbf{F}$, is defined as, $F_{iA} = \frac{\partial x_i}{\partial X_A}$, and the determinant of $\mathbf{F}$ defines the Jacobian determinant of the transformation. Conservation of mass M is expressed as,

$$0 = \frac{dM}{dt} = \frac{d}{dt}\left(\int_{\Omega_t} \rho \, d\Omega\right) = \frac{d}{dt}\left(\int_{\Omega_0} \rho J \, d\Omega_0\right) = \frac{d}{dt}\left(\int_{\Omega_0} \rho_0 \, d\Omega_0\right) \tag{3.1}$$

In the third equality we made use that for any infinitesimal volume $d\Omega$ we have, $d\Omega = J \, d\Omega_0$. As the domain Ω_0 is arbitrary and in the Lagrangian coordinate is not a function of time we have the following expression for the mass conservation,

$$\rho J = \rho_0 \tag{3.2}$$
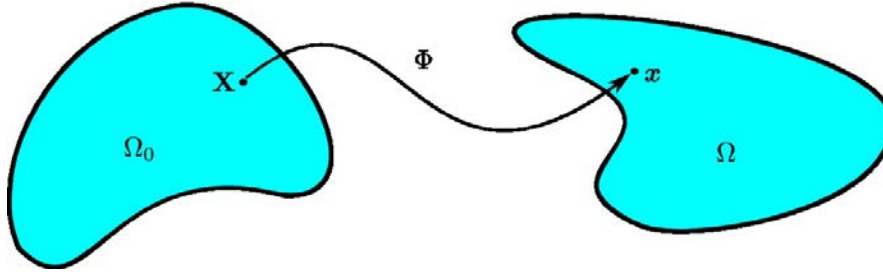
Figure 3.1: Lagrangian map Φ

Note that in the updated Lagrangian formalism Ω_0 is used for any previous configuration and not necessarily for the initial, $t = 0$, configuration.

The conservation of momentum for the arbitrary volume Ω is written as,

$$\frac{d}{dt}\left(\int_\Omega \rho\mathbf{u}\,d\Omega\right) = \int_\Omega \rho\mathbf{b}\,d\Omega + \int_S \boldsymbol{\sigma}\cdot\mathbf{n}\,dS \tag{3.3}$$

where $\mathbf{u}$ is the velocity, $\mathbf{b}$ is the body force, $\boldsymbol{\sigma}$ is the Cauchy stress tensor and $\mathbf{n}$ is the normal to the exterior surface S. Recalling the mass conservation (3.2) to evaluate the left hand side of (3.3) and applying the Gauss divergence theorem to the right hand side, we have:

$$\int_\Omega \rho\dot{\mathbf{u}}\,d\Omega = \int_\Omega (\rho\mathbf{b} + \nabla\cdot\boldsymbol{\sigma})\,d\Omega \tag{3.4}$$

for any arbitrary domain Ω which implies that,

$$\rho\dot{\mathbf{u}} = \rho\mathbf{b} + \nabla\cdot\boldsymbol{\sigma} \tag{3.5}$$

For hydrodynamic flows, shear stresses are neglected and the stress tensor $\boldsymbol{\sigma}$ is represented by the volumetric stress, i.e. pressure, p as,

$$\boldsymbol{\sigma} = -p\mathbf{I}$$

where $\mathbf{I}$ is a $n_d \times n_d$ unity tensor.

The conservation of the total energy per unit mass, E, as the sum of the internal energy, ϵ, and the kinetic energy, $\frac{1}{2}\mathbf{u}\cdot\mathbf{u}$, is written as,

$$\frac{d}{dt}\left(\int_\Omega \rho E\,d\Omega\right) = \int_\Omega \rho(\mathbf{u}\cdot\mathbf{b} + r)\,d\Omega + \int_S (\boldsymbol{\sigma}\cdot\mathbf{u} + \mathbf{q})\cdot\mathbf{n}\,dS \tag{3.6}$$

$\mathbf{u}\cdot\mathbf{b}$ is the specific power due to body forces, r is the specific rate of internal energy production, the power added due to to the surface work of surface tensions are included by $\boldsymbol{\sigma}\cdot\mathbf{u}$ and the transfered heat by the heat flux $\mathbf{q}$. The same procedure as the one applied for the momentum conservation is exploited to obtain the following conservative form of the energy equation,

$$\rho\dot{E} = \rho(\dot{\epsilon} + \dot{\mathbf{u}}\cdot\mathbf{u}) = -\nabla\cdot(p\mathbf{u} + \mathbf{q}) + \rho\mathbf{b}\cdot\mathbf{u} + \rho r \tag{3.7}$$

Note that $\boldsymbol{\sigma}$ is replaced by $-p\mathbf{I}$.

A *non-conservative* form of the energy equation can be obtained by multiplying the momentum equation (3.5) by **u** and use to simplify the conservative form (3.7) to obtain,

$$\rho\dot{\epsilon} + p\nabla\cdot\mathbf{u} = \nabla\cdot\mathbf{q} + \rho r \tag{3.8}$$

3.2.2 Lagrangian hydrodynamic equations

Underwater implosions result in bubbles whose characteristic size is considerably larger than that of bubbles obtained in liquid suspensions. Hence such bubbles are less affected by surface tension and viscous forces and therefore their dynamics can be modeled by the Euler equations:

$$
\begin{aligned}
\rho J &= \rho_0 \\
\rho\dot{\mathbf{u}} + \nabla_x p &= \mathbf{b} \qquad \text{in } \Omega, \ t \in]0, T[\\
\rho\dot{\epsilon} + p\nabla_x\cdot\mathbf{u} &= \nabla_x\cdot\mathbf{q} + \rho r \qquad \text{in } \Omega, \ t \in]0, T[
\end{aligned}
\tag{3.9}
$$

The gradient derivatives, ∇_x, are calculated in the current configuration and $\dot{(\ )}$ refers to the material time derivative. J is the deformation Jacobian determinant, ρ_0 is the reference density, ρ is the current density, **u** is the velocity vector, **b** is the body force, p is the thermodynamic pressure, r is the energy source term, **q** is the heat flux and ϵ is the internal energy per unit mass. Although the energy equation is not written in the conservative form it can still be used to develop a globally conservative variational formulation [109].

For the sake of simplicity and without loss of generality, a homogeneous Dirichlet boundary condition is considered. These equations and the boundary conditions, in addition to an equation of state for the pressure p and a constitutive law for the heat flux, q, together with the appropriate initial conditions define the evolution of the system.

We use the Mie-Grüneisen equation of state (EOS) that is widely used in today's hydro-codes to model real materials such as compressible ideal gases, co-volume gases, high explosives, elasto-plastic solids with negligible shear strength etc [111, 113, 132, 76]. The hydrostatic pressure, p, is then related to the density, ρ, and internal energy, ϵ, as the following,

$$p = \hat{p}(\rho, \epsilon) = f_1(\rho) + f_2(\rho)\epsilon. \tag{3.10}$$

where f_1 and f_2 are known from the reference thermodynamic state of the system. Ideal gases, as an example, can be expressed using equation of state (3.10) if $f_1 = 0.0$ and $f_2 = (\gamma - 1)\rho$. Note that another equivalent of (3.10) can be written for the internal energy, ϵ, as, $\epsilon = \hat{\epsilon}(\rho, p)$. In this case the differentiation of ϵ is computed as,

$$d\epsilon = \left.\frac{\partial\epsilon}{\partial\rho}\right|_p d\rho + \left.\frac{\partial\epsilon}{\partial p}\right|_\rho dp \tag{3.11}$$

By considering (3.11) and recalling the differential form of the conservation of mass, $\dot{\rho} + \rho \nabla \cdot \mathbf{u} = 0$, the energy equation (3.8) can be rewritten as,

$$
\begin{aligned}
0 &= \rho \dot{\epsilon} + p \nabla \cdot \mathbf{u} \\
&= \rho \left. \frac{\partial \epsilon}{\partial \rho} \right|_p \dot{\rho} + \rho \left. \frac{\partial \epsilon}{\partial p} \right|_\rho \dot{p} + p \nabla \cdot \mathbf{u} \\
&= \rho \left. \frac{\partial \epsilon}{\partial p} \right|_\rho \left(\dot{p} + \frac{\frac{p}{\rho} - \rho \left. \frac{\partial \epsilon}{\partial \rho} \right|_p}{\left. \frac{\partial \epsilon}{\partial p} \right|_\rho} \nabla \cdot \mathbf{u} \right)
\end{aligned}
\tag{3.12}
$$

For a general compressible flow $\rho \, \partial_p \, \epsilon|_\rho \neq 0$. It is possible to further simplify the previous equations. First note that, by standard calculus derivations,

$$
\left(\left. \frac{\partial \epsilon}{\partial p} \right|_\rho \right)^{-1} = \left. \frac{\partial p}{\partial \epsilon} \right|_\rho .
\tag{3.13}
$$

Second, by the combination of the first and second law of thermodynamics, i.e. Gibbs identity, we have, $d\epsilon - p/\rho^2 d\rho = T d\eta$. Where T is temperature and η is the entropy per unit mass. For a constant entropy we have,

$$
\frac{p}{\rho} = \rho \left. \frac{\partial \epsilon}{\partial \rho} \right|_\eta
\tag{3.14}
$$

The multiplying factor in the last term of equation (3.12), can be rewritten using (3.13) and (3.14) as,

$$
\frac{\frac{p}{\rho} - \rho \left. \frac{\partial \epsilon}{\partial \rho} \right|_p}{\left. \frac{\partial \epsilon}{\partial p} \right|_\rho} = \rho \left. \frac{\partial p}{\partial \epsilon} \right|_\rho \left(\left. \frac{\partial \epsilon}{\partial \rho} \right|_\eta - \left. \frac{\partial \epsilon}{\partial \rho} \right|_p \right).
\tag{3.15}
$$

Recalling the EOS of the form $p = \hat{p}(\rho, \epsilon)$, we have:

$$
dp = \left. \frac{\partial p}{\partial \rho} \right|_\epsilon d\rho + \left. \frac{\partial p}{\partial \epsilon} \right|_\rho d\epsilon
\tag{3.16}
$$

that for the the constant pressure leads to,

$$
0 = \left. \frac{\partial p}{\partial \rho} \right|_p = \left. \frac{\partial p}{\partial \rho} \right|_\epsilon + \left. \frac{\partial p}{\partial \epsilon} \right|_\rho \left. \frac{\partial \epsilon}{\partial \rho} \right|_p .
\tag{3.17}
$$

Substituting (3.17) into (3.15) yields

$$
\begin{aligned}
\frac{\frac{p}{\rho} - \rho \frac{\partial \epsilon}{\partial \rho}\big|_p}{\frac{\partial \epsilon}{\partial p}\big|_\rho} &= \rho \left(\frac{\partial p}{\partial \epsilon}\Big|_\rho \frac{\partial \epsilon}{\partial \rho}\Big|_\eta - \frac{\partial p}{\partial \epsilon}\Big|_\rho \frac{\partial \epsilon}{\partial \rho}\Big|_p \right) \\
&= \rho \left(\frac{\partial p}{\partial \epsilon}\Big|_\rho \frac{\partial \epsilon}{\partial \rho}\Big|_\eta + \frac{\partial p}{\partial \rho}\Big|_\epsilon \right) \\
&= \rho \frac{\partial p}{\partial \rho}\Big|_\eta \\
&= \rho c_s^2,
\end{aligned}
\tag{3.18}
$$

where c_s is the isentropic speed of sound in the medium. Hence (3.12) reduces to,

$$
0 = \rho \frac{\partial \epsilon}{\partial p}\Big|_\rho \left(\dot{p} + \rho c_s^2 \nabla_x \cdot \mathbf{u} \right).
\tag{3.19}
$$

The term $\rho \partial_p \epsilon|_\rho \neq 0$ can be simplified in (3.19), and the momentum and energy equations can be combined into the mixed, first order system form of a nonlinear wave equation in $\mathbf{u}$ and p as,

$$
\begin{aligned}
\rho \dot{\mathbf{u}} + \nabla_x p &= 0 \\
\dot{p} + \rho c_s^2 \nabla_x \cdot \mathbf{u} &= 0.
\end{aligned}
\tag{3.20}
$$

We recognize here the relation between $\partial_p \epsilon|_\rho$ and the Grüneisen parameter [76], defined as

$$
\Gamma = \frac{1}{\rho \frac{\partial \epsilon}{\partial p}\big|_\rho} = \frac{1}{\rho} \frac{\partial p}{\partial \epsilon}\Big|_\rho.
\tag{3.21}
$$

The thermodynamic parameter Γ varies only mildly with the thermodynamic state of a fluid system, unless phase transition occur [76]. In the case of an ideal gas satisfying a γ-law EOS, it is easy to drive $\Gamma = 1 - \gamma = cte$.

As the hydrodynamic equations (5.1) are quite nonlinear, we first develop the stabilized variational multiscale form of the *linearized* version of these equations, (3.20). Such *linearized* problem is presented in the next section.

3.2.3 *Stabilization of the* linearized *form*

The linearization is done considering a small-strain approximation in which the derivatives in the reference and current configurations coincide and the solution of the thermodynamic variables, density, pressure and internal energy, is considered as a small perturbation to the constant reference state;

$$
\begin{aligned}
\rho &= \bar{\rho} + \tilde{\rho}, \quad \bar{\rho} = \text{const.}, \quad \tilde{\rho} \ll 1, \tag{3.22} \\
p &= \bar{p} + \tilde{p}, \quad \bar{p} = \text{const.}, \quad \tilde{p} \ll 1, \tag{3.23} \\
c_s &= \bar{c}_s + \tilde{c}_s, \quad \bar{c}_s = \text{const.}, \quad \tilde{c}_s \ll 1. \tag{3.24}
\end{aligned}
$$
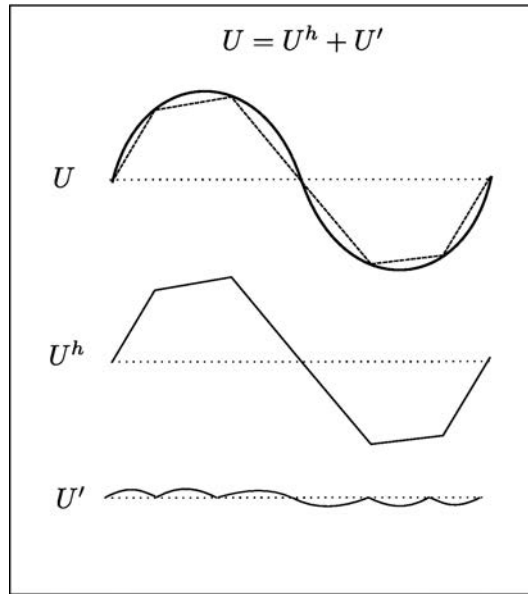
Figure 3.2: Solution, U, is devided to two parts: coarse scale, U^h, captured by the FEM and fine scale U'.

As the result, the conservation of mass decouples from the momentum and energy equations and we can focus on these equations (3.20) with *constant* coefficients to develop the variational multiscale form.

In the absence of source terms and with homogeneous Dirichlet boundary conditions the equivalent variational form of the linearized equations (3.20) is read as, find $\mathbf{u} \in \mathbf{V}_u$ and $p \in V_p$ such that for all test functions $\mathbf{v} \in \mathbf{V}_u$ and $q \in V_p$,

$$
\begin{aligned}
(\rho\dot{\mathbf{u}}, \mathbf{v}) - (p, \nabla \cdot \mathbf{v}) &= 0 \\
(\dot{p} + \rho c_s^2 \nabla_x \cdot \mathbf{u}, q) &= 0.
\end{aligned}
\tag{3.25}
$$

Here the appropriate space for velocity is $\mathbf{V}_u = C^0([0,T], H_0(div, \Omega)) \cap C^1([0,T], \mathbf{L}^2(\Omega))$ and for pressure is $V_p = C^1([0,T], \mathbf{L}^2(\Omega))$. By $C^k([0,T],.)$ we mean all functions that are k continuous in a time interval $[0,T]$ and $H_0(div, \Omega)$ is the space of functions in $L^2(\Omega)$ with their derivatives also in $L^2(\Omega)$ and with zero support in the boundary.

We consider a decomposition of the unknowns to the *coarse* and *fine* scales where the *coarse* scale solution is captured by the finite element and the *fine* scale is approximated by the coarse scale residual in a consistent way [50, 52], figure 3.2. The decomposition has the form,

$$
\begin{aligned}
\mathbf{u} &= \mathbf{u}^h + \mathbf{u}' \\
p &= p^h + p'.
\end{aligned}
$$

The same structure is used for the test function decomposition. Piece-wise linear polynomials for both velocity and pressure are considered to build a C^0 continuous ap-

proximation of the test and trial functions over the domain. Equations (3.25) tested by the coarse scale test functions reduce to

$$
\begin{aligned}
&(\rho(\dot{\mathbf{u}}^h + \dot{\mathbf{u}}'), \mathbf{v}_h) - (p^h + p', \nabla \cdot \mathbf{v}^h) = 0 \\
&(\dot{p}^h + \dot{p}' + \rho c_s^2 \nabla_x \cdot \mathbf{u}^h, q^h) + (\rho c_s^2 \nabla_x \cdot \mathbf{u}', q^h) = 0.
\end{aligned}
\tag{3.26}
$$

Some well known simplifications in the context of the variational multiscale approach [50, 52] are considered as follows,

1. Fine scales are considered *quasi-static* and as a consequence their time derivatives are neglected in comparison to the time derivatives of the coarse scales. This implies that the fine scales adjust instantaneously to complement the coarse scales.

2. For smooth flows or at least smooth regions of the flow one expect continuous solutions. Therefore the fine scales, similarly as the coarse ones, are considered at least continuous in the entire domain. As a result inter-element fluxes are automatically canceled.

3. No contribution of the fine scales is considered on the exterior boundaries.

Integrating by part the last term of equations (3.26) and considering the previous assumptions, the *coarse scale equations* (3.26) reduce to,

$$
\begin{aligned}
&(\rho \dot{\mathbf{u}}^h, \mathbf{v}^h) - (p^h + p', \nabla \cdot \mathbf{v}^h) = 0 \\
&(\dot{p}^h + \rho c_s^2 \nabla_x \cdot \mathbf{u}^h, q^h) - (\rho c_s^2 \mathbf{u}', \nabla_x q^h) = 0.
\end{aligned}
\tag{3.27}
$$

Fine scales $\mathbf{u}', p'$ in the *coarse scale equations* (3.27) are obtained by testing equations (3.25) this time by the fine scale test functions, that is,

$$
\begin{aligned}
&(\rho \dot{\mathbf{u}}', \mathbf{v}') - (p', \nabla \cdot \mathbf{v}') = - < \mathcal{R}_{\mathbf{u}}^h, \mathbf{v}' > \\
&(\dot{p}' + \rho c_s^2 \nabla_x \cdot \mathbf{u}', q') = - < \mathcal{R}_{p}^h, q' > .
\end{aligned}
\tag{3.28}
$$

$\mathcal{R}_{\mathbf{u}}^h$ and $\mathcal{R}_{p}^h$ are residuals of the momentum and energy equations, respectively and are obtained considering the same assumptions mentioned above. They have the following forms

$$
\begin{aligned}
\mathcal{R}_{\mathbf{u}}^h &:= \rho \dot{\mathbf{u}}^h + \nabla_x p^h \\
\mathcal{R}_{p}^h &:= \dot{p}^h + \rho c_s^2 \nabla_x \cdot \mathbf{u}^h.
\end{aligned}
\tag{3.29}
$$

Fixing $\mathbf{v}'$ and q', the left sides of the equations (3.28) can be seen as complicated operators of the fine scales acting on $\mathbf{v}'$ and q'. In this case and by means of the Riesz Representation theorem [83], residuals introduced in equation (3.29) can be identified as the Riesz candidates for these operators and therefore it is guaranteed that $\mathcal{R}_{\mathbf{u}}^h$ and $\mathcal{R}_{p}^h$ belong to the space of $\mathbf{v}'$ and q', respectively.

As the exact solution of the fine scale equations (3.28) is expensive and even unnecessary, one simple way to approximate subscales would be through residuals (3.29) as (see [18, 42] and references therein for the similar approach),

$$
\begin{aligned}
\mathbf{u}' &= -\tau \frac{1}{\rho} \mathcal{R}_{\mathbf{u}}^h \\
p' &= -\tau \, \mathcal{R}_p^h
\end{aligned}
\tag{3.30}
$$

where τ has dimension of time.

This seems to be the simplest approach because subscale approximations are completely decoupled one from another. Consequently, the time derivative terms in equations (3.28) are dominant and so only their discrete inverse $\tau \frac{1}{\rho}$ and τ are used to scale the residuals $\mathcal{R}_{\mathbf{u}}^h$, $\mathcal{R}_p^h$ respectively.

Inserting the preceding approximations (3.30) into the coarse scale equations (3.27) the final stabilized form of the linearized acoustic problem is:

$$
(\rho \dot{\mathbf{u}}^h, \mathbf{v}^h) - (p^h, \nabla_x \cdot \mathbf{v}^h) + (\dot{p}^h + \rho c_s^2 \nabla_x \cdot \mathbf{u}^h, \nabla_x \cdot \mathbf{v}^h)_\tau = 0
$$
$$
\tag{3.31}
$$
$$
(\dot{p}^h + \rho c_s^2 \nabla_x \cdot \mathbf{u}^h, q^h) + (c_s^2(\rho \dot{\mathbf{u}}^h + \nabla_x p^h), \nabla_x q^h)_\tau = 0.
$$

The main stabilization effect comes from an incomplete Laplacian of the velocity,

$$
(\nabla_x \cdot \mathbf{u}^h, \nabla_x \cdot \mathbf{v}^h)_{\tau c_s^2},
$$

in the momentum equation and a full Laplacian of the pressure,

$$
(\nabla_x p^h, \nabla_x q^h)_{\tau c_s^2},
$$

in the energy equation. In addition, the presence of the full residual avoids reduction in accuracy order, which is quite common in residually inconsistent stabilizations.

A similar set of stabilized equations can be obtained using the Finite Calculus (FIC) approach [85, 86].

In the following section we present the full stabilization for the *nonlinear* case, inspired in the *linearized* one previously mentioned.

3.2.4   *Stabilization of the* nonlinear *form*

The variational multiscale stabilization of the *linearized* case reveals the overall structure of the stabilization method. To elaborate the variational multiscale stabilization of the *nonlinear* form, first the variational equivalence of the hydrodynamic set of equations (5.1) is presented. We consider homogeneous Dirichlet boundary conditions and

r, **q** and b are set to zero. We are interested in finding $\mathbf{u} \in \mathbf{V}_u$ and $p, \rho, \epsilon \in V_p$ such that, $\forall \mathbf{v} \in \mathbf{V}_u$ and $\forall q \in V_p$

$$\int_{\Omega_0} q \, (\rho_0 - \rho J) \, d\Omega_0 = 0 \tag{3.32a}$$

$$\int_\Omega \mathbf{v} \cdot (\rho \, \dot{\mathbf{u}}) \, d\Omega + \int_\Omega \boldsymbol{\sigma} : \nabla^s_x \mathbf{v} \, d\Omega = 0 \tag{3.32b}$$

$$\int_\Omega q \, (\rho \, \dot{\epsilon} - \boldsymbol{\sigma} : \nabla^s_x \mathbf{u}) \, d\Omega = 0. \tag{3.32c}$$

Here ∇^s_x is the symmetric part of the gradient operator and $\boldsymbol{\sigma} = -p\,\mathbf{I}$. Piece-wise linear continuous approximation of both kinematic, **u**, and thermodynamic, p, ρ and ϵ, variables are considered. We consider the same decomposition as is performed for the velocity and pressure in section 3.2.3, but this time the decomposition of the ϵ is also added. This gives,

$$\mathbf{u} = \mathbf{u}^h + \mathbf{u}'$$
$$p = p^h + p' \tag{3.33}$$
$$\epsilon = \epsilon^h + \epsilon'.$$

Scovazzi [109] consider also the decomposition of ρ to develop the multiscale method. However, as it has no apparent contribution to the final stabilized form, the density decomposition is omitted here. Furthermore, due to the intrinsic ability of the Lagrangian description to exactly track contact discontinuities without adding numerical dissipation, and as the mass conservation is associated with one of these discontinuities in the form of standing entropy wave, we only focus on the momentum and energy equations to construct the stabilized form.

Inserting the decomposition (3.33) into the variational form (3.32b)-(3.32c), the *coarse scale* equations are formulated as,

$$\int_\Omega \mathbf{v}^h \cdot \rho \, (\dot{\mathbf{u}}^h + \dot{\mathbf{u}}') \, d\Omega - \int_\Omega (p^h + p') \, (\nabla_x \cdot \mathbf{v}^h) \, d\Omega = 0 \tag{3.34}$$

$$\int_\Omega q^h \rho \, (\dot{\epsilon}^h + \dot{\epsilon}') \, d\Omega$$
$$+ \int_\Omega q^h \, (p^h + p') \, \nabla_x \cdot (\mathbf{u}^h + \mathbf{u}') \, d\Omega = 0. \tag{3.35}$$

Using integration by parts, the energy equation (3.35) can be reformulated as,

$$\int_\Omega q^h \rho \, (\dot{\epsilon}^h + \dot{\epsilon}') \, d\Omega + \int_\Omega q^h \, (p^h + p') \, \nabla_x \cdot \mathbf{u}^h \, d\Omega -$$
$$\int_\Omega \nabla_x q^h \cdot ((p^h + p') \, \mathbf{u}') \, d\Omega - \int_\Omega q^h \, (\nabla (p^h + p')) \cdot \mathbf{u}' \, d\Omega$$
$$+ \sum_{e=1}^{n_{el}} \int_{\partial\Omega_e} q^h \, (p^h + p') \, \mathbf{u}' \cdot \mathbf{n}_e \, d(\partial\Omega_e) = 0. \tag{3.36}$$

The last term in (3.36), which is a boundary integral, has two terms; one inter-element boundary term and one domain boundary term.

Similar to the *linearized* case, some simplifications are considered.

1. The fine scale solution, $\mathbf{u}'$, is considered to be zero on the domain boundary.

2. Assuming a continuous solution for $p, \mathbf{u}$ and a continuous approximation for $\mathbf{u}^h$, the fine scale solution turns out to be continuous in the inter-element boundary too i.e. $\mathbf{u}' = \mathbf{u} - \mathbf{u}^h$. As the result, the last term in (3.36) is zero.

3. To preserve the global conservation [109], the internal work done by the fine-scale velocity, $\mathbf{u}'$, is assumed to be zero in a weak sense:

$$\int_\Omega q^h \left(\nabla(p^h + p')\right) \cdot \mathbf{u}' \, d\Omega = 0.$$

4. The *quasi-static* tracking of the subscales is considered.

5. The product of the fine-scale terms is neglected.

The simplified form of the *exact* coarse scale equations (3.34) and (3.35) can be written now as,

$$\int_\Omega \mathbf{v}^h \cdot \rho\left(\dot{\mathbf{u}}^h\right) d\Omega - \int_\Omega (p^h + p')\left(\nabla_x \cdot \mathbf{v}^h\right) d\Omega = 0$$

$$\int_\Omega q^h \left(\rho \dot{\epsilon}^h + p^h \nabla_x \cdot \mathbf{u}^h\right) d\Omega + \int_\Omega q^h p' \nabla_x \cdot \mathbf{u}^h \, d\Omega$$

$$- \int_\Omega \nabla_x q^h \cdot \left(p^h \mathbf{u}'\right) d\Omega = 0. \tag{3.37}$$

Certain similarities are observed comparing the nonlinear coarse-scale equations (3.37) and their linear counterpart (3.27). In particular the momentum equations are practically the same and also recalling (3.19),

$$\rho^h \dot{\epsilon}^h + p^h \nabla_x \cdot \mathbf{u}^h = \rho \frac{\partial \epsilon}{\partial p}\bigg|_\rho (\dot{p} + \rho c_s^2 \nabla_x \cdot \mathbf{u}), \tag{3.38}$$

we observe similarities in the linear and nonlinear energy equations. These similarities give clue to design approximation for the subscales $\mathbf{u}'$ and p'. Note that in comparison to the linearized case (3.27) a new stabilization term of the form,

$$\int_\Omega q^h p' \nabla_x \cdot \mathbf{u}^h \, d\Omega$$

appears. This term has a fundamental role in the global conservation of total energy [109].

We complete our multiscale stabilization by writing the counterpart of equations (3.34) and (3.35), this time tested by the fine scales and rearranged as,

$$\int_\Omega \mathbf{v}' \cdot \rho \dot{\mathbf{u}}' d\Omega - \int_\Omega p'(\nabla_x \cdot \mathbf{v}') d\Omega = - < \mathcal{R}_{\mathbf{u}}^h, \mathbf{v}' > \tag{3.39}$$

$$\int_\Omega q' \rho \dot{\epsilon}' d\Omega + \int_\Omega q' p' \nabla_x \cdot (\mathbf{u}^h + \mathbf{u}') d\Omega = - < \mathcal{R}_\epsilon^h, q' >$$

where $< \mathcal{R}_{\mathbf{u}}^h, . >$ and $< \mathcal{R}_e^h, . >$ belong to the dual space of $\mathbf{v}'$ and q' respectively. They are calculated by doing integration by parts and neglecting the boundary terms, i.e.

$$< \mathcal{R}_{\mathbf{u}}^h, \mathbf{v}' > := \int_\Omega \mathbf{v}' \cdot (\rho^h \dot{\mathbf{u}}^h + \nabla_x p^h) \, d\Omega$$

$$< \mathcal{R}_e^h, q' > := \int_\Omega q' (\rho^h \dot{e}^h + p^h \nabla_x \cdot \mathbf{u}^h) \, d\Omega.$$

Similar to the linearized case and by means of the Riesz representation theorem, the coarse scale residuals, $\rho^h \dot{\mathbf{u}}^h + \nabla_x p^h$ and $\rho^h \dot{e}^h + p^h \nabla_x \cdot \mathbf{u}^h$, can be identified as the members of $(L^2(\Omega))^{n_d}$ and $L^2(\Omega)$ respectively.

We need to approximate subscales from the fine scale equations (3.39) and plug them into the coarse scale equations (3.37). Note that the only fine scales that appear in (3.37) are $\mathbf{u}'$ and p'. Recalling equation (3.38), there is a one by one relationship between $\mathcal{R}_e^h$ and $\mathcal{R}_p^h$, defined in (3.29), so we come out with the same expression as the linear case to approximate p', i.e.

$$p' = -\tau \mathcal{R}_p^h. \tag{3.40}$$

Although $\mathbf{u}'$ can be approximated invoking the same rationalism applied in the linearized case, i.e. $\mathbf{u}' = -\tau \frac{1}{\rho} \mathcal{R}_{\mathbf{u}}^h$, and it is still dimensionally consistent, a more delicate structure could be obtained considering the construction of the term $\int_\Omega \nabla_x q^h \cdot (p^h \mathbf{u}')$ that appears in the coarse scale equations (3.37). The alternative form we propose for the velocity subscales to be substituted into the coarse scale equations (3.37) is,

$$p^h \mathbf{u}' = -\tau(c_s^2) \mathcal{R}_{\mathbf{u}}^h \tag{3.41}$$

where τ has the dimension of time[53, 71, 126, 127, 122, 109, 68, 18] and is taken as Δt, which was one of the options used in,[53, 71] and was the transient limit of the definitions given in[126, 127, 122]. An intuitive interpretation of this choice is to note that $\mathbf{u}' \propto \frac{\Delta t}{\rho} \mathcal{R}_{\mathbf{u}}^h$ and $p \propto \rho c_s^2$.

Introducing the fine scales approximation (3.40) and (3.41) into (3.37), the stabilized variational form of the *nonlinear* hydrodynamic equations is summarized as,

$$\int_\Omega \mathbf{v}^h \cdot \rho (\dot{\mathbf{u}}^h) \, d\Omega - \int_\Omega (\nabla_x \cdot \mathbf{v}^h) p^h \, d\Omega$$

$$+ \int_\Omega \nabla_x \cdot \mathbf{v}^h \, \tau (\dot{p} + \rho c_s^2 \nabla_x \cdot \mathbf{u}) \, d\Omega = 0 \tag{3.42}$$

$$\int_\Omega q^h (\rho \dot{e}^h + p^h \nabla_x \cdot \mathbf{u}^h) \, d\Omega$$

$$+ \int_\Omega \tau(c_s^2) \nabla_x q^h \cdot (\rho \dot{\mathbf{u}}^h + \nabla_x p^h) \, d\Omega \tag{3.43}$$

$$- \int_\Omega q^h \nabla_x \cdot \mathbf{u}^h \, \tau (\dot{p} + \rho c_s^2 \nabla_x \cdot \mathbf{u}) \, d\Omega = 0$$

Note that the first integral in energy equation (5.8) can be replaced by means of equation (3.38) to get a $\mathbf{u}, p$ form similar to the linearized case (3.31). Also by means of (3.41), all stabilization terms are scaled by the acoustic type kinematic viscosity $\tau(c_s^2)$

as mentioned in [109]. Finally the presence of a full residual provides a variationally consistent stabilization that does not reduce the order of accuracy.

The formulation presented above does not apply to the regions where strong discontinuities or shocks appear. In this case a discontinuity capturing operator in the form of artificial viscosities is introduced.

3.2.5 *Discontinuity-Capturing (DC) operator*

In practice we compute an artificial symmetric stress tensor, $\nu_{art;\mathbf{u}} \nabla_x^s \mathbf{u}$, and an artificial flux vector, $\nu_{art;p} \nabla_x p$, that will be activated in the compression zones. The discontinuity capturing operator is then given by,

$$
\boldsymbol{\sigma}_a =
\begin{cases}
\rho\, \nu_{art;\mathbf{u}} \nabla_x^s \mathbf{u} & \nabla_x \cdot \mathbf{u} < 0 \\
\mathbf{0} & \text{else}
\end{cases}
$$

$$
\boldsymbol{\lambda}_a =
\begin{cases}
\nu_{art;p} \nabla_x p & \nabla_x \cdot \mathbf{u} < 0 \\
\mathbf{0} & \text{else}
\end{cases}
\tag{3.44}
$$

where $\boldsymbol{\sigma}_a$ is similar to the quadratic viscosity of von Neumann-Richtmyer [131] type and $\boldsymbol{\lambda}_a$ provides stabilization on the pressure in the energy equation.

One would be tempted to think about $\boldsymbol{\lambda}_a$ as an artificial heat flux, but this interpretation would be incorrect. In fact, the term $\boldsymbol{\lambda}_a$ involves only pressure gradients, and not temperature (i.e., internal energy) gradients. Most importantly, the term $\boldsymbol{\lambda}_a$ is not active at contact discontinuities, where the pressure is continuous and typically constant. $\boldsymbol{\lambda}_a$ is only active where shocks are present, and because the corresponding artificial viscosity does not scale with the speed of sound, this term is expected to be negligible also in compression regions characterized by small pressure gradients.

The artificial viscosities are,

$$
\nu_{art;\mathbf{u}} = c_1 |\nabla_x \cdot \mathbf{u}|\, h_a^2
\qquad\qquad
\nu_{art;p} = c_2 \sqrt{\frac{|\nabla_x p|}{\rho}}\, h_a^{3/2}
\tag{3.45}
$$

$\nu_{art;p}$ is zero when the pressure is constant and so it does not affect the solution at the contact discontinuities and h_a is a measure of the element length along the normal to the shock front. The same definition as [109] is chosen here to define the normal direction, that is a weighted average of the direction of the acceleration vector and the density gradient, as follows,

$$
\mathbf{n} = \frac{0.75\dfrac{\dot{\mathbf{u}}}{\|\dot{\mathbf{u}}\|} + 0.25\dfrac{\nabla_x \rho}{\|\nabla_x \rho\|}}{\left\|0.75\dfrac{\dot{\mathbf{u}}}{\|\dot{\mathbf{u}}\|} + 0.25\dfrac{\nabla_x \rho}{\|\nabla_x \rho\|}\right\|}
\tag{3.46}
$$

and subsequently h_a is defined as,

$$
h_a = \frac{2}{\sqrt{\mathbf{n}^\mathsf{T}(\mathbf{F}\mathbf{F}^\mathsf{T})\mathbf{n}}}
\qquad\qquad
\mathbf{F} = \frac{\partial \mathbf{x}}{\partial \xi}
\tag{3.47}
$$

where $\mathbf{F}$ is the Jacobian of the gradient deformation from the parent domain of the element to the current one and the denominator in (3.47) is a measure of the stretch along the direction of the normal $\mathbf{n}$.

In the next section we present an explicit iterative time integrator for the stabilized nonlinear hydrodynamics equations (5.7)-(5.8). A study of the conservation properties of this scheme can be found in [109].

3.2.6 *Explicit predictor-multi corrector time scheme*

Considering the stabilized form (5.7)-(5.8), the subscales equations (3.40)-(3.41) and the DC operator (3.44), the final form of the hydrodynamic equations (3.32) can be written as,

$$\int_{\Omega_0} q\,(\rho_0 - \rho J)\,d\Omega_0 = 0 \tag{3.48a}$$

$$\int_{\Omega} \mathbf{v}^h \cdot \rho\,(\dot{\mathbf{u}}^h)\,d\Omega + \int_{\Omega} (\boldsymbol{\sigma} + \boldsymbol{\sigma}_a) : \nabla^s_x \mathbf{v}^h\,d\Omega = 0 \tag{3.48b}$$

$$\int_{\Omega} q^h\,(\rho \dot{e}^h)\,d\Omega - \int_{\Omega} q^h\,(\boldsymbol{\sigma} : \nabla^s_x \mathbf{u}^h)\,d\Omega$$
$$- \int_{\Omega} \nabla_x q^h \cdot (\boldsymbol{\lambda} + \boldsymbol{\lambda}_a)\,d\Omega = 0 \tag{3.48c}$$

Where $\boldsymbol{\sigma} = (p^h + p')\,\mathbf{I}$, $\boldsymbol{\lambda} = p^h\,\mathbf{u}'$ and $\boldsymbol{\lambda}_a$ is the artificial, shock-capturing vector flux introduced in (3.44).

The system of equations (3.48) is now discretized in time. An explicit predictor/multi-corrector strategy applied to the mid-point scheme is used. In this way the conservation of mass, momentum and energy are enforced not only at the end of step but also at each nonlinear iteration [109]. Let us introduce the following notation for the mid-point value of a quantity f,

$$f_{n+1/2} = \frac{f_n + f_{n+1}}{2},$$

where $f_n = f(t_n)$. The discretized equivalence of the mass conservation equation is,

$$\int_{\Omega_0} q^h \rho_0\,d\Omega_0 = \int_{\Omega_0} q^h \rho J\,d\Omega_0 = \int_{\Omega} q^h \rho\,d\Omega,$$

and therefore the nodal densities at time step $n+1$, $\boldsymbol{\rho}_{n+1}$, are computed as

$$\mathbf{V}_{n+1}\boldsymbol{\rho}_{n+1} = \mathbf{M}_0$$

$\mathbf{M}_0$ is the vector of nodal mass and its i_{th} component, m_i, is defined as

$$m_i = \int_{\Omega_0} N_i \rho_0\,d\Omega_0. \tag{3.49}$$

Here N_i is the global shape function related to node i. In the same way the lumped nodal volume matrix, $\mathbf{V}_{n+1} = diag(\mathbf{V}_{n+1})$, is defined as

$$\mathbf{V}_{n+1} = \{V_{n+1;i}\} \qquad V_{n+1;i} = \int_{\Omega_{n+1}} N_i \, d\Omega_{n+1}$$

Applying the mid-point rule to the momentum balance in (3.48) we have,

$$\int_{\Omega} \mathbf{v}^h \cdot \rho \, (\mathbf{u}^h_{n+1} - \mathbf{u}^h_n) \, d\Omega$$
$$+ \Delta t \int_{\Omega_{n+1/2}} (\bar{\boldsymbol{\sigma}} : \nabla^s_x \mathbf{v}^h)_{n+1/2} \, d\Omega = 0 \qquad (3.50)$$

where $\bar{\boldsymbol{\sigma}} = \boldsymbol{\sigma} + \boldsymbol{\sigma}_a = (p^h + p') \mathbf{I} + \boldsymbol{\sigma}_a$ and for a quantity $\mathbf{g_t}$ we define,

$$\int_{\Omega_{n+1/2}} \mathbf{g_{n+1/2}} \, d\Omega_{n+1/2}$$
$$= \frac{1}{2} \left(\int_{\Omega_n} \mathbf{g_n} \, d\Omega_n + \int_{\Omega_{n+1}} \mathbf{g_{n+1}} \, d\Omega_{n+1} \right). \qquad (3.51)$$

The matrix form of the momentum equation (3.50) is then written as,

$$\mathbf{M_u} \, (\mathbf{u}_{n+1} - \mathbf{u}_n) + \Delta t \, \mathbf{F}_{n+1/2} = \mathbf{0}. \qquad (3.52)$$

Here $\mathbf{u}$ is the nodal vector of velocity and recalling definition (3.49), the lumped matrix $\mathbf{M_u}$ is,

$$[\mathbf{M_u}] = [diag(\mathbf{M_0}, \mathbf{M_0}, \mathbf{M_0})]. \qquad (3.53)$$

The definition of $\mathbf{F}_{n+1/2}$ is clear from (3.51) and (3.50) and has the following form for node i,

$$\mathbf{F}_{n+1/2} = \{F_{n+1/2;i}\},$$
$$F_{n+1/2;i} = \int_{\Omega_{n+1/2}} (\bar{\boldsymbol{\sigma}} : \nabla^s_x N_i)_{n+1/2} \, d\Omega \qquad (3.54)$$

The discretization of the energy equation (3.48) is done in a similar way. We have,

$$0 = \int_{\Omega} q^h \rho \, (\epsilon^h_{n+1} - \epsilon^h_n) \, d\Omega$$
$$- \Delta t \left(\int_{\Omega_{n+1/2}} q^h \, (\boldsymbol{\sigma} : \nabla^s_x \mathbf{u}^h)_{n+1/2} \, d\Omega \right.$$
$$\left. + \int_{\Omega_{n+1/2}} (\nabla_x q^h \cdot \bar{\boldsymbol{\lambda}})_{n+1/2} \, d\Omega \right) \qquad (3.55)$$

where $\bar{\boldsymbol{\lambda}} = \boldsymbol{\lambda} + \boldsymbol{\lambda}_a$ and therefore the following mid-point discretized form is used to update the nodal internal energy vector $\boldsymbol{\epsilon}$,

$$\mathbf{M}_\epsilon \, (\boldsymbol{\epsilon}_{n+1} - \boldsymbol{\epsilon}_n) + \Delta t \, \mathbf{W}_{n+1/2} = \mathbf{0} \qquad (3.56)$$

$\mathbf{M}_\epsilon$ is an $n_p \times n_p$-dimensional lumped mass matrix, n_p is the total number of nodes, and has the form: $\mathbf{M}_\epsilon = \text{diag}(\mathbf{M}_0)$. The n_p-dimensional vector $\mathbf{W}_{n+1/2}$ is,

$$\mathbf{W}_{n+1/2} = \{W_{n+1/2;i}\}$$

$$\{W_{n+1/2;i}\} = -\int_{\Omega_{n+1/2}} N_i \, (\boldsymbol{\sigma} : \nabla_x^s \mathbf{u}^h)_{n+1/2} \, d\Omega$$

$$- \int_{\Omega_{n+1/2}} (\nabla_x N_i \cdot \bar{\boldsymbol{\lambda}})_{n+1/2} \, d\Omega \tag{3.57}$$

Note that all integrals calculated in the domain $\Omega_{n+1/2}$, in equations (3.57) and (3.54), are understood in the sense of equation (3.51).

Table 3.1: Mid-point explicit predictor/multi-corrector algorithm

Initialize all variables with initial conditions
Calculate $\mathbf{M}_0$, $\mathbf{M}_u$ and $\mathbf{M}_\epsilon$
For $n = 0, ..., n_{steps}$ *(Begin time step loop)*
  Calculate Δt by CFL condition
  Predict: $\mathbf{Y}_{n+1}^0 = \mathbf{Y}_n$
    For $i = 1, ..., i_{max}$*(Begin multi-corrector loop)*
    Assemble: $\mathbf{F}_{n+1/2}^i$
    Velocity update : $\mathbf{u}_{n+1}^i = \mathbf{u}_n - \Delta t \, [\mathbf{M}_u]^{-1} \, \mathbf{F}_{n+1/2}^i$
    Position update : $\mathbf{X}_{n+1}^i = \mathbf{X}_n + \Delta t \, \mathbf{u}_{n+1/2}^i$
    Volume update : $\mathbf{V}_{n+1}^i = \mathbf{V}(\mathbf{X}_{n+1}^i)$
    Density update : $\boldsymbol{\rho}_{n+1}^i = [\mathbf{V}_{n+1}^i]^{-1} \, \mathbf{M}_0$
    Assemble: $\mathbf{W}_{n+1/2}^i$
    Energy update: $\boldsymbol{\epsilon}_{n+1} = \boldsymbol{\epsilon}_n - \Delta t \, [\mathbf{M}_\epsilon]^{-1} \, \mathbf{W}_{n+1/2}^i$
    Pressure update: $\mathbf{P}_{n+1}^i = \hat{p}(\boldsymbol{\rho}_{n+1}^i, \boldsymbol{\epsilon}_{n+1}^i)$
    End *(multi-corrector loop)*
  Update data base: $\mathbf{Y}_{n+1} = \mathbf{Y}_{n+1}^{i_{max}}$
End *(Time step loop)*

As any Lagrangian formulation the position of the nodes need to be updated. This can be done integrating in time the set of equations for nodal displacement to get,

$$\mathbf{X}_{n+1} = \mathbf{X}_n + \Delta t \, \mathbf{u}_{n+1/2} \tag{3.58}$$

where $\mathbf{X}_{n+1}$ is the vector of nodal positions at t_{n+1}.

Once the updated value for $\boldsymbol{\epsilon}_{n+1}$ and $\boldsymbol{\rho}_{n+1}$ has been obtained the nodal pressures are updated by means of the EOS at each nodes,

$$p_{n+1} = \hat{p}(\rho_{n+1}, \epsilon_{n+1}) \tag{3.59}$$

and a piece-wise continuous pressure field is constructed by updated nodal values.

The update of velocity and internal energy from (3.52) and (3.56) needs the knowledge of step $n + 1$. A fully explicit predictor/multi-corrector strategy is adopted to avoid the inverse of systems and also to best handle the nonlinearities in the calculation of the force and work terms.

Table 4.1 shows the predictor/multi-corrector algorithm. In this table $\mathbf{Y}_t$:

$$\mathbf{Y}_t = \left[\boldsymbol{\rho}_t^{\mathsf{T}}, \mathbf{u}_t^{\mathsf{T}}, \boldsymbol{\epsilon}_t^{\mathsf{T}}, \mathbf{P}_t^{\mathsf{T}}, \mathbf{X}_t^{\mathsf{T}} \right]^{\mathsf{T}}$$

is the state of the system at time t where $\mathbf{P}$ is the vector of nodal pressures.

The mid-point values at each iteration are calculated form the previous step and the current iteration data.

The subscales are included in $\mathbf{F}_{n+1/2}^i$ and $\mathbf{W}_{n+1/2}^i$. As the residuals are evaluated at the mid-points, the residual-based definition of the subscales implies that the subscales are also calculated at the mid time intervals. Therefore, by recalling the hypothesis of *quasi-static* subscales, we consider that they are constant during a time interval.

Recalling (3.40) and (3.41) we have

$$p'_{n+1/2;i} = -\tau \left(\mathcal{R}_p^h \right)_{n+1/2}^i$$
$$(p^h \mathbf{u}')_{n+1/2;i} = -\tau \left(c_s^2 \mathcal{R}_{\mathbf{u}}^h \right)_{n+1/2}^i$$

where residuals are defined as,

$$\left(\mathcal{R}_p^h \right)_{n+1/2}^i = \frac{p_{n+1}^{h;i} - p_n^h}{\Delta t} + \left(\rho c_s^2 \nabla_x \cdot \mathbf{u} \right)_{n+1/2}^{h;i}$$
$$\left(\mathcal{R}_{\mathbf{u}}^h \right)_{n+1/2}^i = \rho_{n+1/2}^i \frac{\mathbf{u}_{n+1}^{h;i} - \mathbf{u}_n^h}{\Delta t} + \left(\nabla_x p \right)_{n+1/2}^{h;i}$$

Considering that the subscales are constant during each time interval the force term related to the subscales in (3.54) is calculated as,

$$\int_{\Omega_{n+1/2}} (p'_{n+1/2;i} \nabla_x \cdot \mathbf{u})_{n+1/2} \, d\Omega$$
$$= \frac{1}{2} \left(\int_{\Omega_{n+1}} p'_{n+1/2;i} (\nabla_x \cdot \mathbf{u})_{n+1} \, d\Omega \right.$$
$$+ \left. \int_{\Omega_n} p'_{n+1/2;i} (\nabla_x \cdot \mathbf{u})_n \, d\Omega \right)$$

The fine scale work term in (3.57) is calculated in a similar way by assuming that the subscales are constant in the time interval.

The Lagrangian description of the motion, considered in this work, implies movement of the particles with their convective velocities that may cause large deformations of the finite element mesh. In the next section we extend and improve an interface detecting technique, that was originally proposed for incompressible multiflows [57, 56], to the air-water compressible system. In essence, pressure and density are duplicated at the interface and the interface shape is conserved at each generation of the mesh.
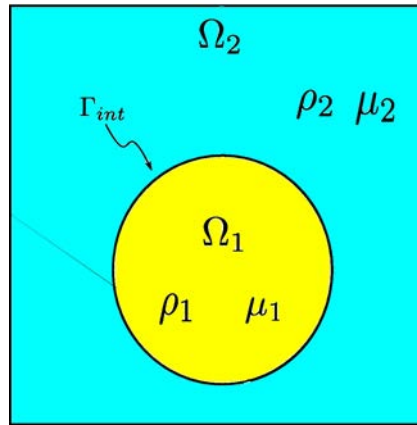
Figure 3.3: A schematic view of a two-fluid system with different material properties and the internal interface.

3.3 TWO-PHASE TREATMENT

Although the robustness of a moving Lagrangian frame for the solution of hydrodynamic equations in the presence of different shock fronts have been tested by many authors [109, 27, 12], the extensions of this frame to multi-phase flow have been restricted due to the presence of the material interface and its possible distortion. In the context of incompressible flow, multi-fluid systems with large density jumps and interface distortion have been successfully resolved via the PFEM [59, 92, 57, 56].

3.3.1 *Nodally matched interface*

The ability of PFEM to accurately simulate large deformations in laminar flows of Newtonian viscous multi-fluids is shown in detail in the work of by Mier-Torrecilla et al [25].

Their answer to the crucial question of multi-fluid flows that simply reduces in *what* is the interface and *how* it is evolved is as follows. Consider the two-fluid immiscible system of Figure 3.3. We know that one of the main features of particle methods is that all the physical properties are attached to the nodes instead of the elements and that the mesh is permanently updated. Hence, it is difficult to keep physical properties at element level. On the other hand, heterogeneous flows can have a jump in the fluid properties of several orders of magnitude and one must decide where does the internal interface between two different fluids occur.

A natural choice is to consider an average of the nodal properties in each element. This means to consider an interface that pass through elements as shown in Figure 3.4a. As one can see in this way a jump in density is not exactly captured (Figure 3.4a). it is shown in [25, 57] that this choice of interface would result in spurious pressure mode at the interface level that will propagate through the solution. In the Eulerian context different remedies are presented to resolve this problem that end up with adding new degrees of freedom along the elemental interface [19, 17].

Another possibility is to impose that the interface between different materials is described by element edges. This will be called *nodally matched interface* (Figure 3.4b). For the nodally matched interface one accept that elements sharing particles with two

(a)

(b)
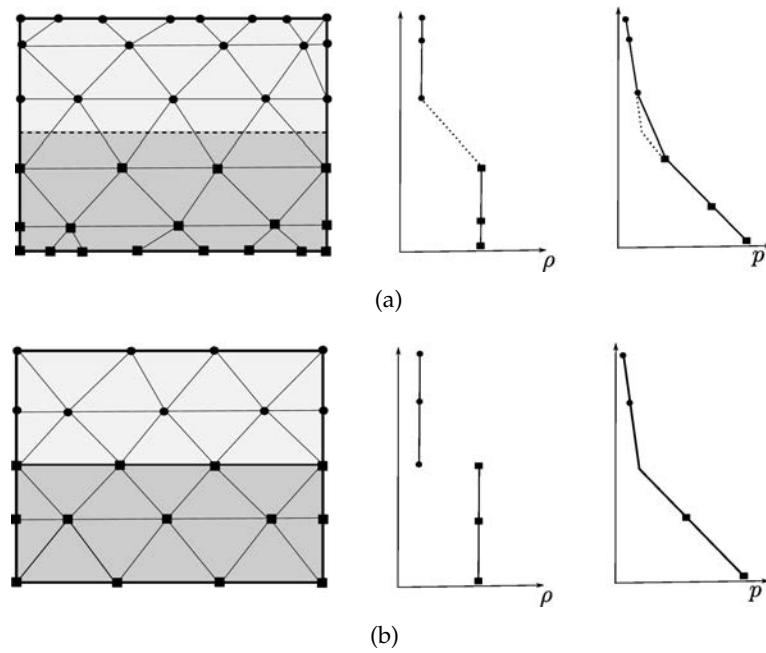
Figure 3.4: Density and pressure representations for the different interface definitions: a) Elemental definition of the interface. , b) Nodally matched interface. Note the exact representation of pressure for the nodally matched interface.

different properties , two densities for example, will have one or the other particular property value i.e. no mean value is used. Furthermore, in the nodal representation the interface is described by mesh nodes and element edges, i.e. a well-defined curve, with the information regarding its location and curvature readily available.

The interface nodes carry the jump of properties (e.g. density, viscosity), maintaining the interface sharp without diffusion along time. Indeed, it is straightforward to impose the boundary conditions on the interface and to treat any number of fluids.

Regarding the two-phase system of Figure 3.5 we choose water as the dominant flag. This implies that those elements that have at least one node as water are *colored* as water elements and only those elements that have all nodes as air are *colored* as air elements. The *nodally perfect matched* interface now appears as the boundary layer that separates air and water elements. As the initial position of the interface is known, the choice of the dominant flag is done in such a way that the resulting nodal interface matches the initial interface at the beginning.

The definition of the interface reviewed above in addition to the intrinsic property of PFEM, that is a moving particle approach, are the main ingredients of the interface treatment by PFEM. Some of the main difficulties in the numerical simulation of multi-fluid flows that this method has successfully overcome are as follows [25]:

1. Appropriate tracking of the interface without introducing excessive numerical smoothing.

2. Modeling large discontinuities across the interface. In fixed mesh methods, the interface is tracked, the elements are cut by the interface position and, therefore, enrichment of pressure, in case of gravity flows, and enrichment of velocity, in case of viscosity dominant flows, is required. However, in the nodally
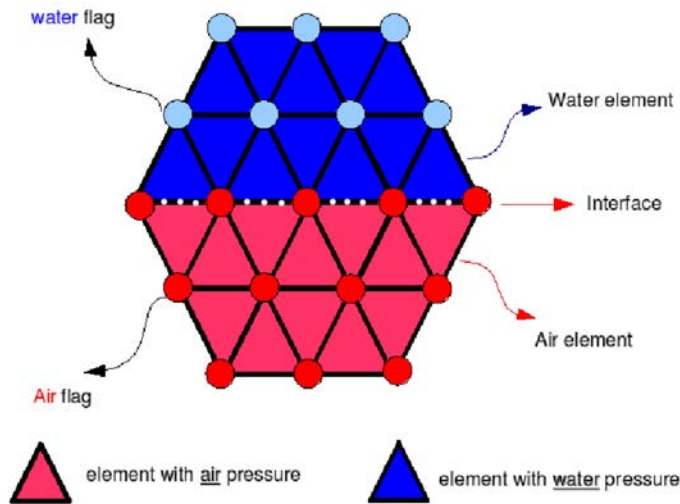
Figure 3.5: Nodally matched interface

matched interface technique, a jump in density does not require any enrichment, although special care has to be taken in stabilization. For viscosity jumps the minimum duplication of degrees of freedom is required.

3. Modeling of the surface tension. Since surface tension plays a very important role in the immiscible interface dynamics, this force needs to be accurately evaluated and incorporated into the model.

One important aspect that is also mentioned in the work of Mier-Torrecilla [25] but it seems that no effective solution is presented to resolve it, is the conservation of the interface during the re-meshing process. The regeneration of the mesh when it becomes too distorted may change the nodes and edges that describe the interface. It is essential to guarantee that the interface is conserved during re-meshing. In the following we explain how this problem may appear in the re-meshing process.

3.3.2   *Mesh construction*

Lagrangian methods are characterized by the fact that the mesh follows the flow motion. After a time, nodes that were initially close together may no longer be close, and some nodes that were initially distant begin to approach each other. The mesh needs to be regenerated when it becomes too distorted due to large deformations.

Given a set of points P in the plane, the Delaunay triangulation constructs a set of triangles whose vertices are the points P such that the circumcircle associated with each triangle contains no other point in P. This is the geometric dual of the Voronoi diagram of P, and each triangle satisfies the empty circumcircle property. The Delaunay triangulation results in a unique mesh for a given set of nodes except in the case when four nodes lie on the same circle (see Figure 3.6).

In the vicinity of the interface, this property can produce considerable change in the position of the interface. Figure 3.7 depicts how mere re-meshing can change the interface position. These connectivity changes may affect the convergence of the numerical algorithm and the mass conservation. A remedy to minimize this effect is
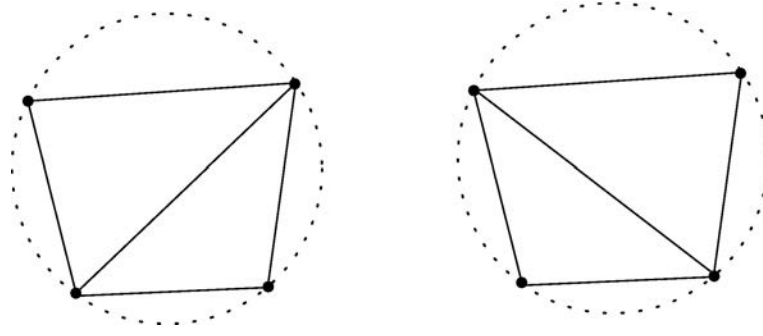
Figure 3.6: Edge swapping occurs when four nodes line on the same circle.
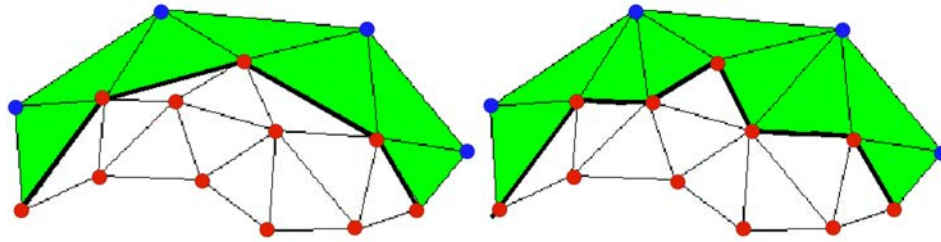
Figure 3.7: Change of connectivities causes change of interface position

to delete those bulk nodes that get too close to the interface, and add nodes on the element edges that are too long. Alternatively, one could use a constrained Delaunay algorithm [112], which allows to fix certain connectivities. Therefore, by constraining the connectivity of the edges that describe the interface to avoid possible swapping, the interface is conserved exactly after re meshing. In the present work we take advantage of both of these remedies. First, nodes that are excessively close to the interface, i.e much less than the element size, are taken out and second, *constrained* re-meshing is done to preserve, as much as possible, the interface connectivities.

Concerning adaptive mesh refinement, a *distance* function that vanishes at the interface is used. Later a *length parameter*, *H*, calibrated by the distance function is assigned to each node of the mesh. The idea is simply to provide a fine mesh near the interface and a coarse one in farther zones. The calibration function, f, can be chosen as a linear function of the distance, d, a step function or simply as any other function that provides the desired refinement at the interface zone,

$$H = f(d).$$

For 2D case problems we choose the Triangle [112] software to build the FE mesh at each step. This mesh generator permits an adaptive constrained Delaunay triangulation of the domain. This is necessary to conserve the connectivities at the interface, as much as possible, and refine the mesh. Interface connectivities are stored in the *segment* list provided by Triangle and then the constrained remeshing is performed as described in [112].

It is necessary to mention that new nodes are added automatically to the interface at the moments of expansions of the interface to maintain the same mesh size at the

interface level. Adaptive refinement is always done by use of a primary mesh. This mesh could be the previous step mesh or one that is created at the beginning of the remeshing phase. To each element of the base mesh an area, A, is assigned. This area would be the maximum area that is expected after the refinement of the element. The *length parameter*, H, that has been already assigned to each node is used to compute the maximum area that is the one of the equilateral triangle with the edge size equal to the mean value, $\bar{H}$, of the nodal length parameters, H, as

$$A = \bar{H}^2 \frac{\sqrt{3}}{4}$$

Similar to the *segment* list, the area map is saved to the *area* list provided by the mesher and the adaptive construction of the mesh is done respecting the area map.

As the refinement is always done around the interface, a derefinement technique is useful when there are large movements of the interface. The distance from the interface is reflected in the length measure that is assigned to each node and, therefore, as a node gains a relative distance from the interface its length measure increases. Considering a circle with the radius equal to the length measure around each node, more neighbors fall in the circle as the length measure increases. This indicator can be used to *mark* neighbor nodes for being deleted from the cloud of nodes and therefore derefine the mesh in the farther zones. Note that the increase of the length measure results in the increase of the minimum area used to refine the mesh and, consequently, no new nodes will be created in the derefined zones.

Table 3.2: Constrained mesh generation process

Remesh:
• Calculate *distance* and assign length parameter, H.
• *Mark* nodes
• Detect interface connectivities (fill *segment* list).
• Delete nodes if assigned by *Mark* node process.
• Generate a constrained triangulation of the domain.
• Assign *area* constraint to each element.
• Generate the final refined mesh respecting.
area and *segment* constraints.
• Interpolate for new added nodes.

Table 3.2 summarizes different steps of the mesh generation process. As we mentioned before, the refinement is done by use of a base mesh that is created in the fifth step. The database for the new nodes that are created during the refinement process are interpolated from the database of the base mesh i.e. each new node falls in one of the elements of the base mesh and therefore its database is filled by a linear interpolation of the databases of the nodes of that element. Having the nodally perfect matched

interface, the material flag of a new node is easily inherited from the material flag of the base element.

3.3.3 *Discontinuous kinetic field*

The preceding definition of the interface has been successfully tested for incompressible heterogeneous flows with large density and viscosity jumps [57, 56]. For incompressible heterogeneous flows a viscosity jump results in a discontinuous pressure across the interface while for compressible multi-flows, contact discontinuous fields usually appear as the initial values. Large jumps of two or three order of magnitudes in pressure fields in simple 1D gas-water tube or in violent collapsing bubble case are quite common. In practice it is desired that each set of elements has its own kinetic field i.e. air-pressure for air elements and water-pressure for water elements. This is faciated by having all kinetic and kinematic variables carried by the particles. The duplication of the kinetic fields, pressure and density, at the interface particles suffices to yield air-field and water-field variables.

This duplication can be also seen as the result of two types of elements, air-element and water-element, being connected together and through the interfacial common nodes. Note that here particles are not being duplicated at the interface but just the kinetic variables are. Hence, comparing to the elemental definition of the interface, a minimum number of degrees of freedom is added to capture the discontinuity.

3.4 NUMERICAL EXAMPLES

In this section we verify the Lagrangian compressible framework proposed in previous sections for a series of benchmark examples and then simulate the underwater implosion of large bubbles, in the order of *cm*. Three-noded linear isotropic triangular elements are used in all examples.

Following 1D hydrodynamics of the bubble that predicts a successive chain of contraction-expansion of the bubble, we choose Noh [81] and Sedov [110] tests to verify our formulation in severe compression and expansion flow regimes.

In the contraction phase, called implosion, converging pressure waves results in a shock created at the center of the bubble. Noh test, designed to study in detail the conversion from kinetic energy into internal energy, is a challenging test for compressible codes and is studied first.

The reaction to the contraction phase is an expansion (explosion) manifested by pressure waves traveling spherically in the domain. Sedov proposed a self-similar solution for the state variables that define the perturbation produced by a detonation at the center of the symmetry. The *standard* [66] version of his test is studied to verify the behavior of the code in diverging wave examples.

Both tests are done in 1D and 2D configurations and with fine and coarse meshes.

A 1D air-water tube test with jumps of several orders of magnitudes in density and pressure examines the robustness of the discontinuous multiphase scheme proposed in Section 3.3.

Finally the underwater implosion of a cm size cylindrical bubble is studied. We observe instabilities at the interface of the bubble in the final stage of the collapse phase that disappear at the beginning of the expansion phase. The bubble finally ruptures
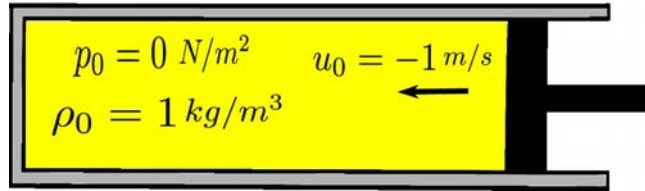
Figure 3.8: 1D Noh test shock tube

at the end of the second expansion-contraction cycle. We verify our simulation by comparing the pressure pulse detected in water for the air bubble implosion with the experiment [129] provided by Turner.

3.4.1 *Noh test*

Noh test [81] models the conversion of kinetic energy to internal energy. The setup of the test (Figure 3.8) consists of a shock tube in which a cold, uniform perfect gas is driven by a piston with constant speed into a rigid wall. It can be easily generalized to 2D and 3D cases if we identify the rigid wall with the axis of a cylinder or the center of a sphere, and the piston with their respective outer walls.

The shock tube has a unit length and the piston moves with the velocity of $u_0 = -1 m/s$ towards the wall. Density is uniform everywhere and is equal to 1, $\rho = 1.0 \, kg/m^3$. The initial pressure and internal energy are zero along the tube.

At the instance the piston is pushed inward, a stagnation shock of infinite strength is created at the origin (rigid wall). Zero pressure in the pre shock zone results in zero sound velocity and therefore the Mach number of the shock is infinity, something that makes this problem challenging to numerical methods.

The gas is ideal with $\gamma = 5/3$ and the analytical solution suggests that the shock will propagate with the velocity equal to $\frac{1}{3}u_0$ ($v_s = (\gamma - 1)u_0/2$). The exact values for pressure and density in the past shock zone are $p = 4^{n_d}/3$ and $\rho = 4^{n_d}$, respectively, where n_d is 1 for the 1D case and 2 for the 2D one.

Considering the shock speed of 1/3, we expect to see the shock wave at the radial position of $0.2 \, m$ from the center of the shock at the time instant $t = 0.6 \, s$. The results for the 1D simulation can be seen in Figure 3.9. The exact values for pressure, density, velocity and internal energy are shown in solid lines. The pressure value for the pre shock zone is $p = 4/3$ and a constant density equal to 4 is expected in this zone. Results for the 50 and 100 element meshes are compared with the exact values [81].

The computational domain for the 2D case is a $[0, 1] \times [0, 1]$ square domain. Two mesh resolutions of 50 and 100 divisions are considered. Initial values for the pressure and density are the same as for the 1D case. All nodes except the one of the center of symmetry have an initial radial velocity toward the center, equal to 1.

Figure 3.10 shows the mesh configuration and the pressure field at instant $t = 0.6s$. The pre shock zone values for the pressure and density are $p = 16/3$ and $\rho = 16$, respectively. Figure 3.11 depicts the exact solutions, solid lines, for various variables of interest compared with the results obtained for the coarse and fine mesh along the radius. Note that the exact pressure distribution, $p = 1 + 0.6/r$, is captured in the pre shock zone.

Figure 3.9: 1D Noh test. Results for 50, "□", and 100, "●", element meshes. Figures *a* to *d* show the exact solution in *solid* line for pressure, density, internal energy and velocity in comparison with the numerical ones. Artificial viscosities are shown in figures *e* and *f*.

Good agreement between the numerical and exact solution is obtained for both position of the shock and the pre and post shock zone values. Note that the shock capturing terms are just activated in some elements along the shock.

The known wall heating phenomenon [104] is also seen here in the excessive values of the internal energy at the center.
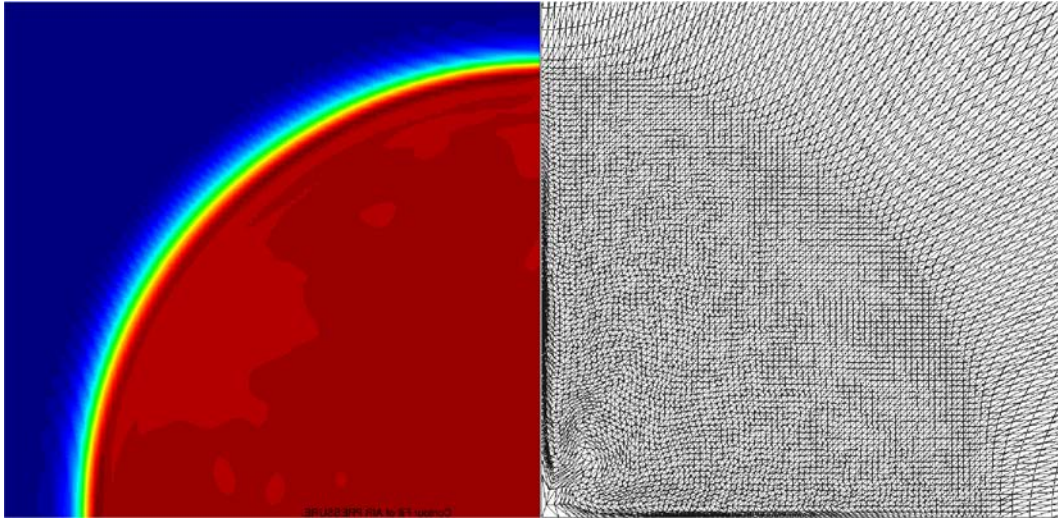
Figure 3.10: 2D Noh test. Mesh configuration and pressure field at time t = 0.6 s.

3.4.2 *Sedov test*

Sedov [110] provided analytical solution for the motion of a gas initially at rest and being disturbed by a detonation at the center of symmetry (Figure 3.12a).

We choose here the *constant* initial density case among the Sedov setting tests for which the initial density, $\rho_0 = 1g/cm^3$, is uniform and constant everywhere, the gas is ideal with $\gamma = 7/5$ and the internal energy, e, is zero everywhere except in a small zone at the center of symmetry.

Planar and cylindrical tests are considered for which $e = 0.0673185$ for the planar case, and $e = 0.311357$ for the cylindrical one, in some elements near the center. These value are chosen in accordance with [66] to be able to reproduce the exact self-similar Sedov solutions.

For the 1D case a 1m long tube as shown in Figure 3.12b is discretized with triangular elements. Two mesh sizes of 0.01 and 0.02 are considered. The left wall has a fixed velocity and the rest of the domain has zero initial velocity. The shock, instantaneously created at the left wall, reaches the middle of the tube at time t = 1.0s. The mesh configuration at this instant is shown in Figure 3.12c.

In Figure 3.13 the self similar exact solutions for the state variables (solid lines) are compared with the numerical ones at t = 1.0s. The extension to the cylindrical case is obtained by considering a square domain of $[0, 1.2] \times [0, 1.2]$. Two Cartesian meshes, with the same element sizes as the 1D case, are considered. The initial internal energy is zero everywhere except at the center of symmetry where an initial value of $e = 0.311357$ is assigned to few elements near the center. Zero velocity is considered everywhere and the initial density is equal to 1. After 1s the circular detonation shock wave reaches to the radial position of 0.75. This pressure wave and the current mesh configuration can be seen in Figure 3.14. No remeshing is applied to the Sedov and Noh tests. Figure 3.15 compares the exact [66] and numerical solutions obtained for the two mesh resolutions.
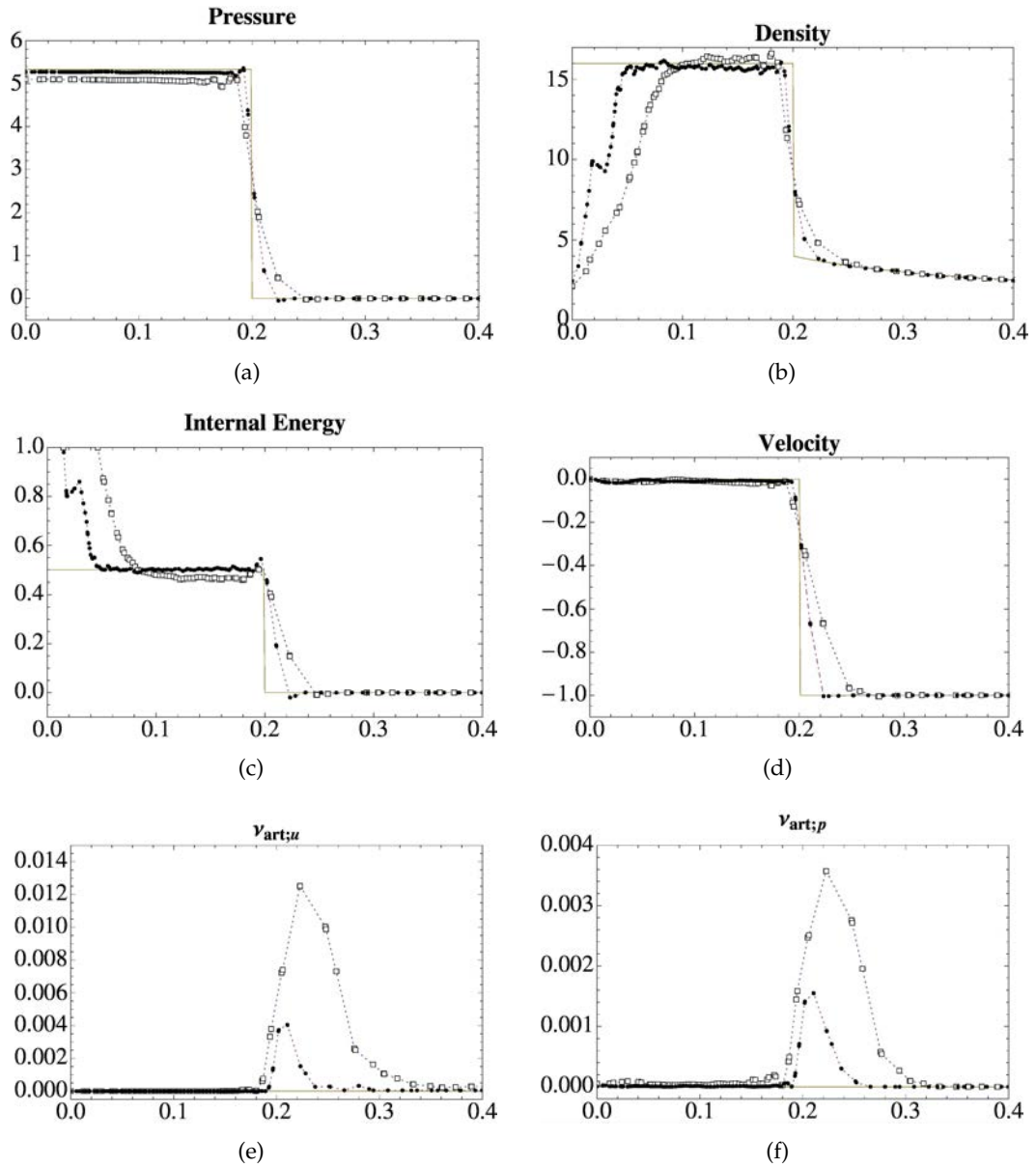
Figure 3.11: 2D Noh test. Results for 50×50,"□", and 100×100, "•", element meshes. Figures *a* to *d* show the exact solution in *solid* line for pressure, density, internal energy and velocity in comparison with the numerical ones. Artificial viscosities are shown in figures *e* and *f*.

3.4.3 *Air-water system with big density jump*

The two-phase flow with large density, pressure jumps and two different EOSs is considered. Air is modeled as a perfect gas with $\gamma = 1.4$ and the high pressure water is modeled by the Tait's EOS with $k_1 = 2.7 \times 10^9, k_2 = 7.15$, as

$$\rho = \rho_0 \left(\frac{p + k_1/k_2}{p_0 + k_1/k_2}\right)^{\frac{1}{k_2}}$$

(a)

(b)

(c)
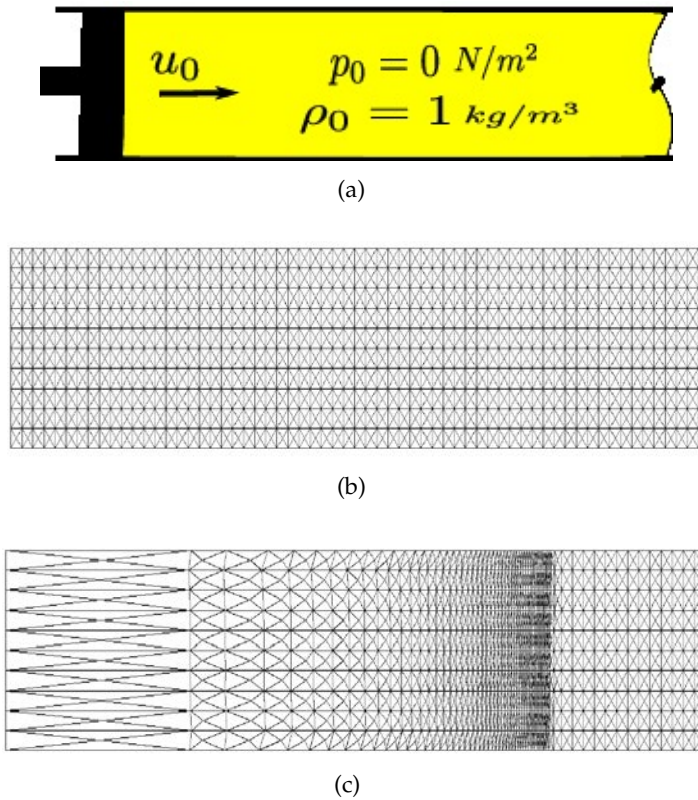
Figure 3.12: 1D Sedov test. a) *constant* initial density, b) initial mesh configuration, c) mesh configuration for t $= 1.0$s

The same setting as the one proposed by Farhat et al [31] is used. A tube is filled with air on the left side, a membrane positioned at $x = 0.3$ and water on the right side (Figure 3.16). Both fluids are initially at rest. A density jump of order 1000 and a pressure jump of order 100 is produced.

The discontinuous pressure scheme explained in Section 3.3 allows us to initialize interface nodes for both the water and air initial pressures.

The computations are done in a 1m long tube discretized by 200 three-noded triangles. Figure 3.17 depicts the results obtained at t $= 4 \times 10^{-4}$s. The structure of the solution consists of a shock wave traveling in the air, a contact discontinuity, manifested in the density graph, and a rarefaction wave propagating in the water.
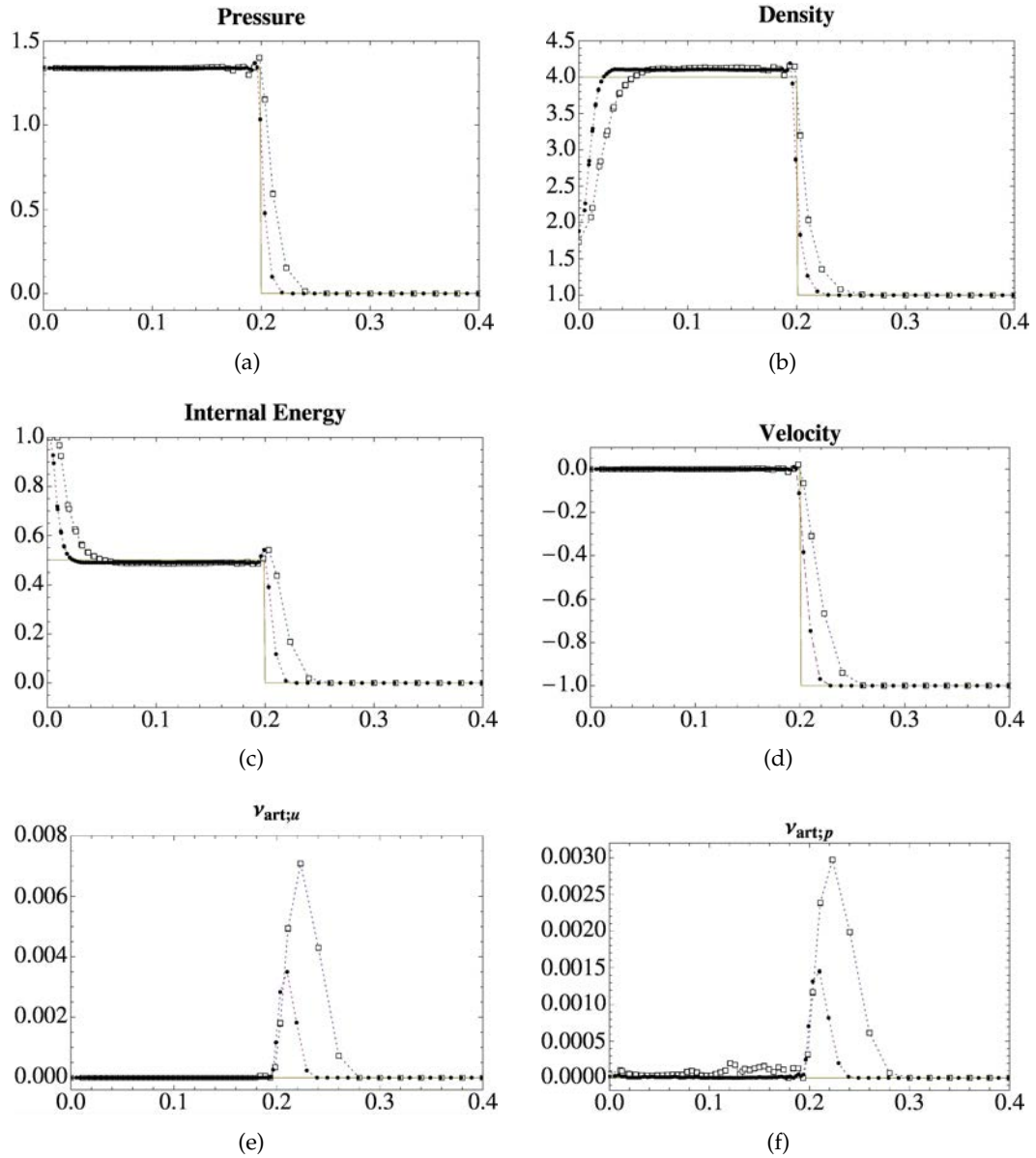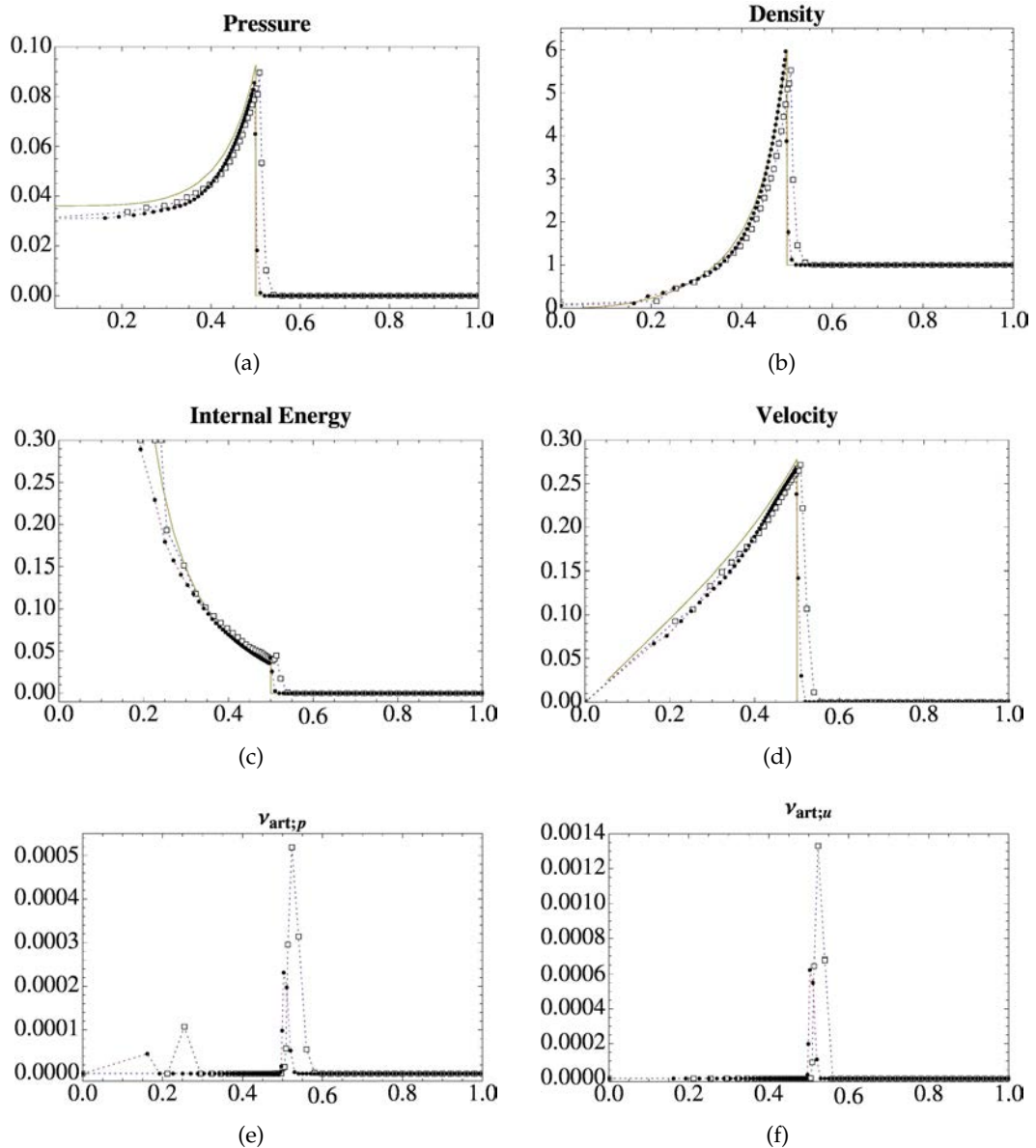
Figure 3.13: 1D Sedov test. Results for 60, "□", and 120, "•", element meshes. Figures *a* to *d* show the exact solution in *solid* line for pressure, density, internal energy and velocity in comparison with the numerical ones. Artificial viscosities are shown in figures *e* and *f*.

3.4.4   *Underwater implosion of cylindrical bubble*

In this section we study the implosion of an infinitely long cm size cylindrical bubble which is initially at atmospheric pressure and is being compressed by the surrounding pressurized water at 70 atmospheres. The initial radius of the bubble is 3.81 cm and the numerical domain is a 1×1m square (Figure 3.18).

As we are interested to study the possible instabilities that may occur during the collapse, a full model is considered. The inside air is modeled as a perfect gas with $\gamma = 1.4$. Water is modeled by Tait's equation of state presented in Section 3.4.3.
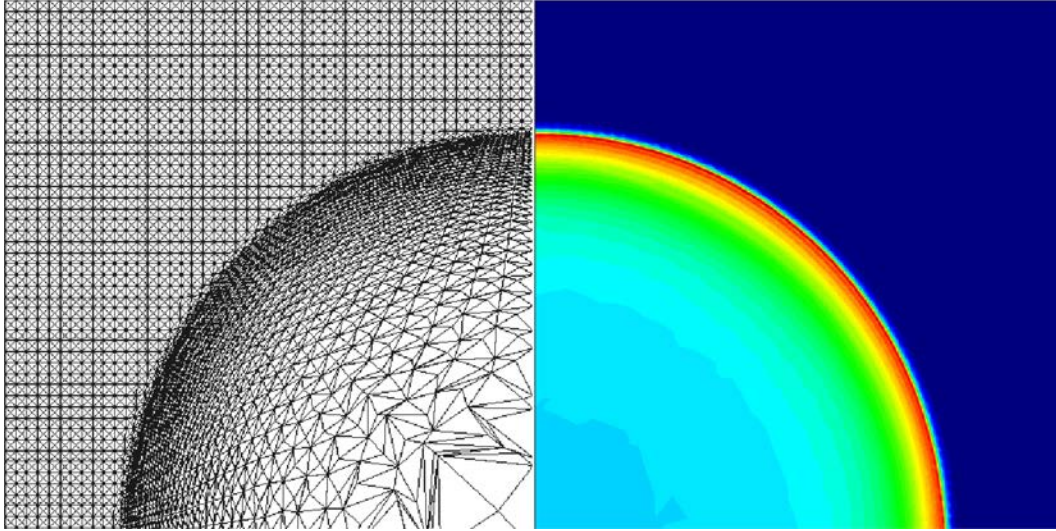
Figure 3.14: 2D Sedov test. Pressure field and mesh configuration at time t = 1.0 s.

Adaptive mesh refinement is considered in three levels and with respect to the distance calculated from the air-water interface. We seek to obtain a constant number of elements at the interface level to cope with the dramatic change of bubble radius, variations up to 90% of the initial diameter, during the collapse and rebound phases. In this way starting from a fine mesh at the beginning of the solution, the quality of the results is guaranteed during the simulation.

Figure 3.19a shows the time histories of the x and y measures of the bubble radius along with the pressure at the center of the bubble. The set up of the test is the same as the underwater implosion at a depth around 700 m and therefore the behavior expected for the bubble is the *violent collapse* that consists of one or two pulses leading to the collapse.

The variation of the *length parameter*, H, of a sample node on the interface in time is shown in Figure 3.19b. This parameter is used to refine the mesh in the vicinity of the interface, as explained on Section 3.3.2.

Interface values of the H have to be a function of the bubble radius to provide enough refinement during the contraction and expansion phases. As the minimum element size is required at the interface level, the minimum *length parameter*, H_{min}, is assigned to the interface nodes. For the rest of the nodes, the distance to the interface is used for choosing H.

Three levels of refinement are considered by using the following piecewise linear function for the variation of H,

$$H(d) = \begin{cases} H_{min} & d < 10\,H_{min} \\[2ex] H_{min} + 0.25\,(d - 10H_{min}) & 10\,H_{min} < d < 50.0\,H_{min} \\[2ex] 10\,H_{min} + (d - 50\,H_{min})\dfrac{H_{max} - 10\,H_{min}}{250} & 50\,H_{min} < d < 300.0\,H_{min} \\[2ex] H_{max} & d > 300.0\,H_{min} \end{cases}$$

(3.60)
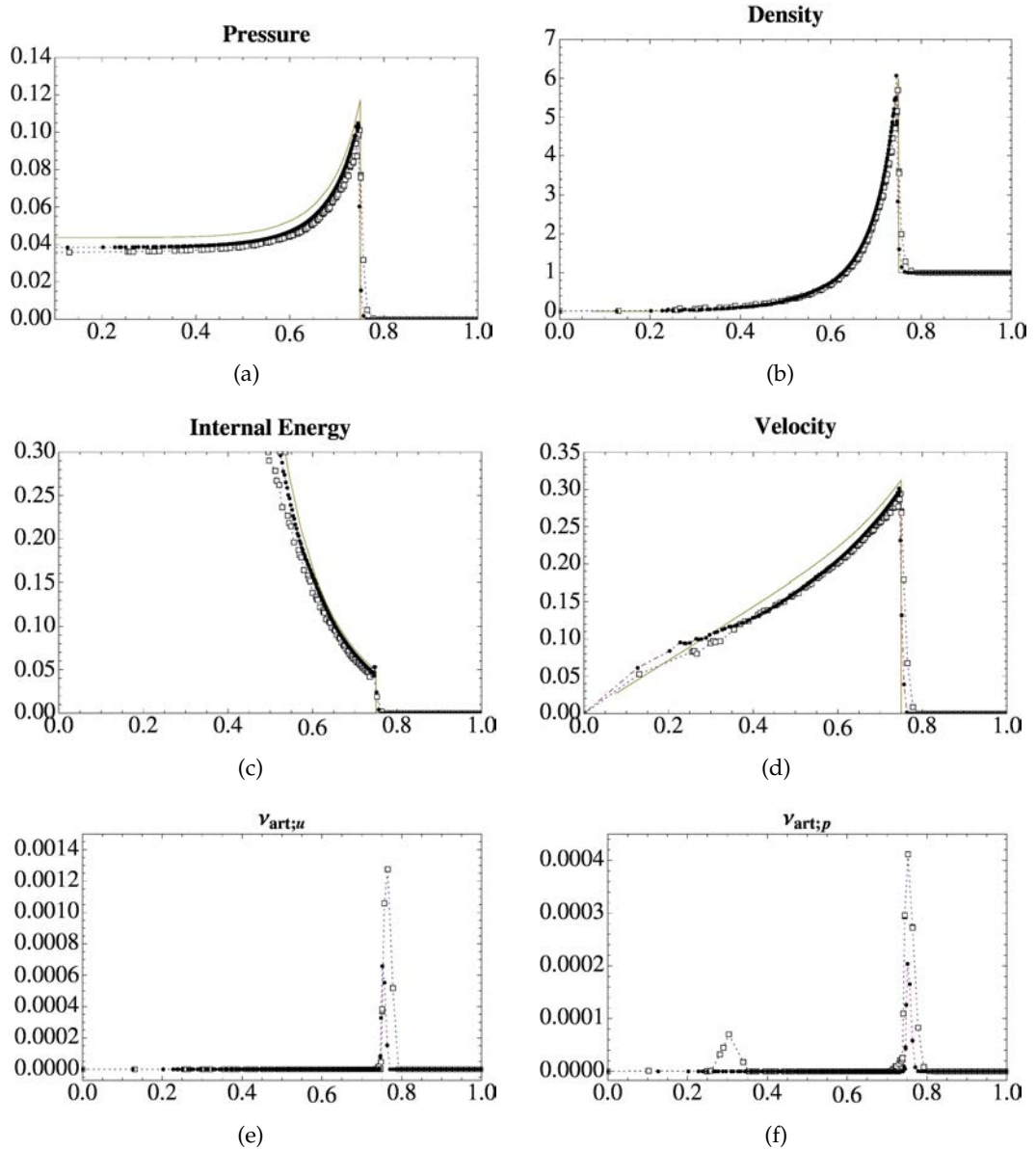
Figure 3.15: 2D Sedov test. Results for 60×60, "$\square$" , and 120×120, "$\bullet$", element meshes. Figures *a* to *d* show the exact solution in *solid* line for pressure, density, internal energy and velocity in comparison with the numerical ones. Artificial viscosities are shown in figures *e* and *f*.

where d is the distance from the interface and H_{max} is the element size far from the interface zone. Here H_{min} is assigned to the first layer near the interface and then two more levels of refinement, base on the distance from the interface, are considered. H_{max} is chosen in a way that the mesh in far distant zones, where no considerable movement occurs, remains unchanged.

Figure 3.20a and 3.20b show the mesh near the interface at the beginning of the simulation and at the moment of maximum contraction. The same level of zoom is chosen for both cases for depicting the variation of the bubble radius during the
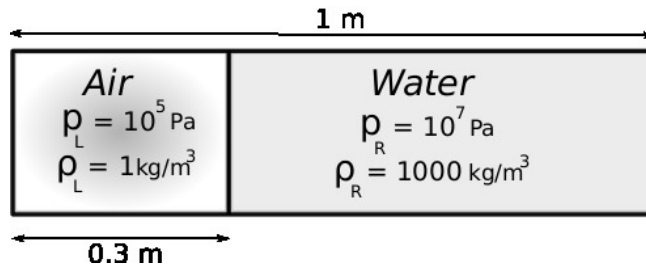
Figure 3.16: Air-Water tube

(a)

(b)

(c)
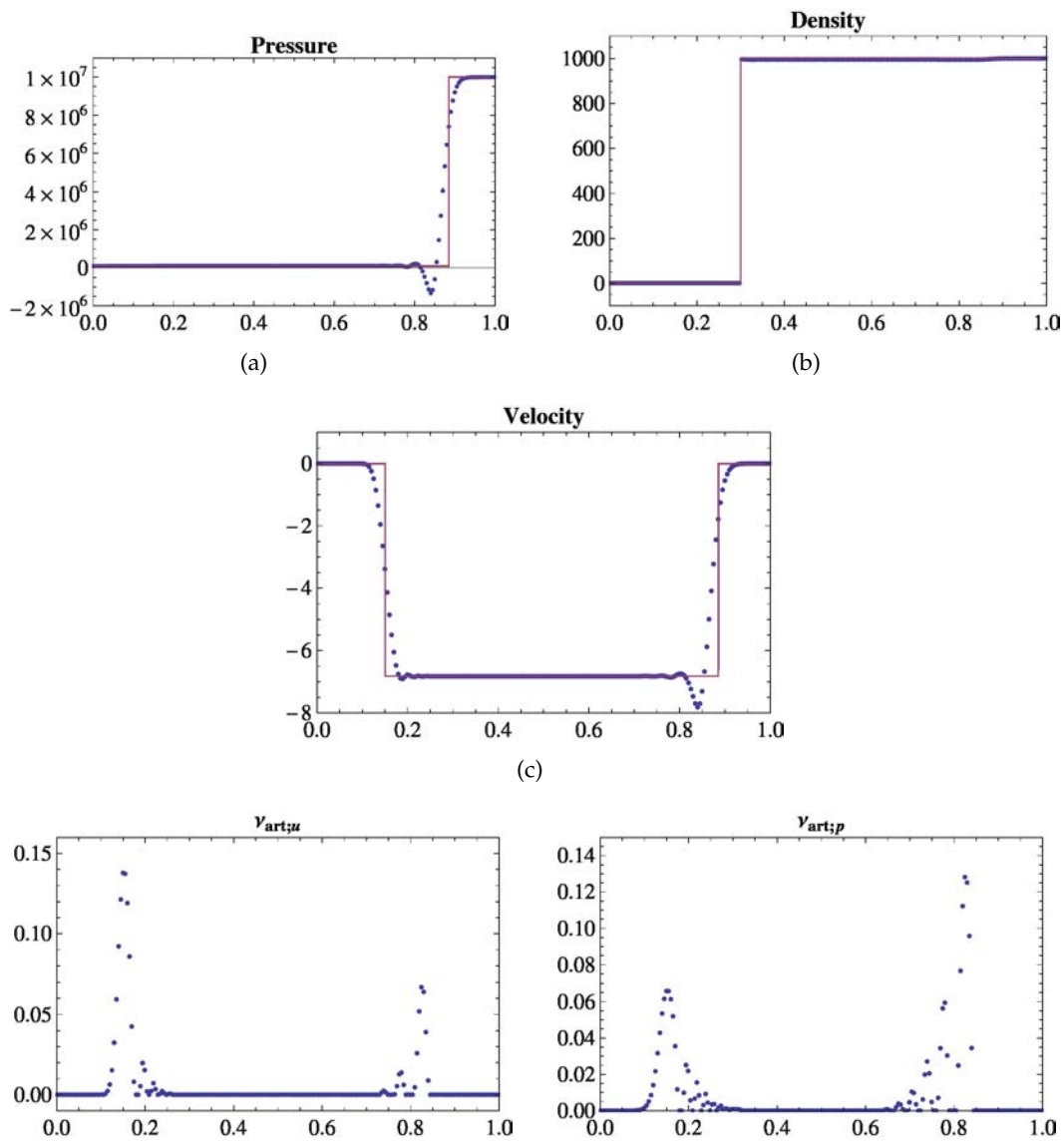
Figure 3.17: Air-water tube. Results for pressure, density and velocity are shown in figures *a* to *c* and are compared with the exact ones depicted in *solid* lines. Artificial viscosities are shown in figures *d* and *e*.
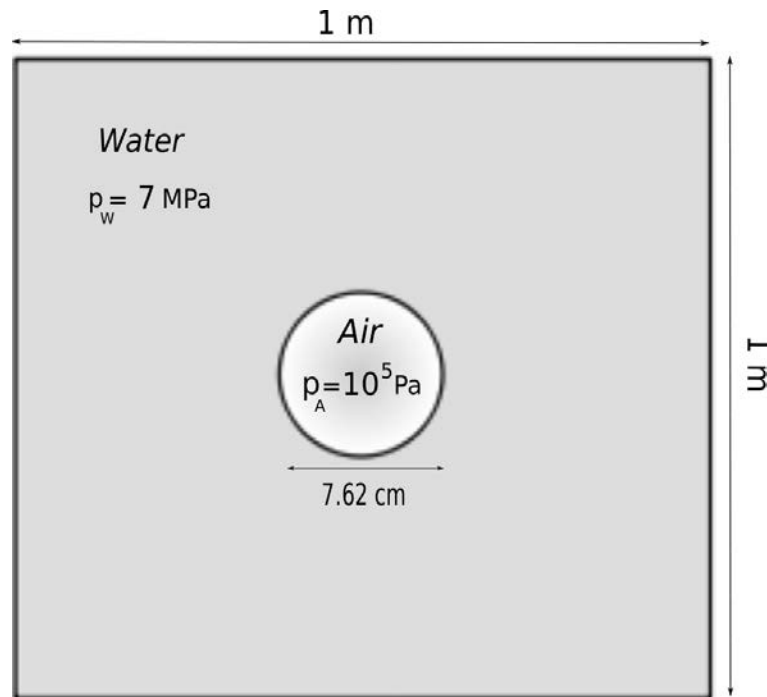
Figure 3.18: Underwater implosion setup

collapse. Note that a refined mesh is generated near the interface and derefinement occurs in the zones far from the interface.

The behavior of the bubble can be divided into three phases. The first one is the collapse of the air bubble due to the large external pressure exerting on it. Figure 3.21 depicts the pressure distribution along the radius and the interface position for different instances prior to the collapse. These converging pressure waves induce the shock at the center of the bubble. The appearance of the instabilities and deviation from the circular shape can be also seen in the evolution of the velocity in the x and y directions shown in Figure3.22. The velocity profiles have the same shape till some instances prior to the collapse but then a different behavior appears at the collapse moment when the instabilities occur.

The converging shock first rapidly increases the velocity inside the bubble but near the final convergence of the shock wave, the velocity is reduced due to the resistance of the gas to further compression. The flow reverses direction outward once the shock has impacted on itself at the center of the bubble. These observations are similar in both directions, however, the change in effective radius of the bubble measured along the two axial directions are different.

The collapse phase ends up with the maximum reduction in the radius up to 90 % of its initial value and the drastic increase in the air pressure (Figure 3.19a). Considerable change in the bubble radius and the appearance of instabilities in the air-water interface during a very short instance of the maximum pressure are quite noticeable (Figure 3.23).

The second phase starts with the shock wave, for an intensity of around 2500 times the initial air pressure, moving outward from the center of the bubble. The radius of the bubble starts to increase and the acceleration of the high pressure air into the water produces instabilities (Figure 3.23).
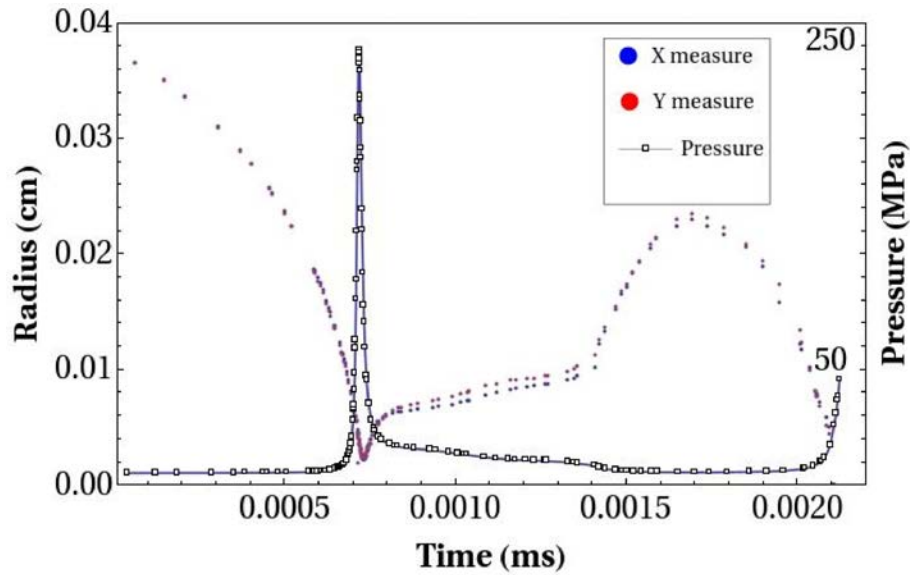
(a)
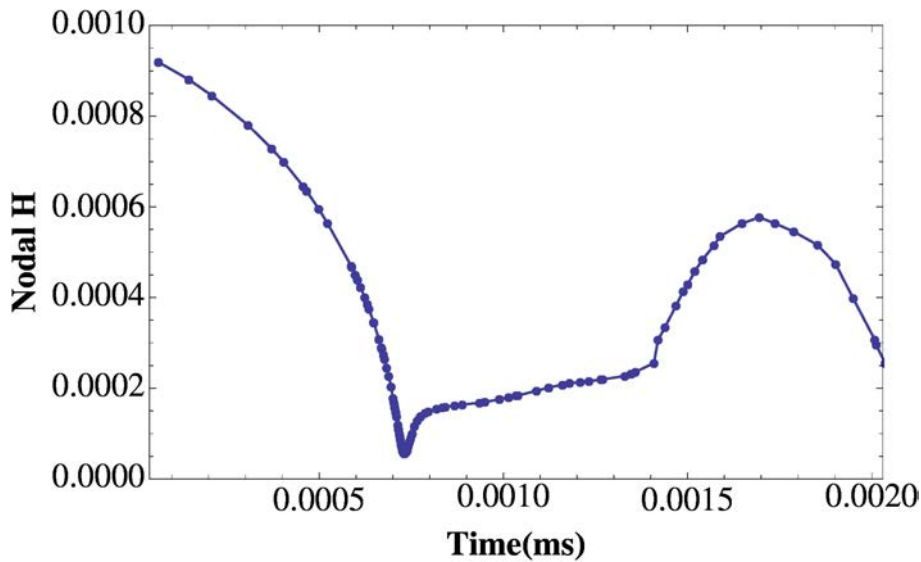
(b)

Figure 3.19: Time histories of a) "X", "Y" measures of bubble radius and pressure at the center of the bubble, b) Length parameter, H.

Surface instabilities appear in a very short period, less than 0.1 ms, and then the bubble recovers its circular shape with some oscillations remaining in its interface. The next expansion of the bubble starts at the final part of the second stage, as the result of the reduction in water pressure at the post shock zone. At the end of this stage the bubble has recovered 50% of its initial radius (Figure 3.19a), and air pressure has been reduced due to the rapid expansion of the bubble volume (Figure 3.24).

Last phase of the simulation is again an implosion similar to the first phase, but this time ends up with the rupture of the bubble as the result of the shape instabilities excited at this stage, (Figure 3.24). Note that the bubble almost recovers a circular shape at the end of the second stage.
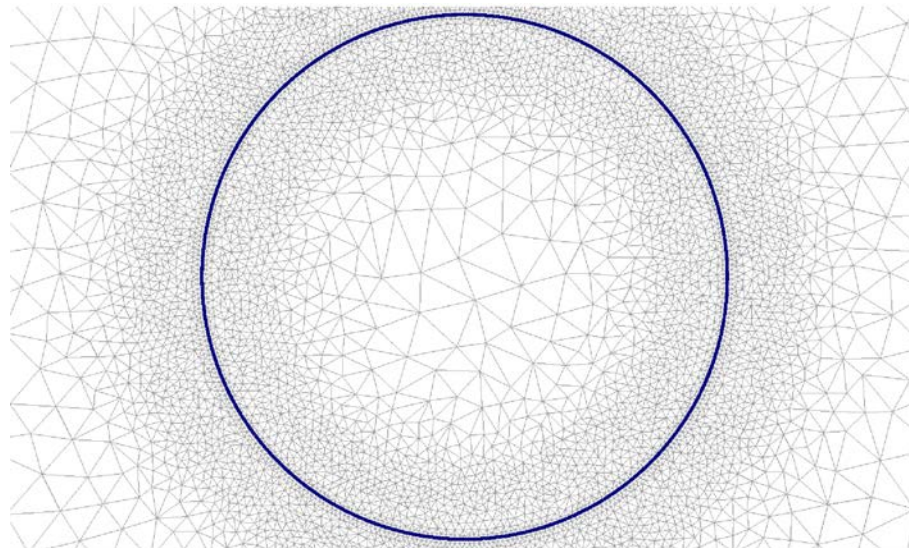
(a)
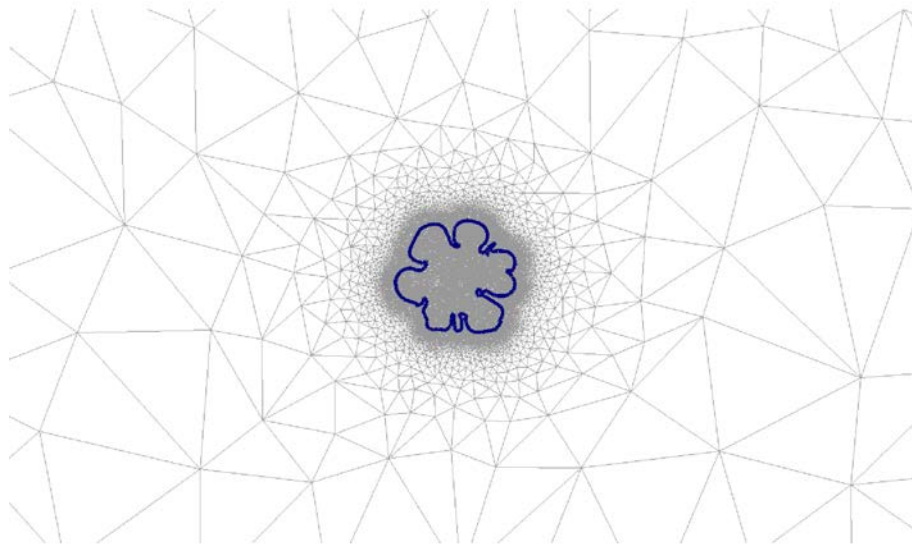
(b)

Figure 3.20: Adaptive mesh refinement, a) initial mesh near the interface, b) mesh at the moment of maximum contraction. Solid line indicates the position of the interface.

The parameters of this simulation correspond to the underwater implosion of glass spheres provided by Turner [129]. He detected the pressure pulse being created as the response of the implosion and traveling in water at 10.16 cm from the center of the glass and then studied the effect of the glass sphere on the pressure peak. The absence of a structure that separates air and water can cause up to 40% of error on the pressure peak [129].

The same setting is used by Farhat et al [31]. The water pressure computed in our simulation is compared with the experiment in Figure 3.25. The typical signature of all implosions that consists of a low flat negative-pulse followed by a sharp positive-pressure spike of 0.1ms duration can be seen in this figure.

Experimental results [129] report a peak value in the range of 27 to 32 MPa for the pressure pulse and depending on the failure rate of the structure. The same range is obtained by the simulations done using DYSMAS [129]. Numerical results presented in [31], using the AERO-F solver, report a maximum value of 27 MPa.

Our solution (labeled as PFEM in Figure 3.25) suggests a maximum peak of 35 MPa that is in good agreement with the experimental results both in the value and the signature. A more detailed study of the underwater implosion of cylindrical containers, accounting for fluid-air-structure interactions, is provided in [115].

3.5 DISCUSSION

The asphericity of the bubble can be attributed to many factors, such as the inherent dynamic instability of contracting bubbles, the proximity of solid boundaries or free surfaces, and buoyancy effects [42].

The DNS results presented in [77] for μ m size bubbles show deviation from spherical shape. In particular, at the final stage of the collapse the spherical bubble takes the ellipsoidal form. This is due to the excitation of nonspherical shape instability modes of the gas bubble during the violent collapse as already mentioned in the work of Wu and Roberts [135]. Brenner et al. [10] in their work on acoustic energy storage during SBSL, showed that the most easily excited instability modes of bubble are not spherically symmetric.

To better understand the behavior of the bubble at the final stage , let us consider a harmonic disturbance of the bubble radius as,

$$r_d = R + \Sigma b_n Y_n \qquad (3.61)$$
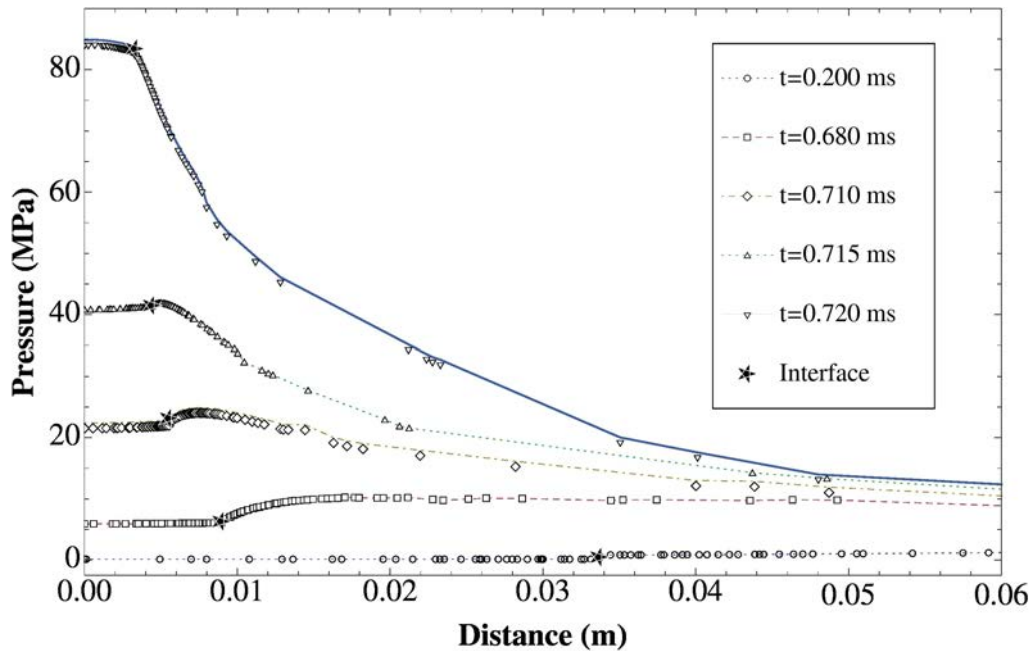
Figure 3.21: Formation of the shock at the center of the bubble
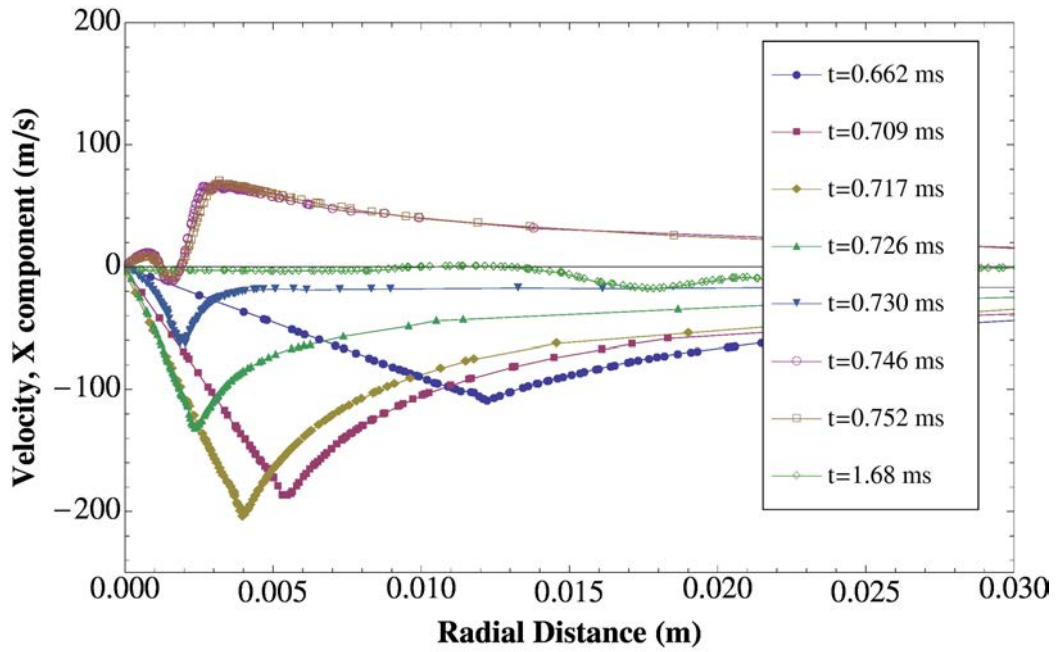
(a)
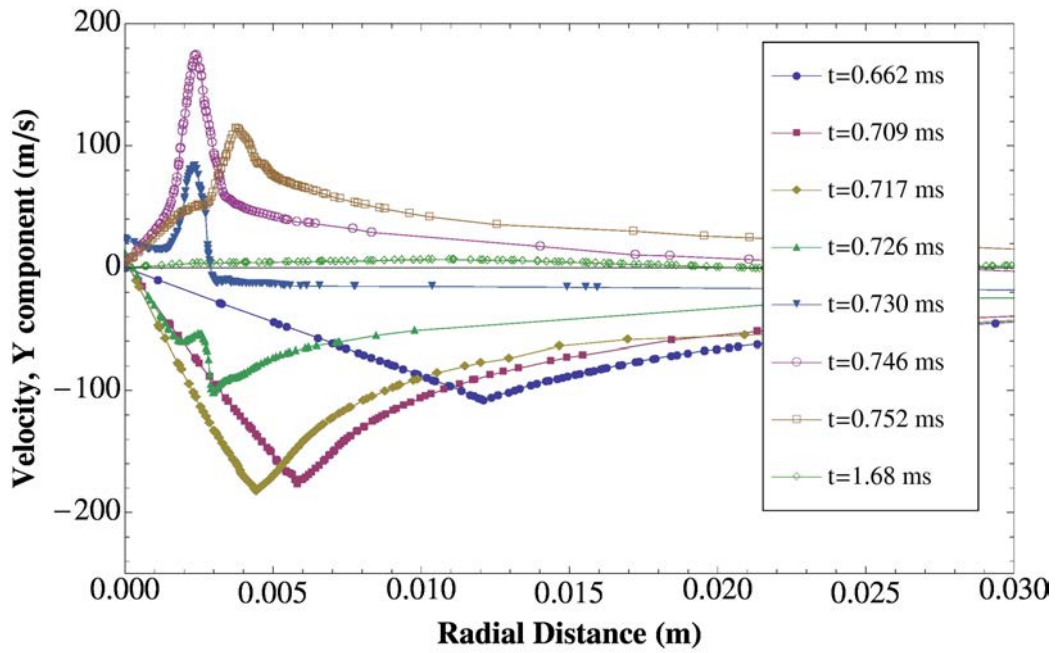
(b)

Figure 3.22: Bubble implosion. Velocity distributions a)X direction b)Y direction

Here R is the undisturbed radius, b_n is the amplitude of the harmonic n and Y_n is the circular harmonics of order n. The question is: *do the small harmonics, $|b_n| \ll R(t)$, grow,*
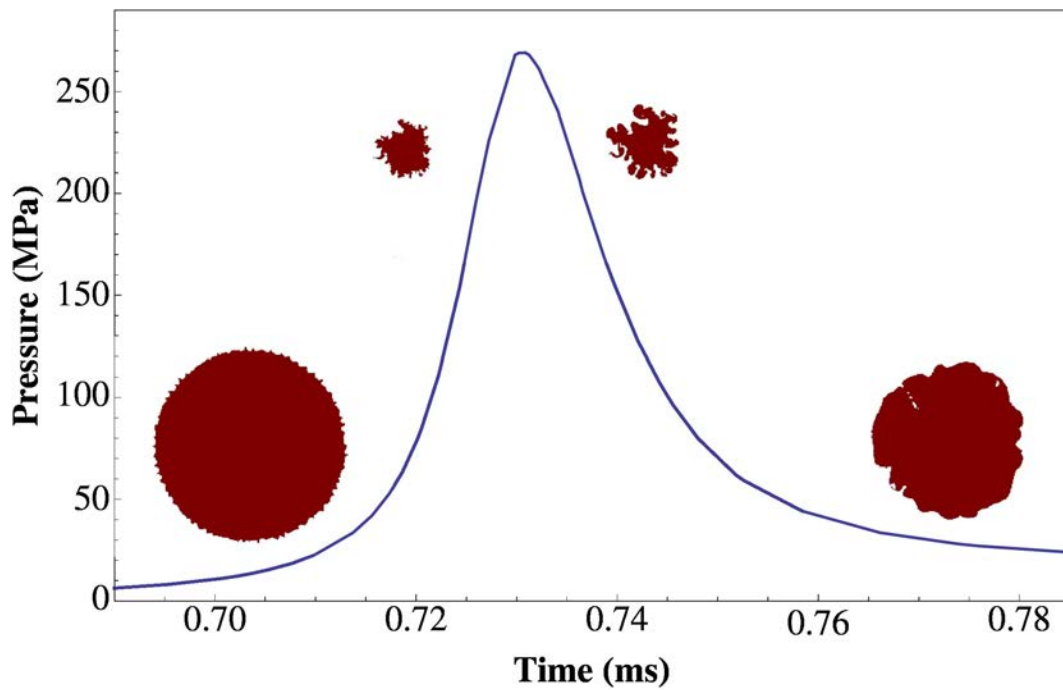
Figure 3.23: Bubble implosion. Appearance of the RT instabilities.

(a) 1.2 ms

(b) 1.48 ms

(c) 1.75 ms

(d) 2.0 ms
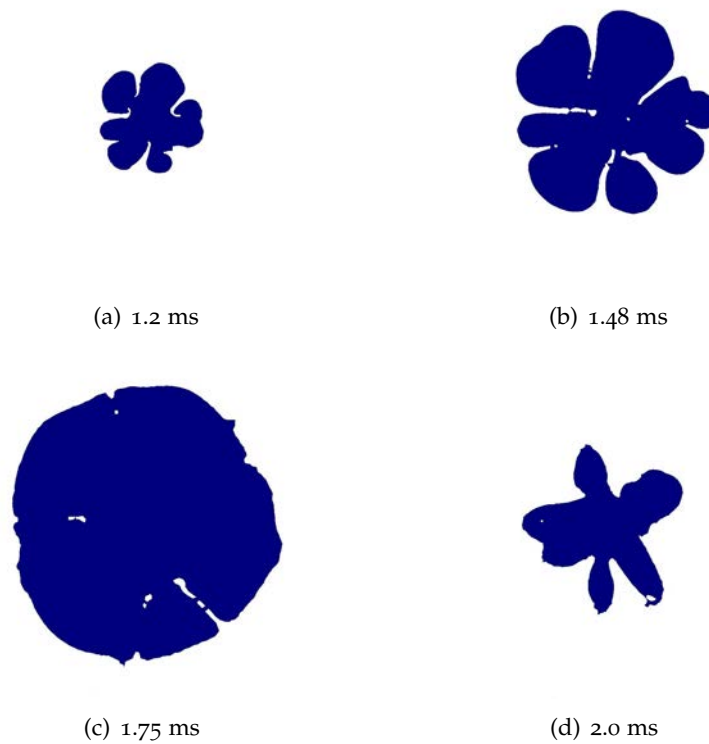
Figure 3.24: Expansion of the bubble and violent collapse
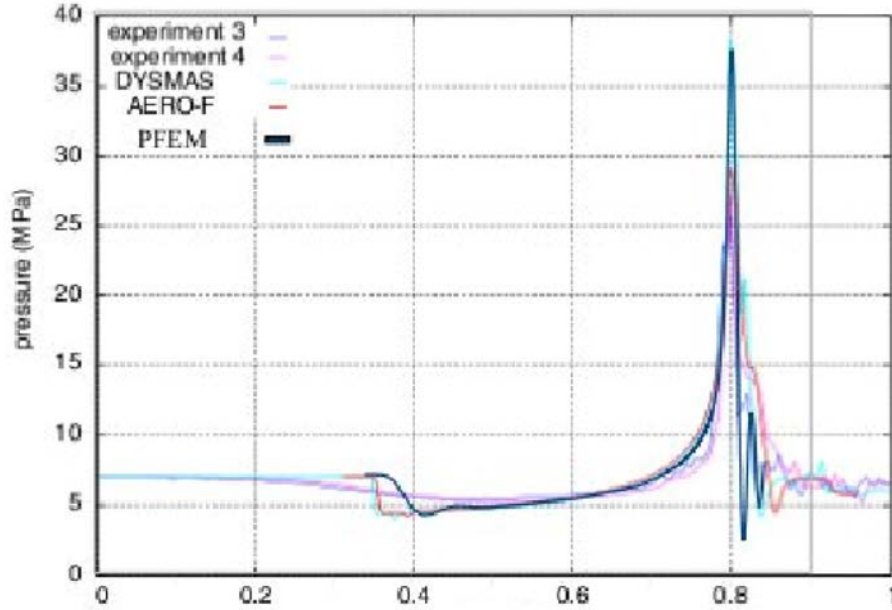
Figure 3.25: Time history of pressure at 10.16 cm from the center of the bubble

or diminish, during the collapse?. Recalling from chapter 2 and as is shown by the work of Plesset and Mitchelle [98, 99], for small perturbation, b_n, the growth in amplitude of the perturbation is governed by

$$\frac{d^2b}{dt^2} + \frac{3}{R}\frac{dR}{dt}\frac{db}{dt} - \left[\frac{(n-1)}{R}\frac{d^2R}{dt^2} - (n-1)(n+1)(n+2)\frac{S}{\rho_L R^3}\right]b = 0 \qquad (3.62)$$

Solving equation 3.62 with the well-known Rayleigh equation, see chapter 2, of the following from,

$$\frac{p_B - p_\infty}{\rho_L} = \frac{d^2R}{dt^2}R + \frac{3}{2}\left(\frac{dR}{dt}\right)^2 \qquad (3.63)$$

yields the evolution of amplitude with time.

Figure 3.26 shows the results obtained from this analysis. One can observe that as the radius of the bubble decreases, the distortion amplitude may oscillate in sign with increasing frequency and magnitude. It can be noted that higher harmonics are excited.

The results obtained in this section for *cm* size bubbles are compatible with the idea of excitation of higher modes during the collapse. In particular, results presented in Figures 3.23 and 3.24 show a mixture of higher mode excitations that leads to the shape instability from one side and RT instabilities from the other side.

The onset of interfacial instabilities can be attributed to a Taylor instability mode at higher interfacial acceleration. Specifically, these classic RT instabilities occur during the later stages of implosion when the gas accelerates into the liquid. There will be a significant destabilization as the bubble nears its minimum size, since the acceleration of the gas towards the liquid at this time is enormous. Note that this effect can be mitigated for small size bubbles, as the μm size bubbles of reference [77], by the fact
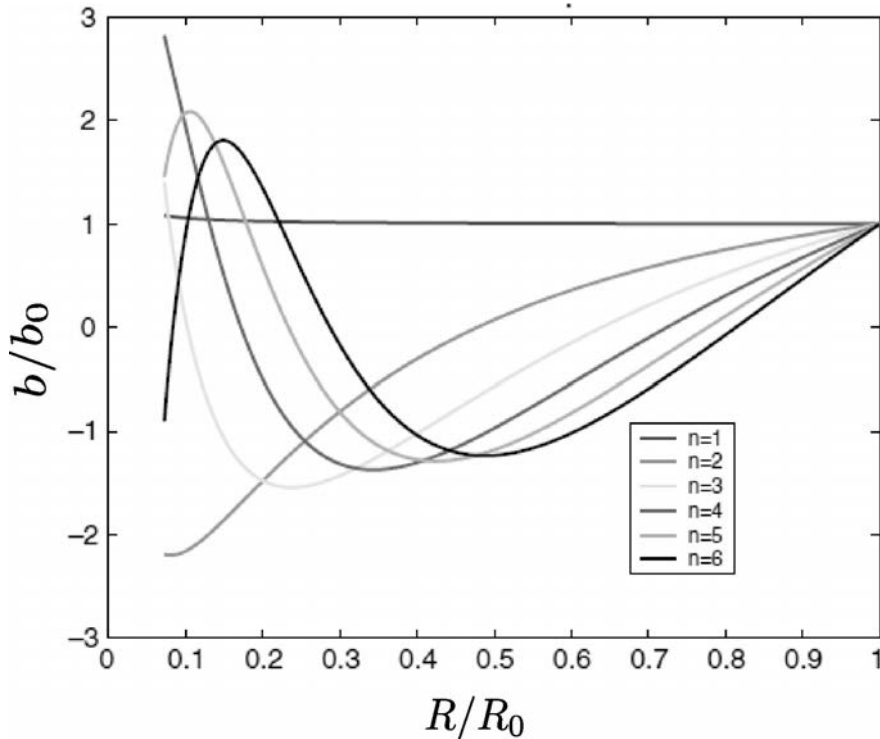
Figure 3.26: 1D analysis. Variation of distortion amplitude, b/b_0, as a function of R/R_0

that the gas density also increases significantly, while for larger bubbles this is not the case and interfacial instabilities appear.

This phenomena has been noted by many other researchers. Young [138] reported that during the final stages of bubble collapse during typical SBSL experiments, the bubble interface decelerates in preparation for re-expansion, leading to an extremely large relative acceleration of the gas with respect to the liquid, which tends to destabilize the interface.

Concerning the RT instabilities, the semi-analytical study performed by Bogoyavlenskiy [7] on SL bubbles ($R = 40\mu m$ and with water velocity of order 2-4 Mach) reveals that the time derivative of the shape perturbations can grow drastically as the bubble collapses, giving the dominant contribution to posterior evolution of the RT instability during the shock-like bounce. Actually the dominant contribution to RT instabilities comes from time derivative of perturbations rather than from the perturbation itself.

Our results show that the appearance of the RT instabilities are more pronounced in the first collapse, figure 3.23, while the second collapse, figure 3.24, is more affected by a fifth or sixth mode instability excitation.

3.6 CONCLUSION

We have presented a Lagrangian compressible framework for the simulation of fast dynamic compressible multi-flows with special interest in underwater implosion modeling. A variationally consistent form of the hydrodynamic set of conservation equations is considered to model the compressible air and water media. A nodally matched definition of the interface is used to follow its evolution. This facilitates the duplication of the pressure DOF at the interface to easily deal with the large initial pressure

jumps typical of implosion problems. The severe deformation of the interface, in addition to the large local motion of the fluids, require an adaptive mesh generation that respects the interface connectivities at each time step.

The formulation has been successfully tested for several benchmark problems and then has been applied to model the underwater implosion of cm size cylindrical bubbles. Numerical results show that the hydrodynamics of the bubble has three different stages. The first one is the collapse of the bubble that results in the reduction up to 90% in the bubble radius and an increase in the internal pressure up to 2500 times the initial pressure. At this point a shock wave is created at the center of the bubble and RT instabilities appear at the air-water interface. The pressure wave traveling in water is detected at 10.16 cm from the center of the bubble. Results for this phase have been successfully compared with experimental and numerical data. The second stage then starts by the expansion of the bubble, due to the high internal pressure, and the vanishing of the RT instabilities till the bubble recovers 50% of its initial radius and gains an almost circular shape. The third stage is again a collapse of the bubble volume that ends up with the rupture of the bubble initiated from a fifth mode instability that appears at the air-water interface.

4

CONTACT ALGORITHM FOR SHELL PROBLEMS

The final stage in the implosion of closed containers usually consists of the total collapse of the containers. It is, therefor inevitable to introduce a self-contact scheme to model the collapse. In this chapter we present a contact algorithm developed for modelling shell-to-shell frictionless contact. The material for this chapter is taken from our paper *A contact algorithm for shell problems via Delaunay-based meshing of the contact domain* [67].

4.1 INTRODUCTION

One of the major issues in contact problems is the definition and discretization of the contact surfaces. Many contact algorithms enforce the non penetration constraint on some collocation points. Hallquist et al. [4] proposed the simple idea that a specific slave node must not penetrate an opposing master segment. This node-to-segment approach is applied through a single pass algorithm that just checks for slave nodes, and so is prone to master node penetration, and also does not satisfy the patch test [30]. To cure this deficiency, a number of two-pass algorithms have been proposed. Although some of these algorithms satisfy the patch test, they may cause locking for certain configurations of the master and slave nodes.

Based on the so called mortar method [5] some segment-to-segment discretization strategies of the contact interface have been proposed [47, 49]. Segment-to-segment strategies are well suited for non-conforming interface grids and opposite to the node-to-segment approach enforce the constraint condition not at discrete nodes but along the entire coupling boundary and in a weak integral sense. Concerning the frictional contact, Heintz and Hansbo [44] proposed a method based on Nitsche's approach [80] that combines Lagrange multipliers and stabilization terms to reach a condensed matrix. This approach was first used by Wriggers and Zavarise [134] to solve frictionless small deformation.

In the context of the so-called Particle Finite Element Method (PFEM), Oñate et al. [92, 59] proposed a simple technique to define a contact domain where the contact constraints are imposed on the interacting interfaces. This Contact Domain (CD) technique has been applied for modeling fluid-solid and solid-solid contact situations in a variety of engineering problems [91, 28, 87, 14]. In this method the elements created during the mesh generation step are used to calculate the distance between the solid objects and determine the contact domain on an arbitrary minimum distance. Then an approximate contact force which is sufficient to avoid the penetration between the contacting bodies is activated. Because of such approximation only a rough estimation of the real contact forces can be provided. Oliver et al. [84, 41] refined such

simple contact model by using a constrained meshing technique and by allowing the contact domain to have zero thickness. Their formulation can be considered as a generalization of the method proposed by Heintz and Hansbo [44] for large deformation frictional contact problems.

The contact domain has the same dimension as the contacting bodies and provides a complete, continuous and non-overlapping pairing of the contact surfaces. It also overcomes some deficiencies of the node-to-segment pairings like dependence on the choice of master or slave faces and over constraining of some specific parings. The displacement field on the contact domain is naturally taken from the interface of the contacting bodies and the definition of the strain measures are straightforward.

The essence of the CD method is to discretize the domain within the contacting bodies by a finite element mesh, so to allow the accurate definition of the gap within the active contact area. The contact boundary condition is then enforced in the continuum by the use of Nitsche's technique and the discretized problem is solved following the Uzawa approach.

The resulting method was proved to be robust and efficient for a variety of demanding problems in computational mechanics. It was shown that the method succesfully passes the patch test and that much smaller penalty parameters (presented as stabilization in the reference works) are sufficient to prevent unwanted penetrations while guaranteeing locking-free behaviour. The resulting method was hence proved to be superior to penalty-based approaches for body-to-body contact problems.

Despite the attractiveness and the elegance of the approach, the CD method has still some disadvantages, related in particular to the need to performing a "shrinking" of the contacting domains to allow the correct definition of the contact volume. Even though such "shrinking" is only used in the meshing phase, and the nodes are brought back to their original position prior to the calculation of the contact forces, this represents a sensitive operation which should be performed with great care. A second, technical, disadvantage is the need for modifying the element formulation used in the discretization of the domain. The element formulation needs in fact to be modified so to be able to compute "consistent" contact forces depending on the gap intensity at the contact boundary. This implies that existing library of elements need to be modified to include such additional capabilities.

While such drawbacks are fully justified when dealing with body-to-body contact problems, since in such a context it is vital to enforce strictly the no-penetration constraint while avoiding the use of high penalty values, they may represent an unecessary burden in dealing with problems of different nature. Namely, if we focus on shell-to-shell contact, the use of Oliver's approach would require treating the shells as physical bodies and estimating the contact forces as they appear on the shell's surfaces. While this approach is possible, it leads to technical difficulties since the contacting surfaces are typically not discretized (only the mid-surface is represented in the FEM), and hence not easily available for meshing purposes. Furthermore, since shell formulations typically neglect the elastic deformation of the shell thickness associated to the normal forces, the computation of the contact forces by the Nitsche's method would imply a rather extensive reformulation of the shell element.

In the current work we will focus exclusively on the shell-to-shell frictionless contact, and define an algorithm designed to take advantage of the specific features of such setting, in the effort of defining a simple algorithm, but still appropriate for the

simulation of the problem of interest. The idea we will exploit sistematically is that shell's kinematics is described by the motion of its mid plane, and hence contact will be detected as soon as the midplanes reach a distance equivalent to the sum of the half-thicknesses of the contacting structures. Basing on this we will discretize, by the Delaunay approach, the volume enclosed between the contacting surfaces (that will be guaranteed to have non-zero thickness). Such "virtual volume" will be treated as elastic, with a suitably defined assumed strain, in all the areas in which the two shells are actually in contact.

The key difference with respect to the CD approach will be thus in the nature of the constraint: while for body-to-body contact it is needed to impose a "rigid" contact, which needs furthermore to be enforced on a domain of zero thickness, in the case of shell-to-shell contact we will consider the elastic deformation of a "virtual solid" enclosed within the shell's midplanes. The inclusion of such elasticity will thus provide automatically a suitable (and physically based) penalization strategy, thus avoiding the need of using Nitsche's approach in applying the contact forces.

The contact algorithm we propose is designed to handle arbitrary deformations of the shells involved, nevertheless we will assume in all of the work that the variation of the thickness induced by the contact forces can be considered "small" although not necessarily infinitesimal. This assumption is justified by considering that for shell structures, the stiffness in the normal direction is typically orders of magnitude smaller than the membrane one.

In the following, we first explain the contact criteria and the contact forces proposed for the shell contact. Then a closest point projection method is applied to compute the distance within different types of contact elements that appear in the discretization. Next the rotation-free triangular shell element used for discretizing the shell structure is described. Finally some tests are provided to examine the efficiency of the proposed contact method in combination with the rotation-free shell triangle.

4.2 CONTACT CRITERIA AND CONTACT FORCES

The definition of a new contact algorithm implies the choice of a contact criteria and of a procedure for calculating the contact forces. Both of these steps rely on comparing the "distance" between the contacting bodies with a suitably defined "critical distance" which allows us measuring the amount of penetration and consequently estimating the contact force.

In dealing with volumetric objects, contact is typically measured by comparing the position of the body surfaces so that contact is detected once the distance of the surfaces assumes the value of zero. Some care is needed in applying this simple idea to contact problems involving contact between two shells, since the definition of kinematics of the shell is (normally) tied to the movement of the shell's mid-plane.

In our approach, the critical distance, l, is taken as a function of the shell's thicknesses so that contact is detected once the mid-planes arrive at a distance corresponding to the sum of the shells' half-thicknesses[1], i.e.

$$l = (t_1 + t_2)/2 \tag{4.1}$$

---

[1] The algorithm can be easily extended to the shell-solid body contact by setting one of the thicknesses to zero. However this is not considered in the current work.
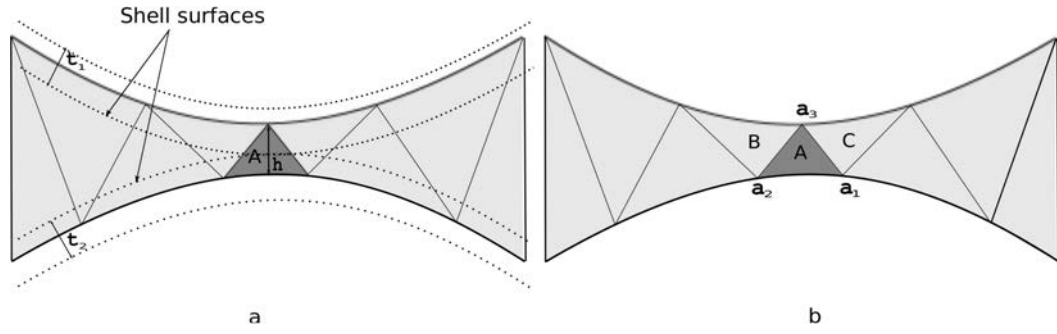
Figure 4.1: a) Shell thicknesses t_1 and t_2 and actual distance between mid-planes, h. b) Element A and its neighbors B and C

The distinctive feature of our contact procedure is the use of a finite element (FE) discretization of the space between the shell's mid-planes so that an assumed strain approach can be defined within this area and the contact forces can be calculated accordingly. The fact that contact happens when the shell's mid-planes are still at a finite distance, guarantees that the discretization of the contact domain is well defined and in turn provides a substantial advantage both for the integration of the contact forces and the definition of the contact strain.

Figure 4.1 describes the situation: the whole area between the contacting shells is discretized, however only within a small portion of such domain (element "A") the contact condition is actually introduced. The portion of the computational domain covered by elements of the contact discretization will be named as *potential* contact domain (light grey in Figure 4.1a), while the subset of the elements of such domain for which the contact condition is fulfilled is identified as *active* contact domain (dark gray in Figure 4.1a).

Our proposal for the calculation of the contact forces is to define a strain of the type

$$\boldsymbol{\epsilon} = \mathbf{n} \otimes \mathbf{n}\, \epsilon \tag{4.2}$$

within each element of the *active* contact domain. This corresponds to assuming a 1D strain in the normal direction given by the formula, $\epsilon := (l^2 - h^2)/(2l^2)$ which can be recognized as the Green-Lagrange strain computed in a direction $\mathbf{n}$.

For all the active elements in the contact domain we define a characteristic distance h and a normal direction $\mathbf{n}$. The computation of the contact forces follows as a consequence of the application of the Galerkin method to the elements within the *active* contact domain. By assuming that contact elements behave elastically and inherit the elastic properties of the shells in contact, the stress tensor, $\boldsymbol{\sigma}$, is computed as,

$$\boldsymbol{\sigma} = \mathbf{D} : \boldsymbol{\epsilon} \tag{4.3}$$

where $\mathbf{D}$ is the fourth order elastic constitutive tensor[2]. Contact forces corresponding to the stress field can be obtained by integration, as

$$F_i^I = \int_{\Omega_e} \frac{\partial N_I}{\partial x_j} \sigma_{ij} \, d\Omega_e \tag{4.4}$$

Here F_i^I is the i_{th} component of the vector force related to the node I and N_I is the shape function at node I. σ_{ij} are components of the stress tensor $\boldsymbol{\sigma}$. Tensor formalism for the repeated indices is applied.

The above definitions still fail to prescribed exactly a methodology for the calculation of the distance, h, and of the normal, $\mathbf{n}$, used in the strain definition. We exploit the idea of the "closest point projection" performed within each element to compute the distance. Next section explains the computation of h and $\mathbf{n}$ in detail for 2D and 3D problems.

4.3 DISTANCE AND NORMAL

In each contact element, contact happens when one node starts to penetrate the opposite face or when two edges are going to cross each other. The first step for computing the interaction distance is the detection of the penetrating node or the crossing edges in each element. This is done via the neighboring information provided by the mesher. Once the tetrahedalization is built, the list of *neighboring* elements can be computed (or directly received from the mesher) providing information on tetrahedra that share a given face in the mesh.

Neighboring elements are stored in a standard way, so that they are identified by the index of the node opposite to the accessing face. As an example, consider element A in Figure 4.1b with three corners a_1, a_2 and a_3 and two neighbors B and C. According to the neighbor list, element A has the neighbor B assigned to the corner a_1, the neighbor C assigned to the corner a_2 and obviously no neighbor assigned to the corner a_3. The corner that has no neighbor assigned to it, is the penetrating node and we call it the *free corner*.

The remaining corners build the *face*. Most of the elements of the discretization have the *free corner* on one of the two planes of the contact and the *face* on the opposite one. An example is node a_3 in Figure 4.1. For this standard configuration the normal, $\mathbf{n}$, is defined as the normal to the *face*. Such configuration will be called "canonical".

Unfortunately, other configurations may rise within the discretization. Particular cases may appear for which a contact element may have two of its vertices on one side of the contact face and the other two on the opposite side. This second class requires additional care in the definition of the normal and is therefore identified as "non-canonical". The discretization is *constrained* to respect the given surface meshes, in the sense that it is not allowed to add additional nodes and has to respect the given surface discretization.

In our implementation the Tetgen [114] software is used for defining a constrained Delaunay tetrahedralization of the contact space. Figure 4.2 shows the discretization

---

2 We recall that the proposed setting could be easily extended to the case of two shells of different thicknesses, or even different material properties, by considering the analogy of two springs in series.

(a)   (b)
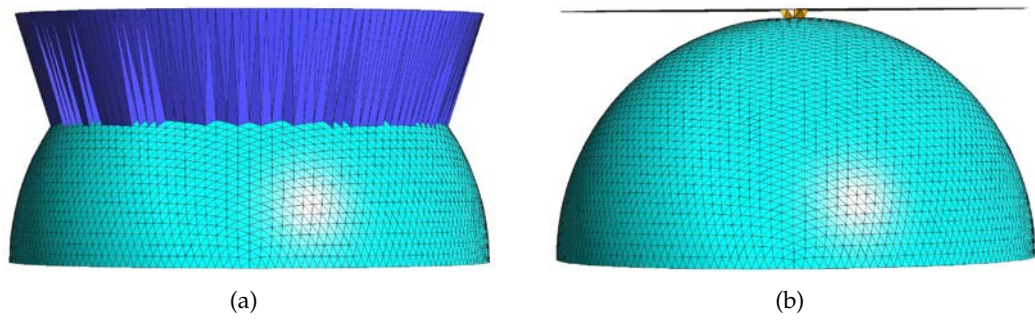
Figure 4.2: a) *Potential* contact elements, b) *Active* contact elements

provided by Tetgen for an example that is later studied in this paper. The *potential* contact elements and the *active* ones, that satisfy the contact criteria, are shown in Figure 4.2a and Figure 4.2b, respectively.

The following sections will describe in detail the calculation of the distance and the normal for the "canonical" and "non-canonical" subclasses of elements attempting to cover all possible cases.

4.3.1 Canonical elements

In each *canonical element*, the *free corner*, i.e. the one that has no neighbor assigned to it, belongs to one of the shells in contact and the other corners, which form the *face*, belong to the opposite shell. The possible contact occurs between the *free corner* and the *face* and therefore the distance between them defines h.

Figure 4.3 depicts two possible cases that may appear for *canonical elements* in 2D. They are distinguished by the position of the image of the *free corner* on the *face* plane. For both of these cases height defines the characteristic distance h and the normal to the *face* plane defines $\mathbf{n}$ (see Figure 4.3).

(a)   (b)
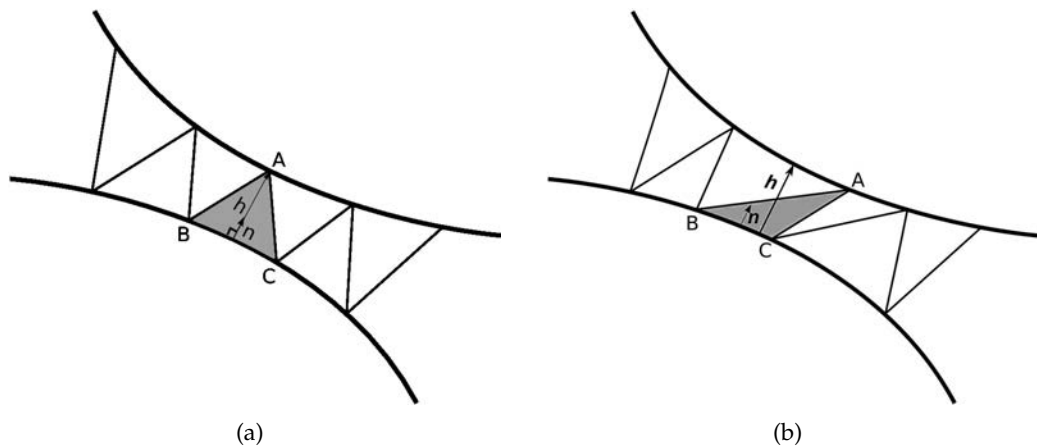
Figure 4.3: "Canonical" contact elements

The same idea is extended to 3D "canonical" elements. We need first to distinguish the *free corner* and the *face* and then calculate the distance and the normal. In each
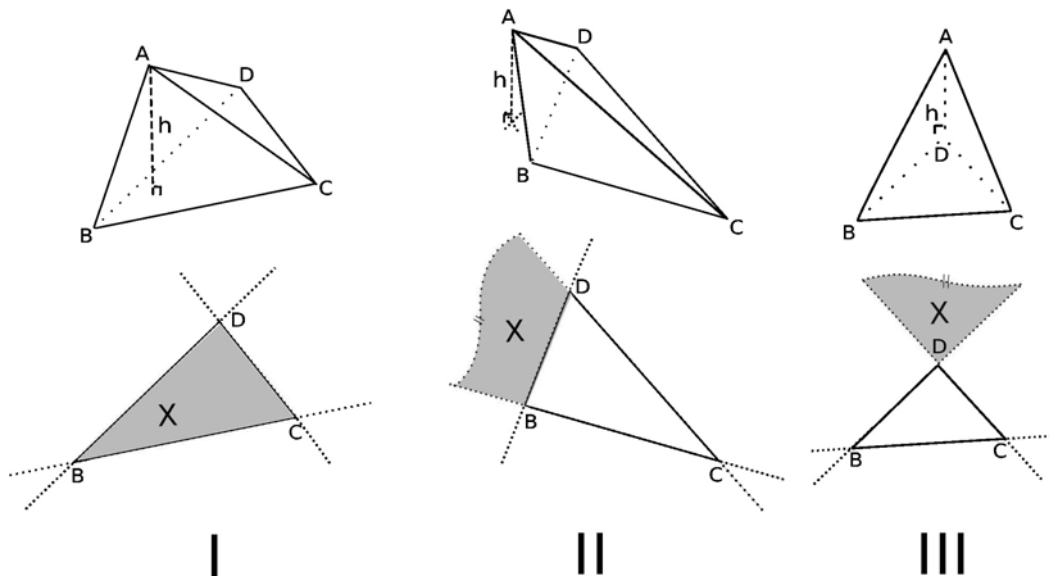
Figure 4.4: Vertex-edge combinations

tetrahedron the corner that has no neighbor assigned to it is labeled as the *free corner* and the remaining corners that belong to the surface mesh build the *face*.

In general three *free corner - face* combinations can be distinguished. The first case is the 3D counterpart of the first case in 2D. The second and the third cases somehow stem from the skew element case in 2D. These cases are shown in Figure 4.4.

It is obvious that three zones can be distinguished in the *face* triangle. The zone inside the *face* triangle, the zone outside the triangle but near the edges and, finally, the zone outside the triangle and near the corners. These zones are shown in gray color in Figure 4.4. In this figure A is the *free corner* and BCD△ the *face*. The image of the *free corner* on the *face* plane that falls in one of the gray zones is shown by the cross sign X.

In case of *canonical element* and for all of these three combinations, h is defined as the length of the altitude and **n** as the normal to the face plane (Figure 4.4). Small perturbation to the definition of h is used in case of *non-canonical* boundary elements.

4.3.2 *Non-canonical elements*

Although constrained discretization of the contact domain mainly results in *canonical* type elements, some elements may appear that either have no *free corner* or have more than one *free corner*. **Sliver**, **corner** and **boundary** elements, see Figures 4.5a, 4.5b and 4.5c, are examples of elements that have more than one *free corner* and may appear both in 2D or 3D cases.

On the other hand, and just in 3D cases, elements without any *free corner* may appear. These elements that represent a segment-segment contact case are called "two by two" elements because they have two nodes on one of the contact shells and two nodes on the other one (Figure 4.5d).

4.3.2.1 *Sliver, corner and boundary elements*

In each triangulation, or tetrahedalization in 3D, sliver elements (completely flat elements) may appear (Figure 4.5a). As mentioned these elements have more than one *free corner*, B and C in Figure 4.5a, and therefore can be simply detected by the use of the neighbor list provided by the mesher. As the application of the contact criteria on these elements may result in fake contacts, they are eliminated from the potential contact domain.

On the other hand, and similarly to sliver elements, corner elements, like the one shown in Figure 4.5*b*, have also more than one *free corner*. These elements appear in self-contact problems and have to be kept to avoid the local corner penetration.

A geometrical condition is used to distinguish between slivers and corner elements. We define slivers as very flat elements for which the image of each of the *free corner*s falls outside of the corresponding *face*. Examples are the *free corner* A in Figure 4.3b, or cases **II** and **III** in Figure 4.4. In contrary, we introduce the concept of corner element as the one for which the image of each of the *free corner*s falls inside of the corresponding *face* (Figure 4.5*b*), and therefore it is easy to distinguish between a sliver and a corner element.

Last member of this family is the boundary element as shown for the 2D case in Figure 4.5c. This type of element rarely appears and is only generated in the external boundaries of the contact zones by the Delaunay discretization. They are always very skewed and if for these elements the characteristic distance h is chosen as the height, wrong contact will be detected. The possible configurations of the skew elements in 2D and 3D are shown in Figures 4.3b and 4.4 **II** or **III**, respectively.

Two possible remedies can be taken to treat this kind of elements. One choice is that, as the exclusion of these boundary skewed elements does not affect the detection of the contact, they can be simply omitted from the *active elements* pool. Second choice is to modify the computation of the characteristic distance h for these elements. We propose that instead of the height, the distance between the *free corner* and the *face* itself is chosen as the characteristic distance h. This means that for the boundary element of Figure 4.5c, the distance between the edges "A" and "B" is taken as the characteristic distance h. The same idea is applied for the 3D cases.

4.3.2.2 *Two by two elements*

These elements have two nodes in one of the contact shells and two nodes on the other one. Two by two elements identify a segment-segment contact and only appear in 3D cases (Figure 4.5*c*).

One possibility to calculate the *distance* and the *normal* for these elements is to search for the minimum distance between the two contacting segments. Unfortunately such approach has difficulties for detecting which segments are in contact. The neighbor list can not provide any information to distinguish the segments in contact, because all corners now have neighbors assigned to them.

We use the information facilitated by the neighbor elements of each two by two elements to define h and **n**. As the contact in each of the neighbors inevitably means the contact of the two by two element also, we choose the neighbor element that has the minimum h and adopts this value of h and the normal **n** for the two by two elements.
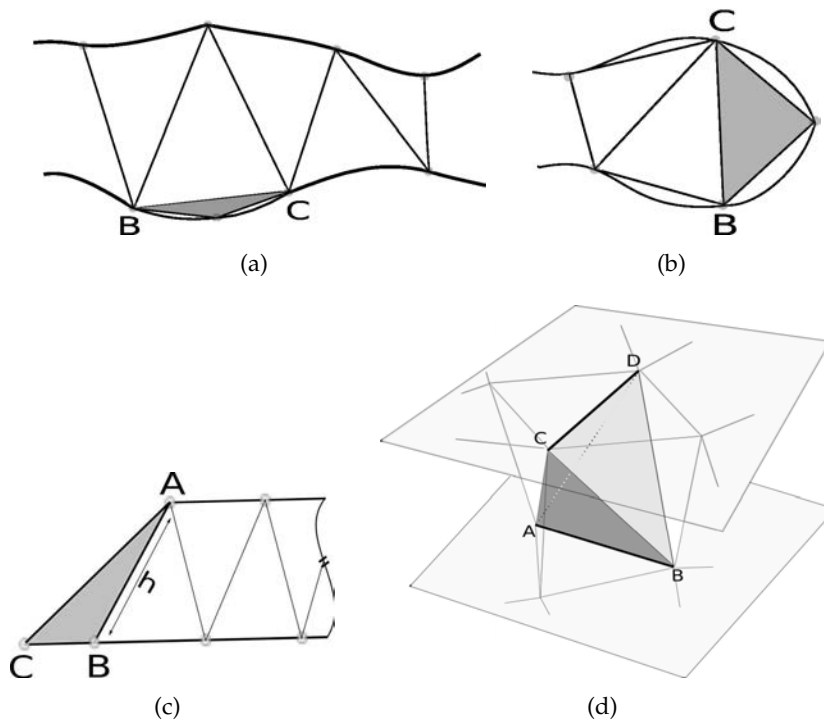
Figure 4.5: *a*) Sliver *b*) corner element *c*) boundary element *d*) two by two element, in which
segment *AB* belongs to the one contact surface and segment *CD* to the other one

4.3.3 *Region attributes and multi-object contacts*

Up to now we have described the computation of the characteristic distance for each of
the element within the *potential contact domain*. We finish this section by highlighting a
detail that is important for multi-object contact problems. As mentioned in Section 4.3
the detection of the *free corner* and the *face* is necessary to calculate the characteristic
distance h for each *potential* contact element. If the geometry of the problem consists
of a single closed volume, like the self-contact problem of Example 4.6.6, the neighbor
list provided by the mesher is sufficient to detect the *free corner* and the *face*. In these
cases, the exterior surface of the closed volume is the surface mesh of the shell. Hence,
as all nodes in the discretization belong to that mesh, the surface nodes are *free corner*s
candidates.

The situation gets more complicated, however, when different closed volumes are
involved. This may happen for multi-object contacts or even when an exterior box is
used to close the inter-bodies volume. In these cases the shell surface mesh is not any
longer an exterior boundary but becomes embedded in the volume mesh. Although
the mesher still respects the shell as an interior boundary, no *free corner*s can be any-
more distinguished by the neighbor list.

We use the *region attribute* facility provided by Tetgen [114] to solve this problem. *Re-
gion* is simply defined as the interior of a closed volume. Each closed volume can have
an attribute assigned to it that is also inherited by the discretization of the volume. In
this way each potential contact element knows its *region attribute*. This property yields
a more precise definition of the *free corner*:
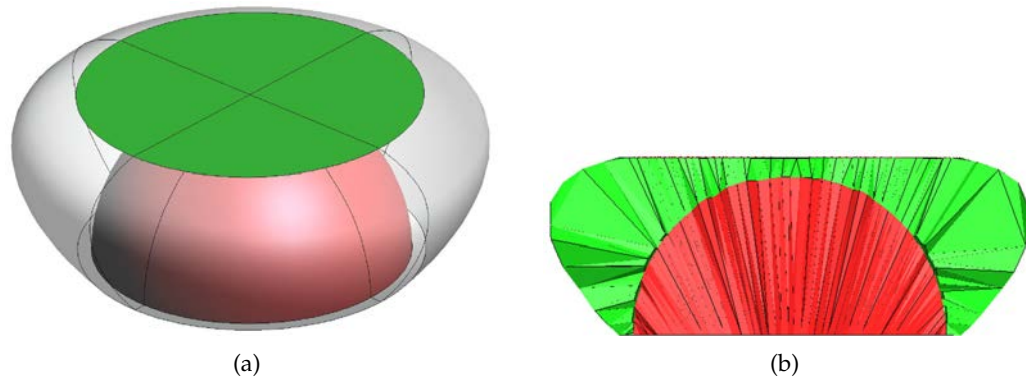
Figure 4.6: *a*) Initial geometry with bounding box *b*) *Region* attributes shown in a mid-plane.

> In each potential contact element, the corner that has no neighbor assigned
> to it, *with the same region marker as the element*, is defined as *free corner*.

Therefore, to detect the *free corner*, neighbors are searched inside each *region* and not
in the entire domain. This minor change provides enough information to detect both
self-contact and inter-body contact situations.

Figure 4.6*a* shows the initial geometry for a cap compression example that is later
studied in the paper. The geometry is not closed and an arbitrary bounding box is
created to close it. Two regions, marked by the mesher and assigned to the *potential*
contact elements, are shown in Figure 4.6*b* through a mid-plane cut of the original
geometry.

4.4   SUMMARY OF THE CONTACT ALGORITHM

Table 4.1 summarizes the contact algorithm. In the first step the surface mesh of the
shell is saved. In cases when this surface mesh is not closed or multi-body contact
occurs, an artificial external box is added to provide a closed volume. The second step
is an optional one and is necessary for cases when more than one closed volume is
involved. In such cases, one internal point inside each closed volume is passed to the
mesher to assign related region attributes to the elements in that zone.

Constrained discretization of the domain is done respecting the surface connectiv-
ities and providing neighbor and region attribute lists. Then a loop over all *potential*
contact elements is performed for computing, the characteristic distance h and the
normal vector **n** for each contact element as explained in Section 4.3.

Next, the contact criteria is verified in each element by comparing distance h with
the mean thickness value. The strain field and the contact forces are computed in each
active contact element and are directly assembled into the global system. As all nodes
of the contact elements belong to the surface mesh the assembly is straightforward.
In this way the contact routine can be easily coupled with the shell routines, or other
modules of a fully coupled system.

Finally, the entire system is solved implicitly or advanced in time using an appro-
priate time integration scheme. This approach has been tested by the authors for fully
coupled fluid-structure-interaction problems [115].

Table 4.1: Contact algorithm

- Save surface mesh of exterior and all interior boundaries.

- Assign *Region attributes*.

- Discretize the contact domain to get *potential* contact elements.

- Search for the element neighbors inside each region.

- **For** $n = 0, ..., n_{ele}$

    - Count free corners f_c.
    - **If**($f_c == 1$):(*Canonical* elements)
        . Calculate distance, h, and normal,n.

    elseif($f_c == 2$): (*Slivers, corners and boundaries*)
        . for *slivers* $h = \inf$.
        . for *corners* and *boundaries* calculate, h and n.

    else (*Two by two* elements) :
        . Search for the neighbor element, that has minimum h.
        . Assign $h = h_{ele}$, $n = n_{ele}$

    - Set $l = (t_1 + t_2)/2$.

    - **If** $h \leqslant l$ (contact criteria):
        . Build assumed strain field $\epsilon = \mathbf{n} \otimes \mathbf{n} \|\epsilon\|$.
        . Calculate contact forces.
        . Assemble the forces to the shell nodes.

- **End** loop over *potential contact elements*.

4.5 ROTATION-FREE SHELL TRIANGLE

Although many thin shell models exist in the literature, only relatively few successfully deal with triangular meshes and even less can deal correctly with large deformations and rotations. The contact model here proposed could be used in principle with any shell formulation. In this work we have implemented it with the Enhanced Basic Shell Triangle (EBST) introduced by Flores and Oñate [34].

The EBST falls within the category of the so called "rotation-free" shell elements originally derived by Oñate et al. [93, 89]. The key feature of the EBST element is the use of a patch of elements for estimating the shell curvatures and the membrane strains. This allows avoiding the use of rotations at the price of enlarging the stencil of the element stiffness matrix.

An important property of the EBST formulation is the possibility of handling large displacements and large deformations in a relatively simple manner.

Early formulations of rotation-free shell elements [93, 88] recovered the curvature within the central element by estimating the relative rotation of the triangles that share the different edges in the mesh. The original EBST formulation has been improved [34, 89] by introducing a non-local quadratic function constructed over the whole patch which is used for computing the curvatures and the membrane strains at the mid-side points of the central element. Such improved kinematics allows the
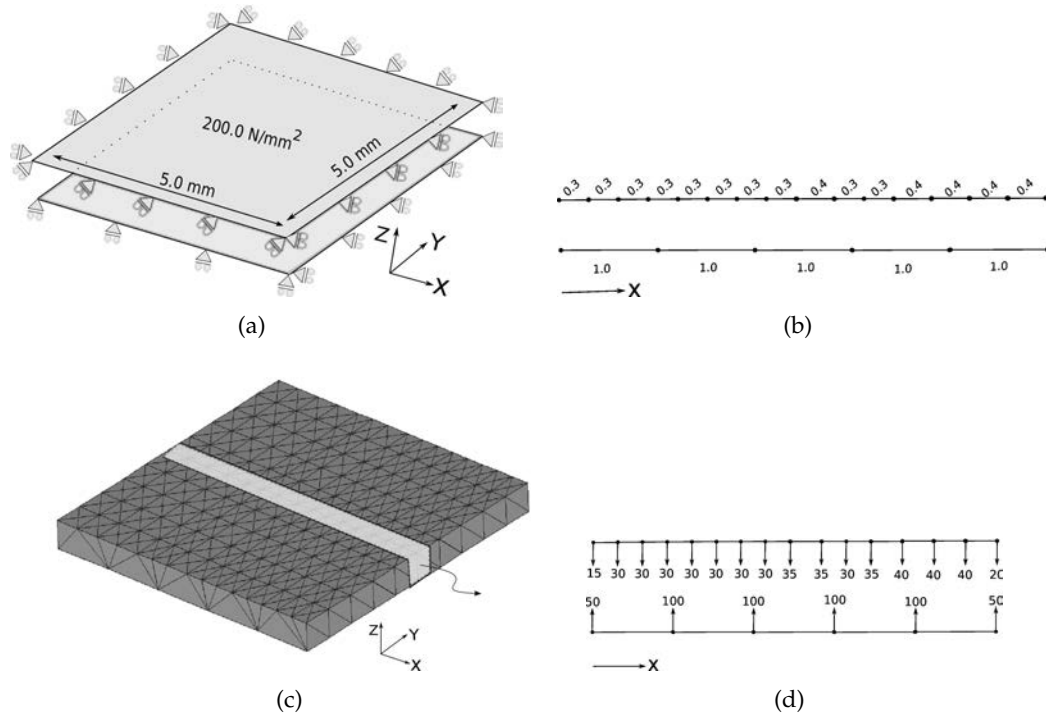
Figure 4.7: Patch test a) setup of the test b) discretization in *x*-direction c) *active* contact elements d) contact forces.

natural definition of a volume around the mid-plane, which in turn can be used effectively for the integration of the stresses across the thickness, thus allowing the correct representation of non-linear material models. The absence of rotations also allows us using standard 3D strain measures, thus effectively avoiding problems related to arbitrarily large rotations which may appear during the computations. A summery of the formulation of the EBST rotation-free element is presented in Section 5.2.2. Further details can be found in [34, 89].
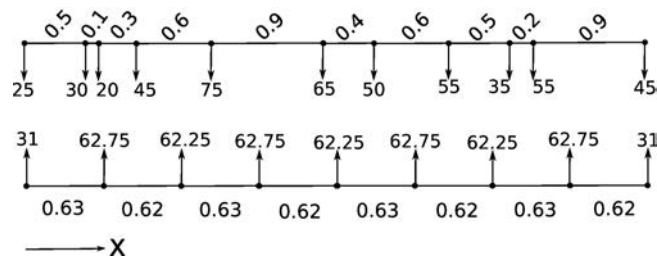
Figure 4.8: Unstructured discretization in *x*-direction and the distribution of the computed consistent nodal forces.

In this section some numerical examples are provided to verify the proposed contact algorithm for shell problems. The ability of the contact scheme in exact transmission of the uniform distributed loads along non-conforming contact meshes is tested via a 3D extension of the so-called patch-test [22]. Then, the effect of the mesh refinement on the maximum normal stress and distribution of the contact zone is studied in a modified Hertzian contact for shells. The third example is the compression of a spherical shell between two rigid plates. The shell material undergoes severe elasto-plastic deformations and the multi-contact between the top plate and the shell, and then the bottom plate and the shell are successfully detected. In the next example the contact algorithm is tested for the high velocity impact between two cylindrical tubes. Then, we study the elastic impact between a high velocity ball and a clamped beam modeled by shell elements. The good results obtained verify the behavior of the shell in high velocity contact induced motion. We finish this section by studying the buckling of a cylindrical tube under external pressure. The surface nodes of the shell are slightly perturbed to initiate the second and the third buckling modes of the cylinder. Self-contact zones are detected at the beginning of the contact as well as during the contact until the end of the simulation when the cylinder is totally collapsed. Region attributes, explained in Section 4.3.3, are activated for the first and second examples where multi-contact situations appears.

4.6.1   *Contact patch test*

A 3D extension of the contact patch test for shell to shell contact as proposed in [22] is considered here. Figure 4.7a shows the schematic view of the test. Both shells have a thickness of 0.5 *mm*. The non-conforming discretization proposed in [22] is considered in the *x*-direction (Figure 4.7b).

A structured discretization is considered in the *y*-direction (10 divisions) and this facilitates the computation of the contact forces. Active contact elements are shown in Figure 4.7c. As the uniform load distribution provides uniform displacement field, all the contact elements between top and bottom shells are activated. The scaled computed contact forces along one of the *x*-direction strips, see light gray strip in Figure 4.7c, are depicted in Figure 4.7d. The strip has the length equal to 0.5 *mm* that results in distributed load equal to the 100 *N/mm* along the strip.

The contact patch test is properly passed and the resulting consistent nodal forces coincide with the exact ones. The same behavior is obtained for the other strips in the *x*-direction.

We continue this test by considering the same configuration this time having a non-conforming and totally *unstructured* discretization in one direction as shown in Figure 4.8. The top plane is discretized randomly in the *x*-direction and the bottom plate has a semi-structured mesh. A Structured mesh, the same as for the previous case, is used in the *y*-direction. The computed consistent nodal forces, as shown for one of the strips in Figure 4.8, match the exact solution and no mesh dependency is observed.

As a third test, we verify the behavior of the contact scheme for a totally unstructured discretization. The setup of the test consists of a shell supported on top of the other one. The bottom shell is fixed and the in-plane movement of the top shell is

(a)   (b)

(c)
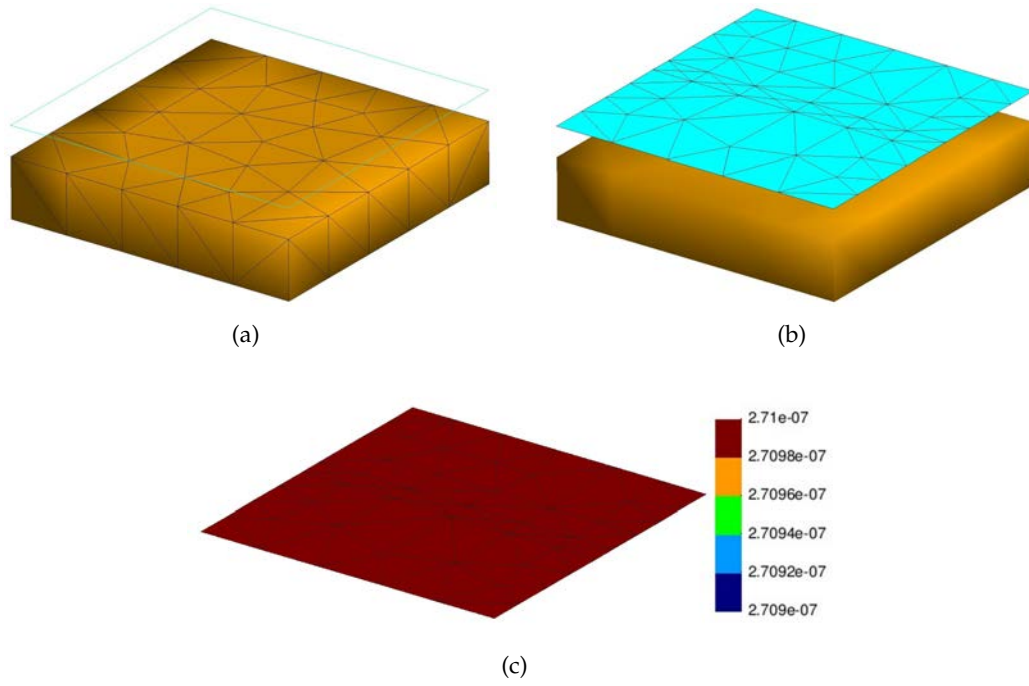
Figure 4.9: The discretization of a) bottom shell and b) top shell with the obtained displacement field (c) for the top shell under the constant load.
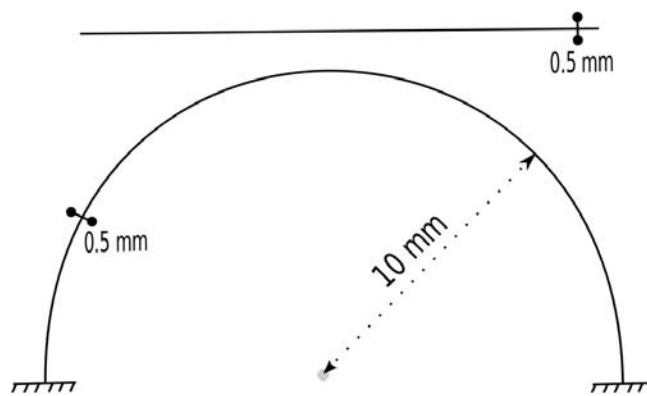
Figure 4.10: Hemispherical shell and plate,front view. The contact is triggered by the vertical movement of the plate.
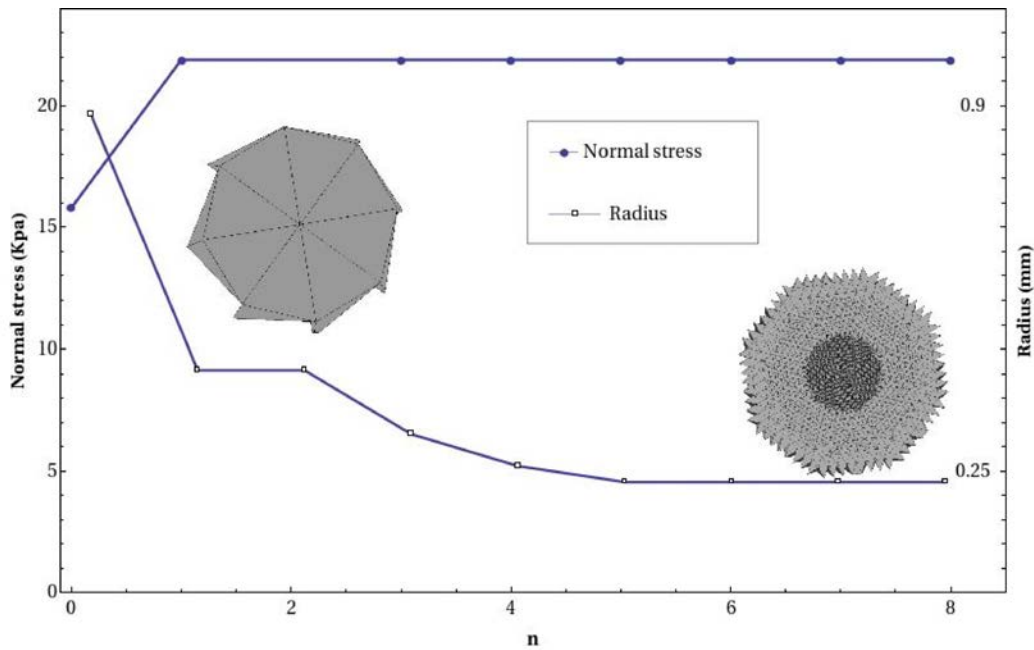
Figure 4.11: Normal stress at the apex and the radius of the contact zone versus the, n, number of refinement levels. A top view of the *active* contact elements related to the refinements n = 1 and n = 8 are shown.

constrained along the edges. The unstructured discretization of both shells are shown in Figures 4.9a and 4.9b.

The top plate is loaded with a distributed pressure of 1000 N/m^2 and the top shell is only supported by the action of the contact forces. Given the irregular distribution of the nodes it is not trivial to compute the exact contact forces for comparison purposes. Instead of referring to the values of the contact forces we therefore analyise the deformation field obtained, and verify, as shown in Figure 4.9c, that as expected no bending deformation nor rotation of the top flexible shell is found.

This allows us to conclude that the propsoed contact strategy correctly passes the contact patch test using an arbitrary discretization of the contacting shells.

4.6.2 *An example on mesh refinement*

The effect of mesh refinement on the computation of the peak contact forces and the distribution of the contact elements are studied in this example. The test consists of a disk and a hemispherical shell as shown in Figure 4.10. The sphere has a radius of 10.0 *mm* and a thickness of 0.5 *mm*. The same thickness is chosen for the disk. Elastic behavior is considered with the Young modulus of E = 200 *GPa* and zero Poisson's ratio. The disk and the sphere are initially in touch.

In order to trigger the contact, the top disk goes down under constant vertical displacement equal to 2% of its thickness. This provides some contacts at the apex of the sphere and yields a negligible displacement field in the shell.

Contact, as expected, is centered at the apex of the sphere where the maximum normal stress is created. The evolution of the contact zone radius and the maximum normal stress versus the level of refinement are depicted in Figure 4.11. The number
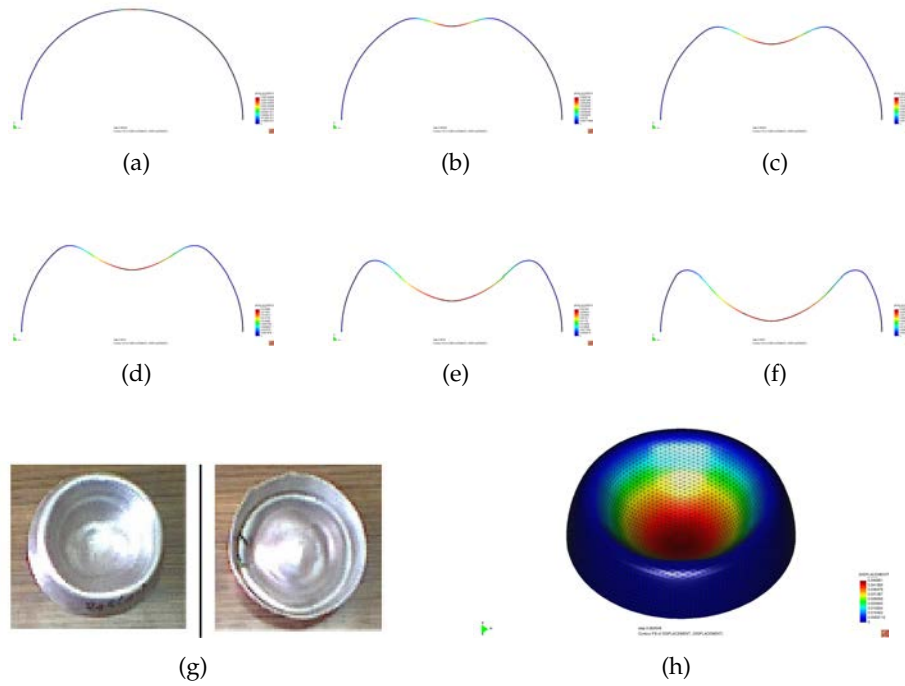
Figure 4.12: Collapse of spherical shell compressed *a* to *f* Mid-plane evolution, g) H4 specimen [39] h) final configuration

of active contact elements increases as a finer mesh is used in the contact zone. Eight levels of refinement are considered that result in a variation in number of active contact elements from 16 to 21000. It is observed that the maximum stress reaches its asymptotic value after two refinements while further refinement is necessary for the radius of the contact zone to obtain its minimum.
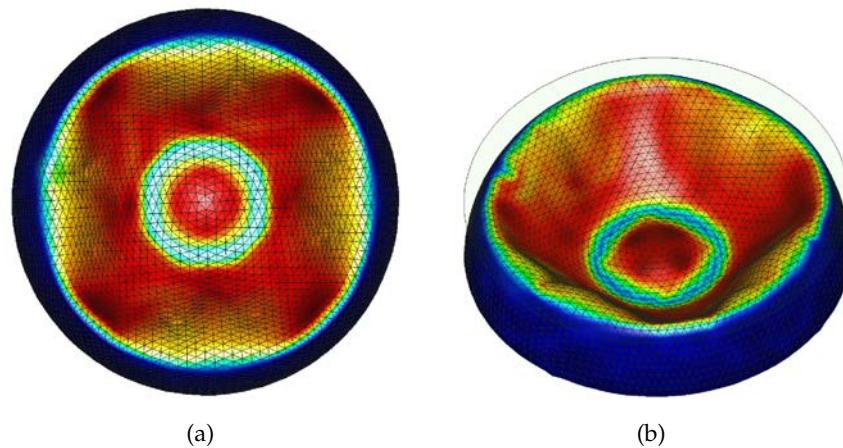
Figure 4.13: Collapse of compressed spherical shell. Appearance of lobes

4.6.3 *Collapse of a compressed spherical shell*

In this section the large deformation of an elasto-plastic hemispherical shell compressed between two rigid plates is studied. An aluminum hemisphere of radius 44 *mm* and thickness of 1.6 *mm* with yield stress of 36 *GPa* and Young modulus of 70 *GPa* is compressed.

Updike [130] proposed an expression relating the compression force and deformation of the spherical shell which is valid for deformations up to one tenth of the shell radius. Gupta et al [39] provided a complete set of experimental data for hemispherical and shallow aluminum shells. The factor that affects the behavior of these spherical shells is the radius to thickness ratio.

The analysis was carried out with a mesh of 3750 EBST elements. The computational results suggest that for small ratios (R/t less than 53) two stages of deformation can be distinguished. The first one is an elastic deformation, wherein a local flattening of the shell in contact with the plate takes place and the second one is the formation of an axi-symmetric inward dimple.

Figure 4.12 shows the evolution of the inward dimple through a mid-plane cut. The geometry used is the same as for the H4 specimen used in [39]. The radius of the parallel circle for an axial compression amount of 16.4 *mm* was computed. Experimental measurements reported a radius of 38.8 *mm*. The numerical prediction provides a radius of 33.8 *mm* that is in good agreement with the experiment. Also note that the radius of the parallel circle analytically calculated for a perfect hemisphere and due to the mentioned compression is 34.3 *mm*, which is similar to our result.

As the R/t ratio increases, the third stage of the collapse appears yielding a non-symmetric shape due to the buckling that is manifested in the appearance of the lobes. The number of lobes varies as R/t changes.

Figure 4.13 shows the top view of the hemispherical shell for R/t = 68.3, at the third stage of the collapse where the lobes appear. This model has the same property as the A10 specimen in Gupta et al [39] but with a constant thickness of 1.11 *mm* along the meridian. A mean experimental collapse load of 5.72 *KN* was reported for this specimen. In our simulation the mean collapse load is 5.95 *KN* which is in good agreement with the experimental value and matches the theoretical value of 5.94 *KN* calculated in the same reference.

We remark that two sets of contact elements appear in this example. At the two first stages of collapse, that lead to the formation of the inward dimple, contact only occurs between the top plate and the cap. The *potential* contact elements related to these stages can be seen in Figure 4.2*a*. The active contact elements are shown in Figures 4.2*b* and 4.14*a*. As the experiment evolves and the inward dimple approaches the bottom plate, the second set of contact elements appear. These elements can be seen in Figure 4.14*b*. This is a contact between the cap and the bottom plate and is also automatically detected by the distance criteria explained in Section 4.3. Note that two sets of *potential* contact elements are engaged to detect the contacts in this example. One set discretizes the volume between the plate and the cap and the other set discretizes the volume between the bottom plate and the cap. It is necessary to distinguish between these two sets of elements to be able to detect the *free corner* in each contact element. As mentioned in Section 4.3 each *potential* contact element has at least a *free corner* that has no neighbor assigned to it and is detected by the

(a)

(b)
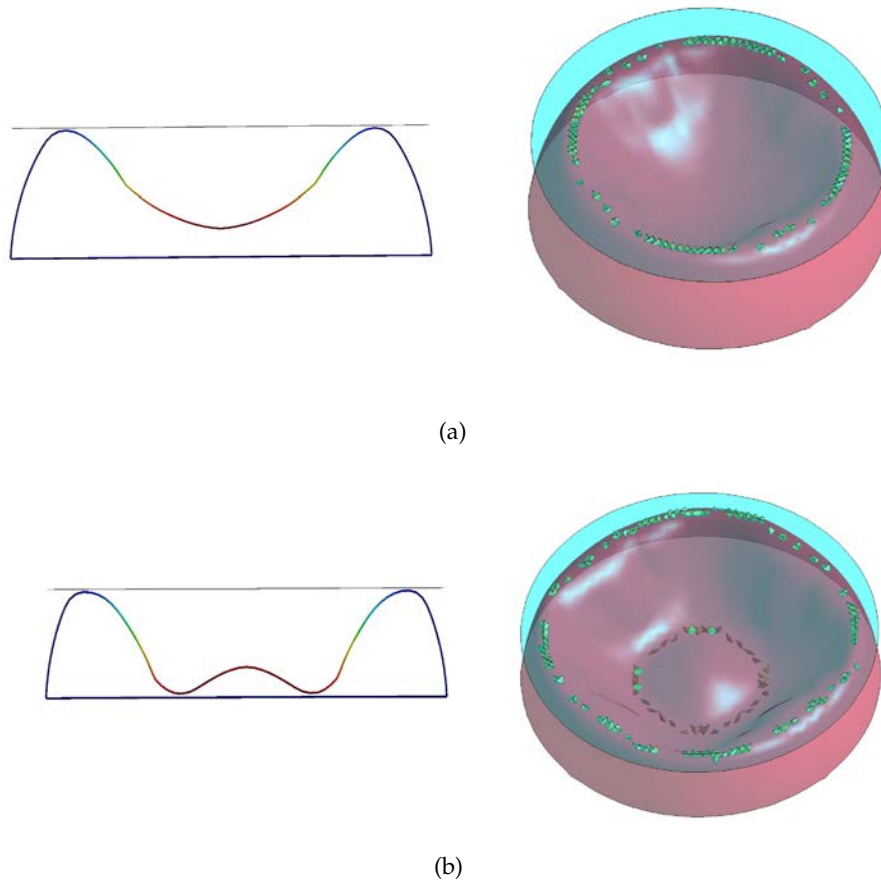
Figure 4.14: Collapse of compressed spherical shell. Midplane, 3D view and *active contact elements* at two instants

neighboring information. If no distinction is made between the two volume elements described above then we come up with elements that have no *free corner*.

To overcome this problem, the region marker introduced in Section 4.3.3 is used. In this way for each element the neighbor search is done among the elements that have the same region flag as the chosen element and so we are able to detect the *free corner*s. Note that meshing is constrained and always respects the interface, so regions are completely separated and each element has exactly one region marker.

4.6.4 *Contact-impact between two tubes*

The elasto-plastic contact between two tubes is studied. The numerical setup is described in Cardoso et al, [15].

Both tubes have a radius R = 0.1 *m*, length L = 0.46 *m* and thickness t = 0.005 *m*. The stiffer tube has a Young's modulus E = 200 *GPa* while the softer one has E = 70 *GPa*. Both tubes have density ρ = 7840 *kgm^{-3}*, Poisson's ratio ν = 0.3 and a yield stress σ_y = 200 *Mpa*. The initial velocities of each of the tubes are (0,30,80) *ms^{-1}* and (0,0,-80) *ms^{-1}*, respectively so that a large relative impact and sliding velocity is obtained.
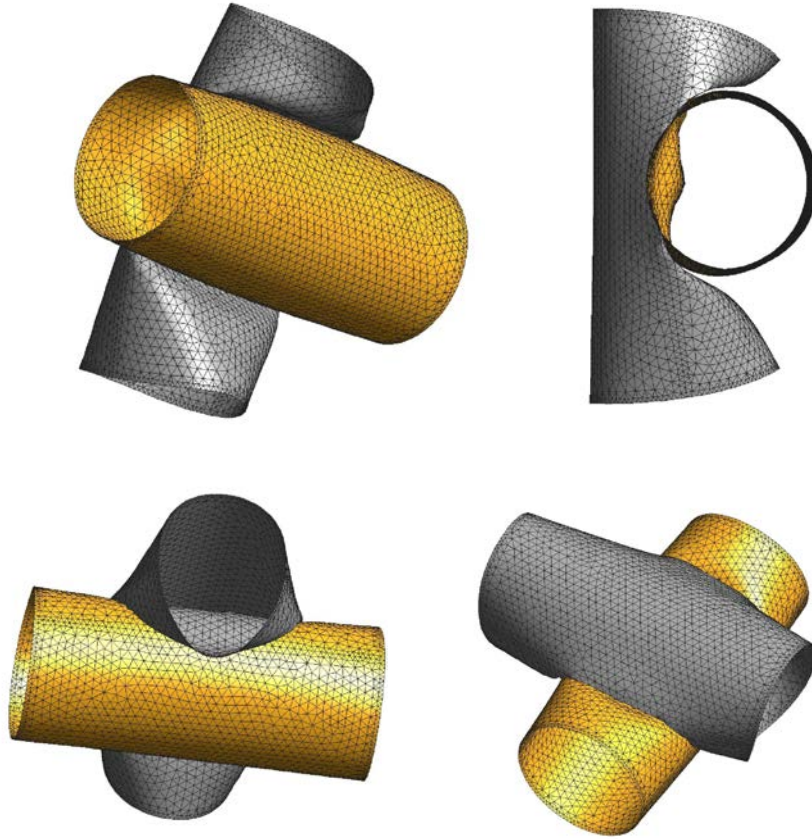
Figure 4.15: Contact-impact of two tubes. Geometries at time t = 1ms

7000 EBST elements were used for discretizing each tube. Figure 4.15 shows the deformed geometry after the impact. A similar set of results obtained by Cardoso et al. [15]. This example clearly shows the behavior of the shell for large deformations and severe contact conditions. Note that the surface meshes are unstructured and no restriction is imposed on them. As in the previous example, different regions are considered to detect the contact elements. Tubes are made closed by putting top and bottom caps and both of them are place in a closed box. Consequently three regions appear, one in each tube to mark elements for the self-contacts and one inter-tube region to mark the contact between tubes.

4.6.5 *Ball impacting a clamped plate*

In this example we study a ball impacting a clamped rectangular plate. The data for this test was provided by Zhong [139]. Both the ball and the plate are assumed to be elastic with Young's modulus E = 200 GPa and Poisson's ratio ν = 0.3. The ball has a radius R = 0.1 m and the beam has a length L = 1.0 m, width W = 0.24 m and thickness t = 0.0015 m. An initial velocity of (0,0,-30.0) ms^{-1} is assigned to the ball. Figure 4.16 shows the results obtained by our method using a mesh of 4800 EBST elements and those obtained by Cardoso et al [15]. Good agreement is again obtained between both set of results.

(a)	(b)
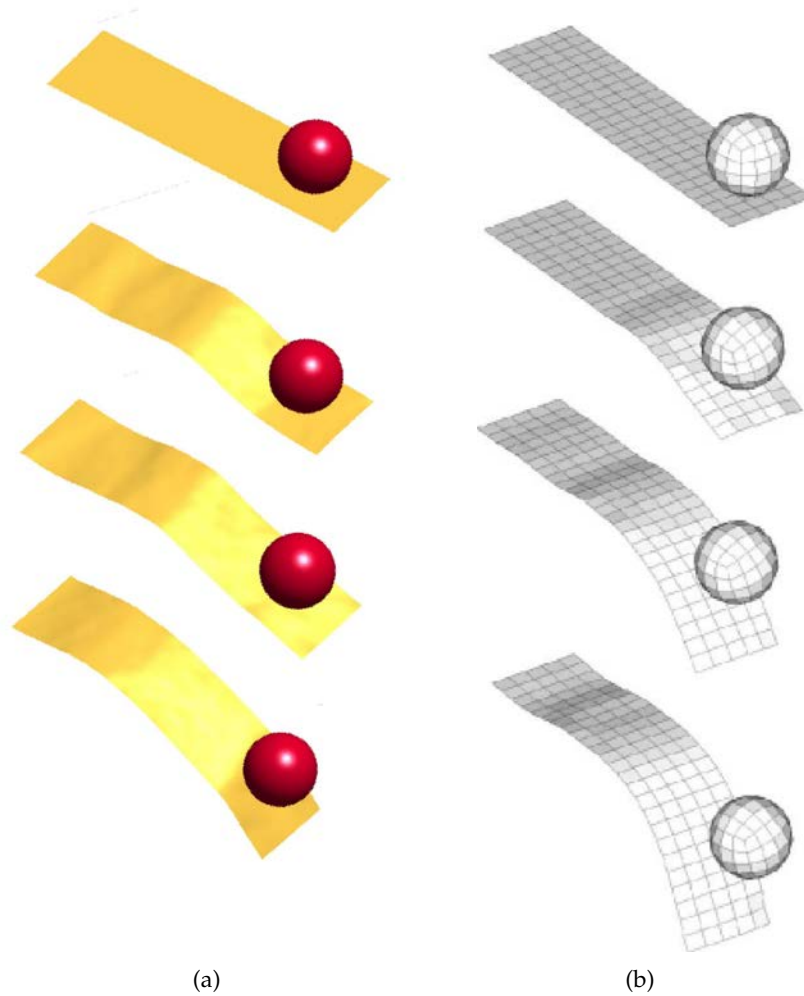
Figure 4.16: Ball impacting a clamped plate a) our method b) Cardoso et al. [15]

4.6.6 *Buckling of cylindrical tube*

The behavior of cylindrical tubes under external pressure is of interest in applications like crash worthiness in car industry and implosion of air filled containers. The presented formulation was originally developed to deal with underwater implosion problems [115].

In this example, the buckling of a cylindrical tube under constant external pressure is studied. The tube has a length, $L = 5.63$ *in*, a mid-plane radius, $R = 0.7497$ *in*, a thickness, $h = 0.0276$ *in* and has supports along 1 *in* on both ends. An elasto-plastic material made with $\sigma_y = 4.008 \times 10^4$ *psi* and $E = 1.008 \times 10^7$ *psi* is considered. The cylinder is subjected to an external pressure of $p = 443.43$ *psi*.

Second and third buckling modes are considered. In order to excite the second mode, the nodes of the tube section are perturbed by an imperfection of the form $\cos(2\theta)$ and with an initial amplitude equal to the 5% of the initial thickness. The third mode is obtained by an imperfection of the form $\cos(3\theta)$ and with the same amplitude as the second mode.

Figure 4.17 shows the evolution of the two longitudinal and transversal mid-planes during the collapse for the second mode. The self-contact between two sides of the cylinder happens at a high velocity around 50 *m/s* and rapidly propagates along the cylinder, in both directions and toward the two ends. Except for a small rebound that appears after the first contact, the velocity of the collapsed walls reduces to zero immediately.

The initial geometry of this example already provides a closed volume with one region and no artificial box is necessary. Figure 4.19 shows experimental results reported
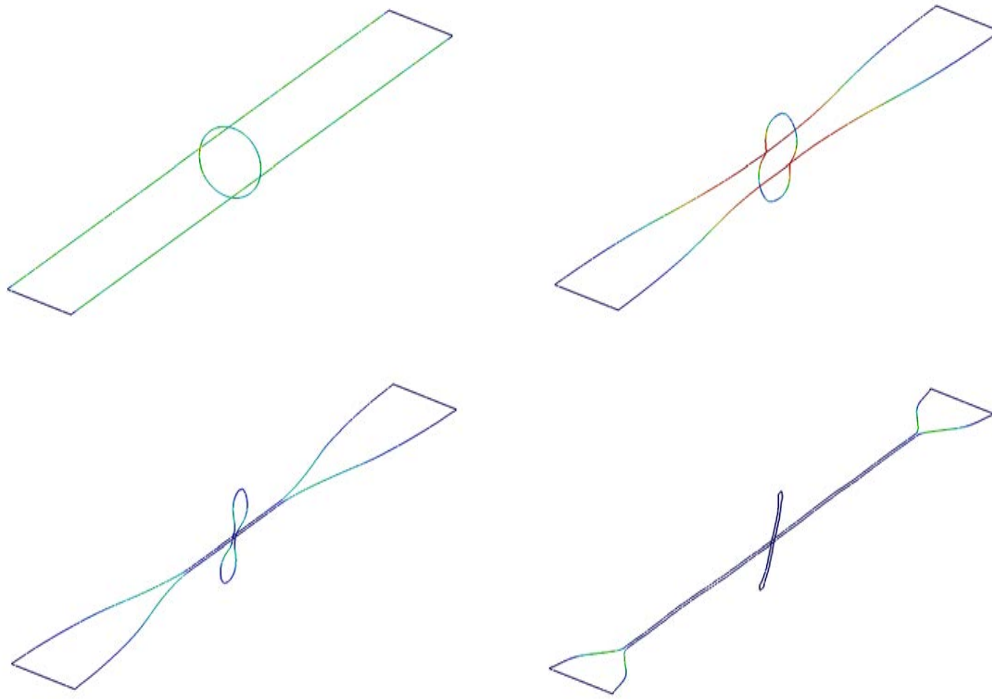
Figure 4.17: Buckling of cylindrical tube under external pressure. Mid-plane view for the second mode collapse

in [3] for the collapse in the third buckling mode.

Figure 4.18 shows the final configuration of the tube. As no failure criterion is included the ruptures appearing in the experiment are not reproduced in our numerical results but the final shape is in good agreement with the experiment. The detection of the first *active contact* elements along the tube is shown in Figure 4.18. It can be seen that the distribution of the active contact elements is not exactly symmetric, due to the unstructured mesh of 12000 EBST elements used for discretizing the tube.

4.7   CONCLUSIONS

We have developed an algorithm for solving shell contact problems. The space between the shell mid-planes is defined as the *potential contact domain*. A constrained discretization of this domain into 4-noded tetrahedra, that respects surface mesh connectivities, is performed.

(a)

(b)
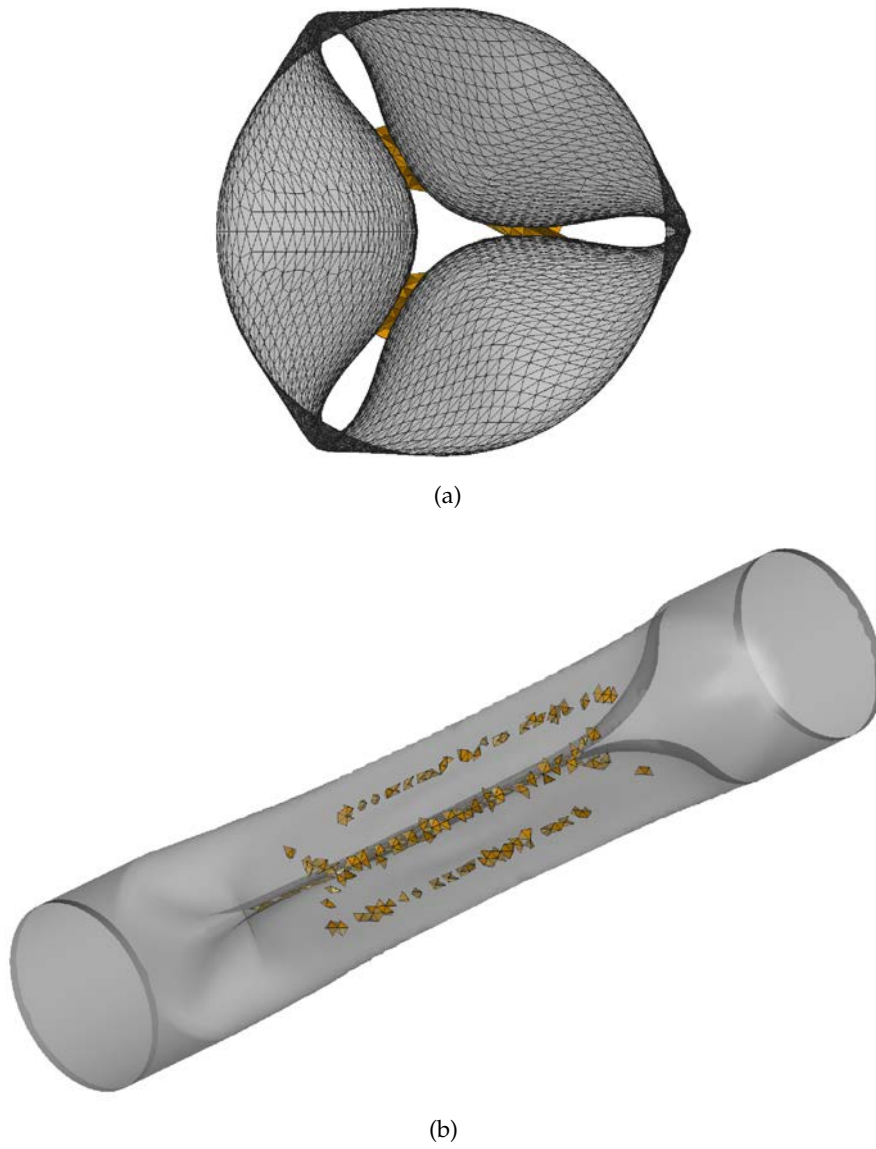
Figure 4.18: Third mode buckling of cylindrical tube. *Active* contact elements a) mid-plane view b) 3D view

Figure 4.19: Experimental results for third buckling mode [3]

A characteristic distance is calculated for each potential contact element and is compared to the mean value of the interacting shells' thicknesses. The so-called *active*

contact domain consist of those elements that satisfy this contact criteria. We construct a Green strain field by means of element normals in each active contact element and then calculate elastic contact forces. As the contact elements share all nodes with shell surface meshes, these forces are directly assembled to the shell nodes. This contact algorithm has been tested for various self-contact and multi-body contact problems in shells using the rotation-free EBST shell triangle. The algorithm can be easily integrated in coupled problems involving shells, solids and fluids. Unlike penalty methods, no arbitrary contact factor to enforce the contact conditions is required and regularity is not needed for the meshes discretizing the shell surface. Very good results have been obtained in the application of the new contact algorithm to different shell-contact problems.

FLUID-STRUCTURE INTERACTION

We propose a fully Lagrangian monolithic framework to simulate the underwater implosion of closed containers "a la PFEM" [59, 92]. To our knowledge, it is the only fully Lagrangian *compressible* FSI framework available. The main features of this framework are the monolithic coupling of the fluid and structure subsystems, the discontinuous treatment of the pressure and density at the interface and the possibility of providing the desired mesh resolution when large displacements occur. This framework is an extension of the multi-fluid compressible formulation, presented in chapter 3, to FSI problems.

We first recall the stabilized variational multiscale method developed in chapter3 for solving the Euler hydrodynamic set of equations. Then the coupling of the EBST shell element and the contact algorithm presented in previous section is explained. The implicit and explicit time integration schemes for the coupled system are detailed and the matrices of the coupled system are extracted. A Section is devoted to explain the Lagrangian framework that includes the adaptive constrained mesh generation, and the construction and solution of the coupled system. Finally the underwater implosion of an aluminum cylinder is simulated and compared with the experimental results.

The material of this chapter are taken from our paper, *A compressible Lagrangian framework for modeling the fluid-structure interaction in the underwater implosion of an aluminum cylinder* [115].

5.1 INTRODUCTION

The goal of the present work is to accurately predict the underwater implosion of an aluminum cylinder. An implodable volume, by definition, is any pressure housing containing a non-compensated compressible volume at a pressure below the external pressure which has the potential to collapse [74].

From the pioneer studies of Rayleigh [102] on the dynamics of bubble and cavitation to the latest works on the violent collapse of μm size bubbles excited by the sound waves [48, 77], different aspects of the underwater implosion have been investigated.

The main signature of this phenomenon is a low flat negative-pulse that is followed by a sharp positive-pressure spike. The strength and duration of the pressure peak depend on the dimension of the implodable volume and the depth in which the implosion occurs[94, 75]. Although, the 1D theoretical studies predict an oscillating behavior of the bubble, with the same amplitude and strength, the compressibility of the high pressure surrounding water [99, 101] and the appearance of the instabilities [7, 77, 9] on the air-water interface explain the strongly damped sinusoidal pulse

detected in the experiments. In many of such experiments [94, 129, 43] the implodable volume is simply a light bulb preweakend in some zones or being attached to a crack initiator device.

In practice, the acoustic wave emanating from these glass spheres can be used to detect the contact of the equipment with the seabed. On the other hand, there is concern that under the wrong circumstances, the pressure pulses produced by the collapsing volume, which in this case are metallic containers filled with fluid at atmospheric-pressure, can damage nearby submersibles or other objects [21, 78].

Although the first predictions on the dynamics of the implosion can be done using 1D models and neglecting the surrounding structure, a full 3D model that considers the realistic, fast dynamic, fluid-structure interaction (FSI) of the problem seems inevitable. It is also necessary to model the structure that separates air and water. Not only the physics of the problem changes by considering a separating structure at the air-water interface, obviously no Rayleigh-Taylor interfacial instabilities appear, but the errors in the pressure peak value neglecting this structure can reach 44% [129] of its maximum value.

The major challenges during the underwater implosion process are: fast dynamics of the FSI, all the process occurs in less than 1 ms; resolution of the possible shock waves that appear in both air and water, and, last but not least, the large deformations of the structure that in some cases end up with cracks and self-contact in the shell structure.

As high pressures are involved, the external fluid (water) as much as the internal one (air) are modeled as compressible media. Respecting the structural part, the geometric and material nonlinearities of the shell structure need to be considered to obtain a realistic solution.

Various studies considering the FSI in related applications are performed. Among them, Kalumuk [16] studied bubble interactions with nearby bodies using the boundary element technique. Some authors [141, 70] investigated the interaction of a bubble, caused by an underwater implosion, with free-surface structures. Iakovlev[54] investigated the interaction of an external explosion with a deformable inner structure. Cor et al [21] evaluated the effect of internal structure on the behavior of spherical and cylindrical implodable volumes.

Among the relatively few works that fully model the FSI system is the one proposed by Farhat et al [31, 32]. They designed a three-field formulation for the non-linear fluid-structure problem based on the Arbitrary Lagrangian Eulerian (ALE) formulation of the fluid equations. Furthermore, a second-order loosely coupled staggered scheme is designed to treat the FSI and few elements have been used for discretizing the internal air due to the restrictions of the ALE mesh motion algorithms.

In the following we recall the stabilized hydrodynamic set of equations presented in chapter 3. The main difference comparing the presenetd two-fluid system isthe presence of a shell structure that separates the internal air from the external water. This shell is modeled with the three node rotation-free EBST shell element [35].

Linear tetrahedra are used to discretize the air and water domain and both fluids are modeled as compressible continua. A nodally perfect matched definition of the interface, proposed by Idelsohn et al [57], allows us to duplicate the pressure and density at the interface level. The contact method described in chapter **??** is used to detect the contact and compute the non-penetrating forces. As large deformations

occur during the solution, a constrained adaptive mesh is generated, whenever necessary, to ensure the quality of the mesh. The monolithic FSI system is solved using an implicit predictor/multi-corrector Bossak scheme at each step. An explicit forward Euler solution of this system is also provided and both results are then compared with experimental data.

5.2 GOVERNING EQUATIONS

5.2.1 *Lagrangian hydrodynamic equations*

We recall from chapter 3 that the Lagrangian compressible hydrodynamic governing the conservation of mass, momentum and energy are, respectively,

$$\rho J = \rho_0 \tag{5.1a}$$

$$\rho \dot{\mathbf{u}} + \nabla_x p = \mathbf{b} \quad \text{in } \Omega, \ t \in]0, T[\tag{5.1b}$$

$$\rho \dot{\epsilon} + p \nabla_x \cdot \mathbf{u} = \nabla_x \cdot \mathbf{h} + \rho r \quad \text{in } \Omega, \ t \in]0, T[\tag{5.1c}$$

We then complete this set of equations by an equation of state of the form $p = \hat{p}(\rho, \epsilon)$. Applying the multisclae paradigm with the decomposition of the unknowns as,

$$\mathbf{u} = \mathbf{u}^h + \mathbf{u}'$$
$$p = p^h + p' \tag{5.2}$$
$$\epsilon = \epsilon^h + \epsilon'.$$

and considering some simplifications typical of the multiscale method, we end up with the stabilized form of the Eqs. (5.1), i.e.:

$$\int_\Omega \mathbf{v}^h \cdot \rho\,(\dot{\mathbf{u}}^h)\,d\Omega - \int_\Omega (\nabla_x \cdot \mathbf{v}^h)\,p^h\,d\Omega$$
$$+ \int_\Omega \nabla_x \cdot \mathbf{v}^h\,\tau\,(\dot{p} + \rho c_s^2 \nabla_x \cdot \mathbf{u})\,d\Omega = 0 \tag{5.3}$$

$$\int_\Omega q^h\,(\rho \dot{\epsilon}^h + p^h\,\nabla_x \cdot \mathbf{u}^h)\,d\Omega$$
$$+ \int_\Omega \tau(c_s^2)\nabla_x q^h \cdot (\rho \dot{\mathbf{u}}^h + \nabla_x p^h)\,d\Omega \tag{5.4}$$
$$- \int_\Omega q^h\,\nabla_x \cdot \mathbf{u}^h\,\tau\,(\dot{p} + \rho c_s^2 \nabla_x \cdot \mathbf{u})\,d\Omega = 0$$

These equations are best suited for the mid-point explicit time descritization as presented in chapter 3, while a more suitbe form for the implicit scheme can be obtained by introdcing a full $\mathbf{u} - p$ equivalence of this stabilized form. We have already shown in chapter 3 that considering the Mie-Grüneisen equation of state (EOS) that has the following general form:

$$p = \hat{p}(\rho, \epsilon) = f_1(\rho) + f_2(\rho)\epsilon. \tag{5.5}$$

and by applying Gibbs identity, an equivalent for the energy equation can be obtained as,

$$\rho^h \dot{\epsilon}^h + p^h \, \nabla_x \cdot \mathbf{u}^h = \rho \frac{\partial \epsilon}{\partial p}\bigg|_\rho (\dot{p} + \rho c_s^2 \nabla_x \cdot \mathbf{u}), \tag{5.6}$$

In this way, and by applying equation (5.6) to the stabilzied form of the enery equation (5.8), the $\mathbf{u} - p$ stabilized form can be obtained as,

$$\int_\Omega \mathbf{v}^h \cdot \rho \, (\dot{\mathbf{u}}^h) \, d\Omega - \int_\Omega (\nabla_x \cdot \mathbf{v}^h) \, p^h \, d\Omega$$
$$+ \int_\Omega \nabla_x \cdot \mathbf{v}^h \, \tau \, (\dot{p} + \rho c_s^2 \nabla_x \cdot \mathbf{u}) \, d\Omega = 0 \tag{5.7}$$

$$\int_\Omega \rho^h \frac{\partial \epsilon}{\partial p}\bigg|_\rho (q^h \, (\dot{p} + \rho c_s^2 \nabla_x \cdot \mathbf{u})) \, d\Omega$$
$$+ \int_\Omega \rho^h \frac{\partial \epsilon}{\partial p}\bigg|_\rho (\tau(c_s^2) \nabla_x q^h \cdot (\rho \dot{\mathbf{u}}^h + \nabla_x p^h)) \, d\Omega \tag{5.8}$$
$$- \int_\Omega q^h \, \nabla_x \cdot \mathbf{u}^h \, \tau \, (\dot{p} + \rho c_s^2 \nabla_x \cdot \mathbf{u}) \, d\Omega = 0$$

We remind that for an ideal gas the term $\rho^h \frac{\partial \epsilon}{\partial p}\big|_\rho$ is constant and equal to $1/(\gamma - 1)$.

Eqs. (5.7) and (5.8) are used in Section 5.3.1 for obtaining the matrices of the implicit monolithic scheme. We remind that at the presence of the shock waves, shock-capturing operators in the form of artificial viscosities are introduced to smear the discontinuity over a few cells of the computational grid.

In the following, the variational model used for the structure is briefly presented.

5.2.2   Rotation-free shell triangle

A rotation-free shell triangular element is used to model the behavior of the cylinder under the high external water pressure. The Enhanced Basic Shell Triangle (EBST), is derived using an assumed linear field for the membrane strains and an assumed constant curvature field [35, 34]. Both assumed fields are obtained from a quadratic interpolation of the displacement field of a patch. For each element the patch is defined as the element itself and three neighboring elements, as shown in Figure 5.1.

The virtual work principle is written as,

$$\int \left[\delta\boldsymbol{\epsilon}_m^T \boldsymbol{\sigma}_m + \delta\boldsymbol{\kappa}^T \boldsymbol{\sigma}_b \right] \, dA = \int \delta\mathbf{y}^T \mathbf{t} \, dA \tag{5.9}$$

Where $\delta\boldsymbol{\epsilon}_m$ is the virtual Green-Lagrange membrane strain vector, $\delta\boldsymbol{\kappa}$ is the virtual curvatures vector and $\delta\mathbf{y}$ is the virtual displacement vector. $\boldsymbol{\sigma}_m$ and $\boldsymbol{\sigma}_b$ are the resultant membrane and bending stresses computed from the integration of the second Piola-Kirchhoff stresses along the shell thickness. A detailed descriptions of the element matrices can be found in [35, 34]. The original EBST formulation was improved [34, 89] by introducing a non-local quadratic function constructed over the whole patch which is used for computing the curvatures and the membrane strains at the mid-side points of the central element. Such improved kinematics allows the
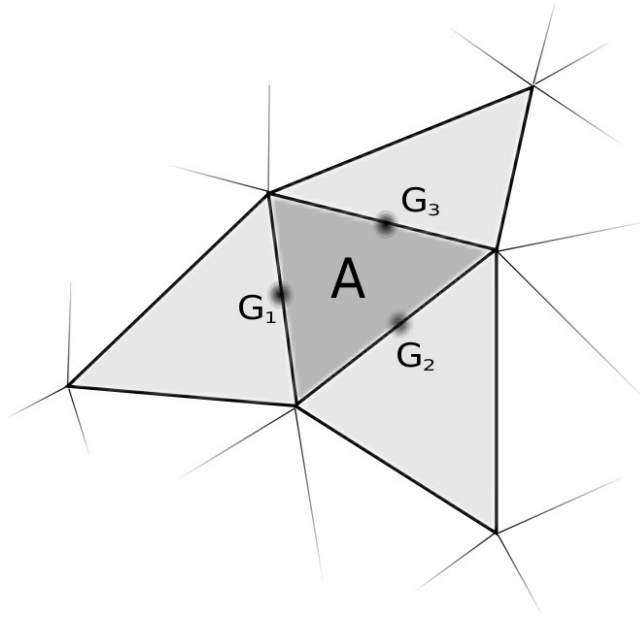
Figure 5.1: EBST rotation-free shell triangle "A" and element patch used to compute the curvatures and membrane strains at points G_1, G_2, G_3

natural definition of a volume around the mid-plane, which in turn can be used effectively for the integration of the stresses across the thickness, thus allowing the correct representation of non-linear material models.

In summary, main characteristics of the enhanced rotation-free EBST element are:

1. Quadratic interpolation of the geometry of the patch using the positions of the six nodes of it

2. The membrane strains are assumed to vary *linearly* within the central triangle and are expressed in terms of the deformation gradient at the mid-side points of the triangle G_i ($i = 1, 2, 3$ see Figure 5.1).

3. The assumed *constant curvature* whithin the element is calculated from the direct evaluation of the deformation gradient at the mid-side points.

The absence of rotations also allows us using standard 3D strain measures, thus effectively avoiding problems related to arbitrarily large rotations which may appear during the computations. We may observe that since the element curvature and the membrane strains are calculated by taking into account overlapping subdivisions, this does not fit in the standard definition of a "finite element".

The last ingredient of the FSI algorithm is a contact scheme that allows the self-contact between shells as presented in chapter **??**. To consistently develop our monolithic framework we briefly recall it in the following section.

5.2.3 *Contact model*

The key concept in this contact method is to descritize the contact domain by constructing a finite element mesh which describes the potential contact area.

Figure 5.2 depicts two shell surfaces and the potential contact area between them discretized by a finite element mesh. As we model the mid-planes of the shells, a critical distance, l, is defined as a function of the shells half-thicknesses as,

$$l = (t_1 + t_2)/2 \tag{5.10}$$

For each element of the potential contact domain a distance h is computed, representing the distance between the shells in contact (Figure 5.2). The contact criterion,

$$h \leqslant l$$

is then checked for each element and those elements that satisfy this criteria build the active contact domain (element "A" in Figure 5.2).

Having known the active contact elements, a strain field of the type,

$$\boldsymbol{\epsilon} = \mathbf{n} \otimes \mathbf{n}\, \epsilon \tag{5.11}$$

is defined in each of these elements. Here $\mathbf{n}$ is the normal direction defined in each element and ϵ is the 1D Green-Lagrange strain defined in that direction, namely:

$$\epsilon := (l^2 - h^2)/l^2. \tag{5.12}$$

We assume a small deformation frictionless contact. The contact algorithm is designed to handle arbitrary deformations of the shells involved, nevertheless we assume that the variation of the thickness induced by the contact forces can be considered "small" although not necessarily infinitesimal.

The stress tensor inside each active element is then computed as,

$$\boldsymbol{\sigma} = \mathbf{D} : \boldsymbol{\epsilon} \tag{5.13}$$

where $\mathbf{D}$ is the fourth order elastic constitutive tensor for the shell material.

Note that in this contact scheme the strain field is computed directly from the displacement of the shell. As the nodes of the contact elements coincide with those of the shell, the contact forces are directly assembled on the nodes of the shell.
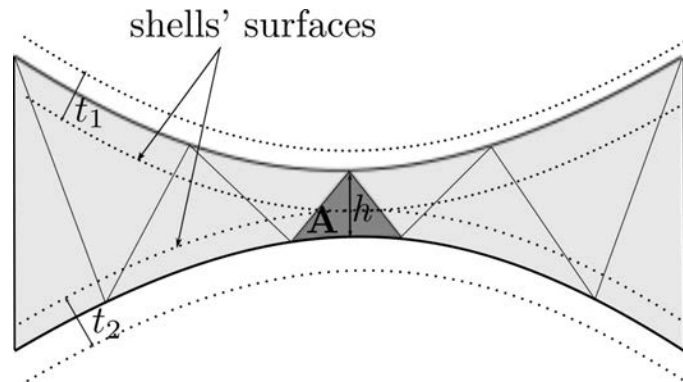
Figure 5.2: Shell thicknesses t_1 and t_2 and actual distance between mid-planes, h. Light gray zone is the *potential* contact domain discretized by triangular elements. Element "A" in dark gray is an *active* element that satisfies the contact criteria.

Details on how to compute distance, h, and normal, **n**, in each potential contact element in 2D and 3D cases can be found in chapter **??** and in reference [67].

We note that a contact algorithm for FSI problems was also introduced in the context of space-time formulation of incompressible flows in [120, 124, 107], with an improved, conservative-force version introduced in [119].

In the next section, the matrices involved in the FSI monolithic system are obtained through the time discretization of the variational forms presented here.

5.3   TIME DISCRETIZATION

The solution of highly transient FSI problems can be achieved by a variety of methods. It is often accepted that the use of explicit solution schemes for the fluid and of implicit techniques for the structure leads to efficient coupling strategies [105].

In dealing with incompressible or quasi-incompressible problems the added-mass effect becomes important, which generally favors the use of strongly coupled schemes, based on monolithic [106] techniques or slight modifications of the fluid equations [60], or "direct" and "quasi-direct" coupling techniques [125], which have been formulated for non-matching fluid and structure discretization at the interface but reduce to monolithic coupling when the discretizations are matching.

Staggered schemes appear to be more and more favored as the compressibility of the fluid increases and as the time step diminishes. For the problem at hand, given the compressibility of both the air and of the water, loosely coupled schemes are possible and were used effectively for example in [32] for the solution of a very similar problem.

Given the features of the FE formulation presented here we prefer to go for a monolithic coupling scheme (that is, the solution scheme chosen tightly couples the fluid and structural unknowns) which we then discretize in time using two different approaches, one implicit and the other explicit. As we shall comment later, the implicit approach turns out to be favored in the initial phase of the collapse, while the explicit scheme appears to be convenient in the final phase.

Before proceeding the time discretization strategies chosen, we would like to highlight some aspects of the coupling scheme.

Figure 5.3 depicts a 2D view of the FSI monolithic system chosen. Two fluids, representing compressible air and water are separated by a shell structure. The structure does not cut the fluid elements but represents a nodally perfect matched interface [57]. Velocity is continuous across the interface, while pressure and density are discontinuous at the interface level. Such discontinuity is represented in the FE solution by a discontinuous pressure field.

In other words, each fluid works with its own pressure and density DOFs. It implies that interface nodes, that are common between the fluids and the shell structure, have duplicated kinematic variables i.e. pressure and density.

5.3.1   *Implicit time discretization*

A residual based predictor/multi-corrector scheme is adopted to best handle the nonlinearities involved in fluid, structure and their interaction. To this end, a second-order Bossak scheme is used for discretization in time of both fluid and structure. This sec-
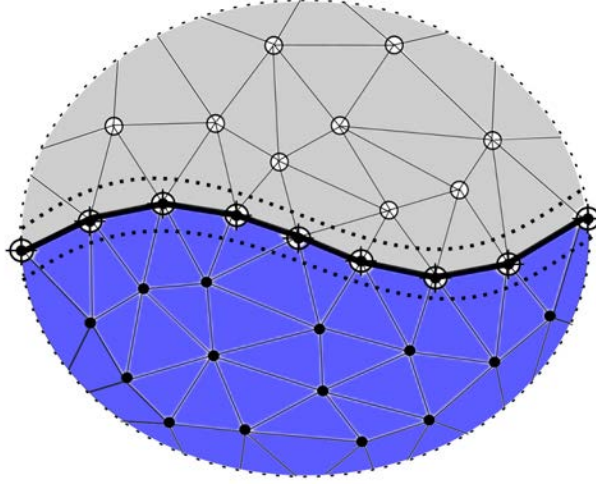
"•" *First Fluid* "○" *Second fluid* "+" *Structure*

Figure 5.3: Two fluids that are separated by the shell structure. Interface nodes are common between fluids and structure and have duplicated pressure and density.

tion is devoted to systematically develop the involving matrices and providing the multi-corrector FSI scheme considering the implicit time discretization.

5.3.1.1 *Fluid equations*

Let us rewrite the momentum and energy equations, (5.7) and (5.8) as,

$$
\int_\Omega \mathbf{v}^h \cdot \rho\,(\dot{\mathbf{u}}^h)\,d\Omega - \int_\Omega (\nabla_x \cdot \mathbf{v}^h)\,p^h\,d\Omega
$$
$$
+ \int_\Omega \nabla_x \cdot \mathbf{v}^h\,\tau\,(\dot{p} + \rho c_s^2 \nabla_x \cdot \mathbf{u})\,d\Omega = 0 \tag{5.14}
$$

$$
\int_\Omega q^h\,\dot{p}^h\,d\Omega + \int_\Omega \rho c_s^2\,q^h\,\nabla_x \cdot \mathbf{u}\,d\Omega
$$
$$
+ \int_\Omega (\tau(c_s^2)\nabla_x q^h \cdot (\rho\dot{\mathbf{u}}^h + \nabla_x p^h))\,d\Omega \tag{5.15}
$$
$$
- \int_\Omega \Gamma\,q^h\,\nabla_x \cdot \mathbf{u}^h\,\tau\,(\dot{p} + \rho c_s^2 \nabla_x \cdot \mathbf{u})\,d\Omega = 0
$$

Note that Eq. (5.8) is multiplied by Γ, the inverse of $\rho^h \frac{\partial \epsilon}{\partial p}\big|_\rho$, known as the Grüneisen parameter [76, 109]. This thermodynamic parameter varies only mildly with the thermodynamic state of a fluid system, unless phase transitions occur [76].

Considering a continuous linear approximation for the velocity, pressure and density, the variational forms (5.14) and (5.15) can be written in matrix form as,

$$
\mathbf{M}_{\mathcal{F}}\dot{\mathbf{U}} + \mathbf{N}_{\mathcal{F}}\mathbf{U} = \mathbf{F}_{\mathcal{F}} \tag{5.16}
$$

Here $\mathbf{U} = \{\tilde{\mathbf{u}}, \tilde{p_1}, \tilde{p_2}\}$ and $\dot{\mathbf{U}} = \{\tilde{\mathbf{u}}, \tilde{p_1}, \tilde{p_2}\}$ are the vector of nodal unknowns and their time derivatives, respectively. $\tilde{p_1}$ and $\tilde{p_2}$ are the pressures related to the first and

second fluid as shown in Figure 5.3. Subscript $\mathcal{F}$ in Eq. (5.16) refers to the matrices calculated for the fluid medium. Matrix $\mathbf{M}_{\mathcal{F}}$ has the form,

$$\mathbf{M}_{\mathcal{F}} = \begin{pmatrix} \mathbf{M_u} & \tau\,\mathbf{D_1} & \tau\,\mathbf{D_2} \\ \tau\,\mathbf{G_1} & \mathbf{M_{P1}} & \mathbf{0} \\ \tau\,\mathbf{G_2} & \mathbf{0} & \mathbf{M_{P2}} \end{pmatrix} \tag{5.17}$$

$\mathbf{M_u}$, $\mathbf{M_{P1}}$ and $\mathbf{M_{P2}}$ are diagonal lumped mass matrices related to the inertia and pressure rate terms respectively. Note that the terms related to air and water pressures are not directly coupled with each other. If we denote the node indexes with superscripts a and b the components of the arrays involved in (5.17) are,

$$\mathbf{D}_1^{ab} = \mathbf{D}_2^{ab} = \int_\Omega \nabla_x \cdot \mathbf{N}^a\,\mathbf{N}^b\,d\Omega$$

$$\mathbf{G}_1^{ab} = \mathbf{G}_2^{ab} = \int_\Omega \rho c_s^2\,\nabla_x \mathbf{N}^a\,\mathbf{N}^b\,d\Omega.$$

$\mathbf{N}_{\mathcal{F}}$ contains terms related to the nodal values of velocity and pressure and has the form,

$$\mathbf{N}_{\mathcal{F}} = \begin{pmatrix} \tau\,\mathbf{C} & \mathbf{D_1} & \mathbf{D_2} \\ \mathbf{D}^{\mathsf{T}}_{\rho_1 c_1^2} & \tau\,\mathbf{L_1} & \mathbf{0} \\ \mathbf{D}^{\mathsf{T}}_{\rho_2 c_2^2} & \mathbf{0} & \tau\,\mathbf{L_2} \end{pmatrix} \tag{5.18}$$

where,

$$\mathbf{C}^{ab} = \int_\Omega \rho c^2\,\nabla_x \cdot \mathbf{N}^a\,\nabla_x \cdot \mathbf{N}^b\,d\Omega$$

$$\mathbf{D}^{ab}_{\rho_i c_i^2} = \int_\Omega \rho_i c_i^2\,\nabla_x \cdot \mathbf{N}^a\,\mathbf{N}^b\,d\Omega \tag{5.19}$$

$$\mathbf{L}_i^{ab} = \int_\Omega c_i^2\,\nabla_x \mathbf{N}^a\,\nabla_x \mathbf{N}^b\,d\Omega.$$

Subscript i refers to the corresponding fluid domain. Note that all integrals related to the stabilization terms are understood as the sum over all elements. In this sense the sound velocity, c, takes its value at each element in the computation of $\mathbf{C}$ in (5.19).

The last term in Eq. (5.15) is a nonlinear term and as we are going to introduce a predictor/multi-corrector scheme to deal with nonlinearities, the last iteration values, are used to evaluate explicitly this term. Finally we have,

$$\mathbf{F}_{\mathcal{F}} = \begin{pmatrix} \mathbf{0} \\ \tau\,\mathbf{f_1} \\ \tau\,\mathbf{f_2} \end{pmatrix}. \tag{5.20}$$

Here the terms for node a are computed as,

$$\mathbf{f}_i^a = \int_\Omega N^a \left(\Gamma \nabla_x \cdot \mathbf{u}^h \left(\dot{p}_i + \rho_i c_i^2 \nabla_x \cdot \mathbf{u} \right) \right)_j \, d\Omega \tag{5.21}$$

where j refers to the values obtained from the last iteration of the predictor/multi-corrector scheme.

5.3.1.2 *Structure*

Matrices for the shell element can be obtained by recalling Eq. (5.9) as,

$$\int_A \left[\mathbf{B}_m^\mathsf{T} \boldsymbol{\sigma}_m + \mathbf{B}_b^\mathsf{T} \boldsymbol{\sigma}_b \right] \, dA = \int_A \mathbf{N} \, \mathbf{t} \, dA \tag{5.22}$$

here, $\mathbf{B}_m$ and $\mathbf{B}_b$, are membrane and bending strain matrices, respectively. $\mathbf{N}$ is the matrix of linear shape functions for a triangle element.

To be consistent with the matrix form (5.16) presented for the fluid, the following form is introduced for the shell by considering the inertia term,

$$\mathbf{M}_S \dot{\mathbf{U}} + \mathbf{K}_S \mathbf{Y} = \mathbf{f}_S \tag{5.23}$$

where $\mathbf{M}_S$, is the lumped mass matrix for the shell element, $\mathbf{Y}$ is the vector of nodal displacements and $\mathbf{f}_S$ represents external forces. Note that, with an abuse of notation, $\dot{\mathbf{U}}$ in (5.23) contains time derivatives of the displacements (i.e. the velocities) only.

For the elastic behavior, $\mathbf{K}_S$, takes the form

$$\mathbf{K}_S = \int_A \mathbf{B}_m^\mathsf{T} \mathbb{C}_e \mathbf{B}_m \, dA + \int_A \mathbf{B}_b^\mathsf{T} \mathbb{C}_e \mathbf{B}_b \, dA \tag{5.24}$$

Here, $\mathbb{C}_e$, is the constitutive elastic matrix assuming plane stress behavior for the shell, as usual. If plastic behavior of the shell is considered, the internal forces are calculated directly by evaluating the plastic stresses in Eq. (5.22). In this case, $\mathbf{K}_S$ represents the tangent matrix, with material and geometric components, and $\mathbf{K}_S \mathbf{Y}$ represents the internal forces.

5.3.1.3 *Contact*

The contribution of the contact scheme, presented in chapter **??** and Section 5.2.3, to the monolithic FSI scheme is a vector of non-penetrating nodal forces, $\mathbf{F}_e$.

This vector is the assembly of contact forces, $\mathbf{f}_e$, computed at each active contact element. Once the stress field, $\boldsymbol{\sigma}$ in Eq. (5.13), is known inside each active contact element the corresponding internal nodal forces are computed as,

$$\mathbf{f}_e = \int_{\Omega_e} \mathbf{B}_e^\mathsf{T} \boldsymbol{\sigma} \, d\Omega_e \tag{5.25}$$

where $\mathbf{B}_e$ is the generalized strain matrix for the element. Note that once the configuration of the shell is known, the generalized strain field can be calculated inside each contact element.
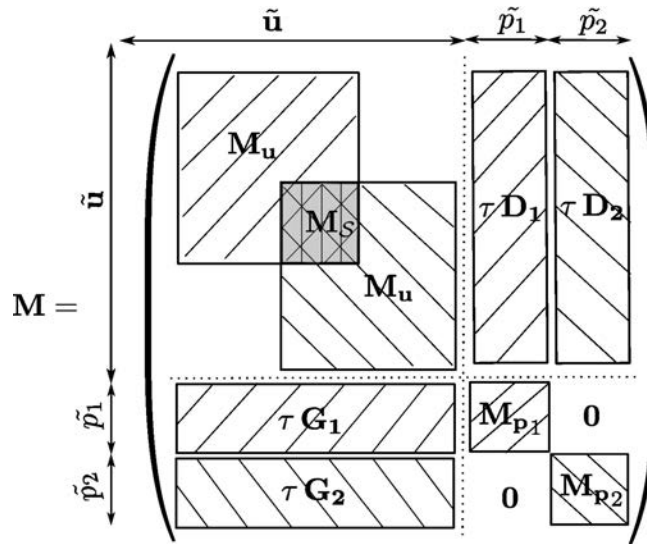
Figure 5.4: Coupled mass matrix. $\mathbf{M}_S$ represents the contribution of the shell element to the coupled system. Note that each domain has its own pressure variables that are duplicated at the interface nodes (Figure 5.3).

5.3.1.4 *FSI predictor/multi-corrector scheme*

Once that all the matrices of the fluid, structure and contact forces are defined, the monolithic FSI system can be written as,

$$\mathbf{M}\dot{\mathbf{U}} + \mathbf{N}\mathbf{U} + \mathbf{K}\mathbf{Y} = \mathbf{F} \tag{5.26}$$

Here $\mathbf{M}$ is the assembly of $\mathbf{M}_{\mathcal{F}}$ and $\mathbf{M}_S$ as defined in Eqs. (5.17) and (5.23), respectively and takes the schematic form shown in Figure 5.4.

Matrix $\mathbf{N}$ only has fluid contributions, Eq. (5.18), and $\mathbf{F}$ is the assembly of fluid, structure and contact forces as introduced in Eqs. (5.20), (5.23) and (5.25).

Note that the term $\mathbf{K}\mathbf{Y}$ only has the contribution from the structure and represents the internal forces. It is obvious that for an elastic behavior of the shell, $\mathbf{K}$ is equivalent to $\mathbf{K}_S$ introduced in (5.23) and $\mathbf{Y}$ is the nodal displacement vector. For an elasto-plastic behavior $\mathbf{K}$ represents the tangent matrix and $\mathbf{K}\mathbf{Y}$ the internal stress forces.

5.3.1.5 *Bossak scheme*

The system of Eqs. (5.26) is integrated in time, from t_n to t_{n+1}, using the Bossak scheme [51, 62] written as,

$$(1 - \alpha)\mathbf{M}\dot{\mathbf{U}}_{n+1} + \alpha\mathbf{M}\dot{\mathbf{U}}_n + \mathbf{N}\mathbf{U}_{n+1} + \mathbf{K}\mathbf{Y}_{n+1} = \mathbf{F} \tag{5.27}$$

Note that terms $\mathbf{M}$, $\mathbf{N}$, $\mathbf{K}$ and $\mathbf{F}$ are calculated in the current configuration, $n + 1$. For the sake of simplicity subscript "$n + 1$" is dropped in these terms. The following

Figure 5.5: Aluminum cylinder filled with air and submerged into the water tank. Sensors are put in 10.16 *cm* from the center of the cylinder.

updates are considered for the accelerations and displacements, as

$$\dot{\mathbf{U}}_{n+1} = \frac{1}{\gamma \Delta t}(\mathbf{U}_{n+1} - \mathbf{U}_n) - \frac{1-\gamma}{\gamma}\dot{\mathbf{U}}_n$$

$$\mathbf{Y}_{n+1} = \mathbf{Y}_n + \Delta t \mathbf{U}_n + \Delta t^2 [\frac{1-2\beta}{2}\dot{\mathbf{U}}_n + \beta \dot{\mathbf{U}}_{n+1}] \tag{5.28}$$

Stability analysis [51] reveals that unconditional stability, second order accuracy and maximal high-frequency dissipation are obtained by choosing the algorithmic parameter α less than or equal to zero ($\alpha \leqslant 0$). γ and β are then computed as,

$$\gamma = \frac{1}{2} - \alpha \qquad \beta = \frac{1}{4}(1-\alpha) \tag{5.29}$$

We choose a residual based predictor/multi-corrector, similar to those proposed in [11] for incompressible flows and in [53] for compressible flows, to handle the nonlinearities embedded in the system of Eqs. (5.27).

The residual, $\mathcal{R}$, at each iteration, i, and in the current step, $n+1$, is defined as,

$$\mathcal{R}_{n+1}^i := \mathbf{M}\dot{\mathbf{U}}_{n+\alpha}^i + \mathbf{N}\mathbf{U}_{n+1}^i + \mathbf{K}\mathbf{Y}_{n+1}^i - \mathbf{F}^i \tag{5.30}$$

The Taylor expansion of the residual, $\mathcal{R}$, around the solution $\mathbf{U}_{n+1}^i$ results in the following incremental system,

$$\mathcal{R}(\dot{\mathbf{U}}_{n+\alpha}^i, \mathbf{U}_{n+1}^i, \mathbf{Y}_{n+1}^i) + \frac{\partial\,\mathcal{R}(\dot{\mathbf{U}}_{n+\alpha}^i, \mathbf{U}_{n+1}^i, \mathbf{Y}_{n+1}^i)}{\partial\,\mathbf{U}_{n+1}^i}\Delta\mathbf{U}_{n+1}^i = \mathbf{0} \tag{5.31}$$

The increments, $\Delta \mathbf{U}_{n+1}^{i}$, are computed at each iteration from (5.31) and the solution is updated;

$$\mathbf{U}_{n+1}^{i+1} = \mathbf{U}_n + \Delta \mathbf{U}_{n+1}^{i}. \tag{5.32}$$

The tangent matrix is evaluated recalling the Bossak update equations for displacements and accelerations, (5.28), and applying the chain rule as,

$$\begin{aligned}
\mathcal{A}_{n+1}^{i} &:= \frac{\partial\, \mathcal{R}_{n+1}^{i}}{\partial\, \mathbf{U}_{n+1}^{i}} = \mathbf{M}\, \frac{\partial\, \dot{\mathbf{U}}_{n+\alpha}^{i}}{\partial\, \mathbf{U}_{n+1}^{i}} + \mathbf{N} + \mathbf{K}\, \frac{\partial\, \mathbf{Y}_{n+1}^{i}}{\partial\, \mathbf{U}_{n+1}^{i}} \\
&= \frac{1-\alpha}{\gamma \Delta t}\, \mathbf{M} + \mathbf{N} + \frac{\Delta t \beta}{\gamma}\, \mathbf{K}
\end{aligned} \tag{5.33}$$

Note that matrix $\mathbf{K}$ represents now the tangent matrix for the shell element. It reduces to $\mathbf{K}_S$, introduced in (5.23), for the elastic behavior of the shell. The tangent matrix includes material and geometric components for the elasto-plastic behavior. The detailed calculation of $\mathbf{K}$ is presented in [34].

Table 5.1 summarizes one step of the residual-based predictor/multi-corrector scheme developed herein. Note that densities are updated at the beginning of each iteration by means of the inverse of a diagonal matrix $\mathbf{V} = [diag(V)]$ containing nodal volumes. V^a, the contribution of a sample node, a, to this diagonal matrix is defined as,

$$V^a = \int_{\Omega} N^a\, d\Omega \tag{5.34}$$

Here N^a is the global shape function corresponding to node a and the integral is computed at the current configuration.

$\mathcal{M}_n$ is a diagonal mass matrix related to step n that its component for a sample node, a, is computed as,

$$\mathcal{M}_n^a = \int_{\Omega_n} \rho^n N^a\, d\Omega_n \tag{5.35}$$

5.3.2 *Explicit time discretization scheme*

In this section we introduce an explicit counterpart for the formulation proposed in Section 5.3.1 using a forward-Euler time discretization scheme. A second order accurate mid-point explicit discretization of the fluid stabilized forms (5.8) and (5.7) was already presented in chapter 3.

5.3.2.1 *Fluid equations*

Recalling definitions for the pressure and velocity subscales as,

$$p' = -\tau\, \mathcal{R}_p^h.$$
$$p^h \mathbf{u}' = -\rho \frac{\partial \epsilon}{\partial p}\Big|_{\rho} \tau(c_s^2) \mathcal{R}_{\mathbf{u}}^h \tag{5.36}$$

Table 5.1: Residual-based implicit predictor/multi-corrector algorithm

Begin *(Time step)*

Predict: $\mathbf{U}_{n+1}^0 = \mathbf{U}_n \Rightarrow$ compute $\dot{\mathbf{U}}_{n+1}^0$ and $\mathbf{Y}_{n+1}^0$

While (err $\leqslant$ tol *or* $i \leqslant i_{max}$)

    Initialize: $\rho_{n+1}^i = \mathbf{V}^{-1}\mathcal{M}_n$ and $c_s^i = \partial p/\partial \rho$

    Build: Evaluate $\mathcal{R}_{n+1}^i$ and $\mathcal{A}_{n+1}^i$,

    Solve: $\Delta\mathbf{U}_{n+1}^i = -\left(\mathcal{A}_{n+1}^i\right)^{-1}\mathcal{R}_{n+1}^i$

    Update: $\mathbf{U}_{n+1}^{i+1} = \mathbf{U}_n^i + \Delta\mathbf{U}_{n+1}^i \Rightarrow \dot{\mathbf{U}}_{n+1}^{i+1}$ & $\mathbf{Y}_{n+1}^{i+1}$

    Finalize: Move particles, $\mathbf{X}_{n+1}^{i+1} = \mathbf{X}_0 + \mathbf{Y}_{n+1}^{i+1}$

End *(Time step)*

the stabilized form of the conservation of momentum and energy, Eqs. (5.14) and (5.15), can be rewritten as,

$$\int_\Omega \mathbf{v}^h \cdot \rho\left(\dot{\mathbf{u}}^h\right) d\Omega - \int_\Omega \nabla_x \cdot \mathbf{v}^h \left(p^h + p'\right) d\Omega = 0 \tag{5.37}$$

$$\int_\Omega q^h \dot{p}^h d\Omega + \int_\Omega q^h \left(\rho c_s^2 + \Gamma p'\right) \nabla_x \cdot \mathbf{u} \, d\Omega$$

$$+ \int_\Omega \Gamma \nabla_x q^h \left(p\mathbf{u}'\right) d\Omega = 0 \tag{5.38}$$

Applying the forward-Euler scheme to the momentum Eq. (5.37) we have,

$$\int_\Omega \mathbf{v}^h \cdot \rho\left(\mathbf{u}_{n+1}^h - \mathbf{u}_n^h\right) d\Omega$$

$$= \Delta t \int_{\Omega_n} \nabla_x \cdot \mathbf{v}^h \left(p^h + p'\right)_n d\Omega \tag{5.39}$$

The matrix form of Eq. (5.39) is written as,

$$\mathbf{M_u}\left(\mathbf{u}_{n+1} - \mathbf{u}_n\right) = \Delta t \left(\mathbf{g}_{\mathcal{F}}\right)_n. \tag{5.40}$$

where $\mathbf{M_u}$ is the same lumped mass matrix introduced in Section 5.3.1.1. The component of vector $\left(\mathbf{g}_{\mathcal{F}}\right)_n$ for node *a* has the form,

$$\left(\mathbf{g}_{\mathcal{F}}\right)_n^a = \int_{\Omega_n} \nabla_x \cdot N^a \left(p^h + p'\right)_n d\Omega \tag{5.41}$$

where N^a is the global shape function corresponding to node a and subscript n refers to the time t_n.
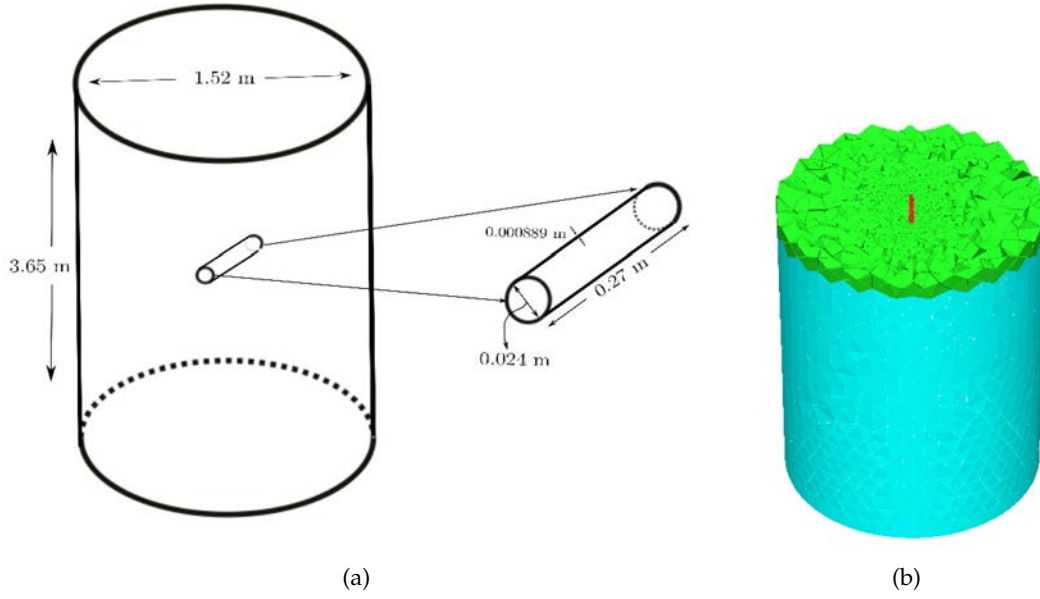
Figure 5.6: Schematic view of the model geometry (a) and mesh configuration at time $t = 0$ (b).

Note that for the interface nodes, $(\mathbf{g}_{\mathcal{F}})_n^a$ has two contributions due to the discontinuous pressure at the interface that are summed up. Discretizing the energy Eq. (5.38) in time we have,

$$\int_\Omega q^h \left(p_{n+1}^h - p_n^h\right) d\Omega = -\Delta t \int_\Omega \Gamma \nabla_x q^h \left(p\, \mathbf{u}'\right)_n d\Omega$$
$$- \Delta t \int_\Omega q^h \left[\left(\rho c_s^2 + \Gamma p'\right) \nabla_x \cdot \mathbf{u}\right]_n d\Omega \qquad (5.42)$$

this results in the matrix equations,

$$\mathbf{M_p}\left(\mathbf{p}_{n+1} - \mathbf{p}_n\right) = \Delta t\, (\mathbf{w}_{\mathcal{F}})_n. \qquad (5.43)$$

where $\mathbf{M_p}$ is an $n_d \times n_d$, n_d is the number of nodes, lumped mass matrix introduced in Section 5.3.1.1. The component related to the node a of the vector $(\mathbf{w}_{\mathcal{F}})_n$ has the form,

$$(\mathbf{w}_{\mathcal{F}})_n^a = -\int_\Omega N^a \left[\left(\rho c_s^2 + \Gamma p'\right) \nabla_x \cdot \mathbf{u}\right]_n d\Omega$$
$$- \int_\Omega \nabla_x N^a \Gamma \left(p\, \mathbf{u}'\right)_n d\Omega \qquad (5.44)$$

We remind that for the interface nodes two pressure forces, $(\mathbf{w}_{\mathcal{F}})_n^a$, are calculated each of which is used to update the corresponding pressure.

5.3.2.2 *Structure and contact*

The explicit time integration of the shell equations is straightforward. In view of Eq. (5.23), the discretized form can be written as,

$$\mathbf{M}_S(\mathbf{U}_{n+1} - \mathbf{U}_n) = \Delta t \left[(\mathbf{f}_S)_n - (\mathbf{K}_S)_n \mathbf{Y}_n\right] \tag{5.45}$$

Note that in contrary to the fluid mass matrix, $\mathbf{M}_{\mathcal{F}}$, that contains off diagonal terms related to the time derivatives of the stabilization terms, the structure mass matrix, $\mathbf{M}_S$, is already lumped and, therefore, can be directly used for the explicit scheme.

Concerning the contact, the only contribution of the contact scheme, presented in Section 5.3.1.3, to the coupled system is the contact forces, $\mathbf{f}_C$. Hence, the only change from implicit to explicit time scheme is that the calculation of these forces is done in the configuration related to t_n instead of t_{n+1}.

5.3.2.3 *Explicit FSI scheme*

One step of the explicit scheme is presented in Table 5.2.

Note that the lumped mass matrix $\mathbf{M}$, used in the velocity update, is constructed by assembling the mass matrices $\mathbf{M_u}$ (for the fluid) and $\mathbf{M}_S$ (for the structure).

At the beginning of each step Δt is chosen as the minimum value computed for all elements. $(\mathbf{F}_S)_n$ in the second step is equal to the $[(\mathbf{f}_S)_n - (\mathbf{K}_S)_n \mathbf{Y}_n]$ as introduced in (5.45). These forces in addition to the fluid momentum residual, $(\mathbf{f}_{\mathcal{F}})_n$ in Eq. (5.41), and contact forces $(\mathbf{f}_C)_n$, are assembled into the global vector $\mathbf{F}_n$. Note that the time derivatives $\dot{\mathbf{u}}_{n+1}$ and $\dot{p}_{n+1}$ are computed to evaluate the pressure and velocity subscales from Eqs. (5.36).

Table 5.2: One step of the explicit scheme

Begin *(Time step)*

Calculate Δt by CFL condition

Assemble: $(\mathbf{f}_{\mathcal{F}})_n$, $(\mathbf{F}_S)_n$ and $(\mathbf{f}_C)_n$ to $\mathbf{F}_n$

Velocity update : $\mathbf{u}_{n+1} = \mathbf{u}_n + \Delta t\,[\mathbf{M}]^{-1}\,\mathbf{F}_n$

Assemble: $(\mathbf{w}_{\mathcal{F}})_n$

Pressure update: $\mathbf{p}_{n+1} = \mathbf{p}_n + \Delta t\,[\mathbf{M_p}]^{-1}\,(\mathbf{w}_{\mathcal{F}})_n$

Position update : $\mathbf{X}_{n+1} = \mathbf{X}_n + \Delta t\,\mathbf{u}_{n+1}$

Volume update : $\mathbf{V}_{n+1} = \mathbf{V}(\mathbf{X}_{n+1})$

Time derivatives update : $\dot{\mathbf{u}}_{n+1}$ and $\dot{p}_{n+1}$

Density update : $\mathbf{J}_{n+1} = [\mathbf{V}_{n+1}]^{-1}\,\mathbf{M_u}$

Sound velocity update : $(c_s)_{n+1} = \partial p_{n+1}/\partial \rho_{n+1}$

End *(Time step)*
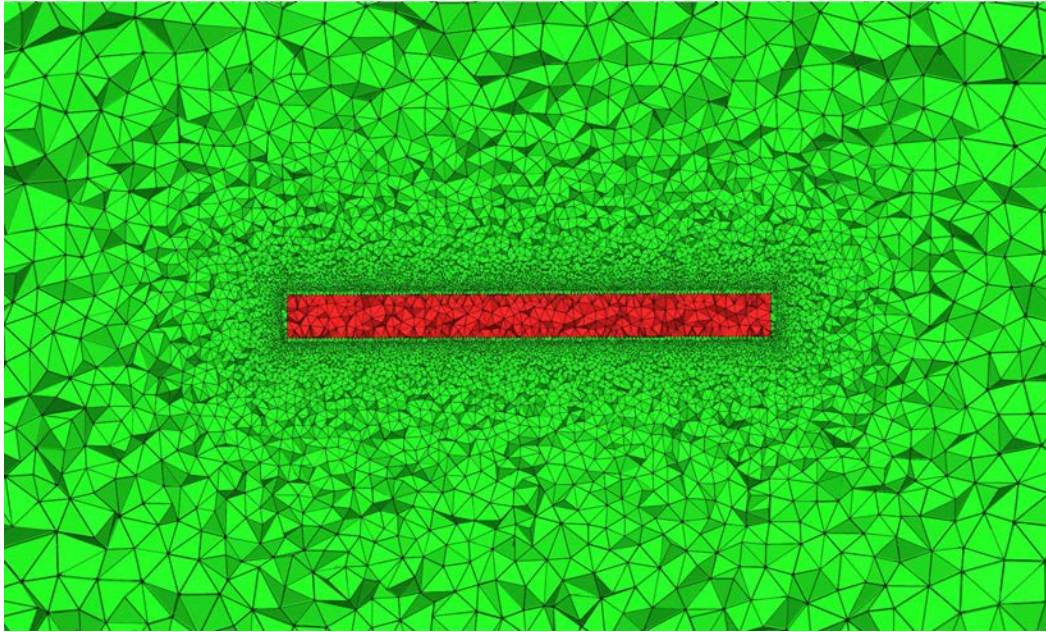
Figure 5.7: Mesh configuration inside and near the cylinder at the beginning of the simulation.

(a)

(b)
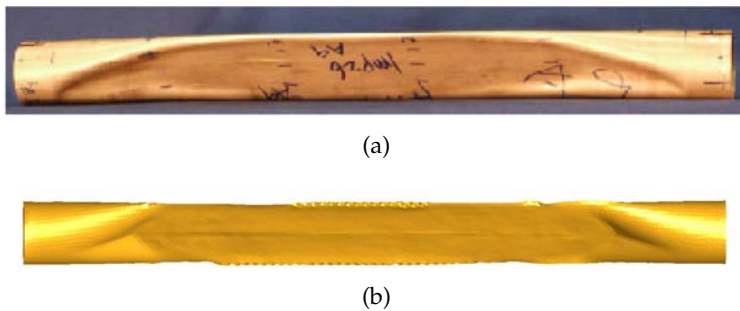
Figure 5.8: Final configuration of cylinder a) experiment, b) simulation

5.4 SOLUTION STRATEGY

Many authors [109, 1, 12, 27] have used a moving Lagrangian frame for solving the hydrodynamic Eqs. (5.1). One of the difficulties in working with moving frames is the large distortion of the FE mesh especially at the interface zones.

In [68] we proposed a compressible framework for the simulation of two-fluid flows that overcomes this problem by regenerating the FE mesh while respecting the interface position. The definition of the interface itself is not straightforward and has consequences on the stability at the interface level [57].

A *nodally perfect matched* interface introduced in [57, 56] for incompressible multi-flows and later developed in [68] for the compressible multi-flows meets the stability requirements at the interface level. This definition is suitable for extension to FSI problems in which the interface, that pass exactly through the nodes and separates fluid domains, is replaced by the structure.

Figure 5.5 depicts an example of a closed cylindrical container submerged into water. The container discretized by shell elements defines the air-water interface. Ad-

vanced mesh moving methods [123, 64, 116, 117] that reduce the frequency of remeshing (i.e. regenerating the mesh) have been developed for FSI computations, including FSI problems with large displacements [116]. For example, FSI computation of parachute clusters with large deformations of the parachutes and with contact between them can be carried out with very few remeshings during the entire computation (see [119]).

In our computations here, due to the extensive nature of the contact we face, we need remeshing, at least in the vicinity of the interface. This is done via utilizing the Tetgen software [114].

In case that a fine mesh near the interface is needed, adaptive mesh generation can be done by assigning volume constrains in the desired zones [114]. As the position of the interface (i.e. structure) is known, a distance function that has its zero on the interface is used to compute the volume constrains at each zone. This technique is tested for 2D multi-flows in [68] to generate a fine mesh near the interface.

The importance of having layers of refined mesh near the fluid-solid interface and maintaining that mesh resolution as the interface moves was recognized as early as in 3D fluid-particle interaction computations reported in [65]. This also motivated the development of the Solid-Extension Mesh Moving Technique [117] for FSI problems in general, where the layers of refined mesh go through minimal deformation as the interface deforms.

In case that large deformations of the shell structure lead to the contact, the contact scheme proposed in Section 5.2.3 is used to compute the contact forces.

Table 5.3 summarizes one step of the FSI scheme. Note that before regenerating the new mesh, nodes in air and water domains that are too close to the interface are marked and deleted to avoid unnecessary local refinement of the mesh.

The new mesh is generated with two constrains: the *first* one is the volume constraint that provides a fine mesh near the structure and the *second* one is a Constrained Delaunay Triangulation to preserve connectivities at the shell surface. Each shell element uses the neighbor elements data to compute the curvature. Therefore, it is more convenient to preserve the connectivities of the shell elements.

In the last step of the mesh regeneration, the new mesh is generated in both air and water and these elements are saved together with the shell elements.

Possible contacts are detected in the following step, as described in Section 5.2.3, by discretizing the closed volume of the cylinder and checking the contact criterion in each contact element. In case that some contact elements are activated, they will be added to the fluid and structure elements to complete the FSI system. The system is then solved using either the implicit or explicit scheme as explained in Sections 5.3.1 and 5.3.2, respectively.

Note that the first and second steps in Table 5.3, that are about generating the new mesh and search for the contact elements, are not necessary at each time step but can be performed every several steps.

5.5   EQUATION OF STATE

Two equations of state (EOS) are used in this simulation. Air is modeled as the perfect gas with $\gamma = 1.4$ and the high pressure water is modeled with Tait equation that is an isentropic stiffened gas EOS.

Table 5.3: One step of the FSI scheme

- **Regenerate Mesh**

  Compute distance and volume constrains

  Mark and delete nodes

  Generate the constrained adaptive mesh

  Merge fluid and shell elements

- **Search for possible contacts**

  Descritize the potential contact volume

  Check the contact criteria

  Save active contact elements

  Merge contact elements into fluid and shell ones

- **Solve FSI system**

  One step of implicit (Table 5.1) or explicit (Table 5.2) solver

The stiffened gas equation is a generalization of the perfect gas equation of state and is written as,

$$(\gamma - 1)\rho\epsilon = p + \gamma\pi \tag{5.46}$$

Here ρ, ϵ and p denote the density, internal energy per unit mass and pressure, respectively and γ and π are constants that need to be specified. This EOS has been used in various applications from gas dynamics to solid. Obviously the constants are chosen to correctly estimate the speed of sound in the medium using this EOS and the definition:

$$c = \sqrt{\left.\frac{\partial p}{\partial \rho}\right|_\eta}$$

where η is the entropy.

To evaluate the sound speed, c, the following thermodynamic expression is first recalled,

$$T d\eta = d\epsilon + p d(\frac{1}{\rho}).$$

Considering the constant entropy and recalling the stiffened gas equation 5.46 it follows that,

$$0 = d\epsilon + pd(\frac{1}{\rho})$$

$$= (\frac{1}{(\gamma-1)\rho})dp - (\frac{p+\gamma\pi}{(\gamma-1)\rho^2})d\rho - (\frac{p}{\rho^2})d\rho$$

$$= (\frac{1}{(\gamma-1)\rho})dp - (\frac{\gamma(\pi+p)}{(\gamma-1)\rho^2})d\rho$$

and the speed of sound in a stiffened gas is given by,

$$c = \sqrt{\left.\frac{\partial p}{\partial \rho}\right|_\eta} = \sqrt{\frac{\gamma(\pi+p)}{\rho}}.$$

In case of water the following values for the constant are found,

$$\pi = 6.0 \times 10^8 \, Pa \quad \gamma \in \{4.4, 5.5, 7.0\}$$

Note that for $\pi = 0$ the stiffened gas equation simplifies to the perfect gas equation.

The Tait equation of state,

$$p = \eta + \alpha\rho^\beta$$

models water as a compressible barotropic medium. In contrary to the perfect gas EOS, here, pressure is just a function of density. η, α and β are three constants that can be determined from the initial state of the material and by the fact that the bulk modulus of a fluid, K, is an affine function of pressure determined by two constants k_1 and k_2. Hence,

$$k_1 + k_2 p = K = \rho\frac{dp}{d\rho} = \beta\alpha\rho^\beta = \beta(p-\eta),$$

which gives

$$\eta = -\frac{k_1}{k_2} \quad \beta = k_2.$$

Furthermore, writing $p_0 = p(\rho_0)$ gives,

$$\alpha = \frac{p_0 + \frac{k_1}{k_2}}{\rho_0^{k_2}}$$

In the literature, the following values are found for water,

$$k_1 = 2.07 \times 10^9 \, \frac{kg}{m^3 s^2} \quad k_2 = 7.15$$

In this case the speed of sound is computed as,

$$c = \sqrt{\left.\frac{\partial p}{\partial \rho}\right|_\eta} = \sqrt{\frac{(k_2 p_0 + k_1)}{\rho_0}\left(\frac{\rho}{\rho_0}\right)^{k_2-1}}.$$

For the initial values of our implosion model, $\rho = 1000$ and $p_0 = 10^6$ Pa, the predicted speed of sound is,

$$c_0 = c(\rho_0) = \sqrt{\frac{(k_2 p_0 + k_1)}{\rho_0}} = 1441.23 \ \frac{m}{s}$$

It can be easily shown that Tait EOS corresponds to the particular case of an *isentropic* stiffened gas. It differs from the ideal gas EOS in one important aspect. Since it involves only pressure and density but not energy, the Tait EOS is barotropic. This closes the Euler equations but decouples the energy equation from the mass and momentum equations, so that simulations may be carried out with only the mass and momentum equations. However there is no harm in also solving the energy equation, which is done in this work.

5.6 UNDERWATER IMPLOSION OF CYLINDRICAL CONTAINER

The underwater implosion of a cylindrical tube is considered in this section. The tube is made of aluminum and has a diameter, $D = 2.4 \ cm$, length, $L = 27 \ cm$, and thickness, $t = 8.89 \times 10^{-2} \ cm$. It is filled with air at the atmospheric pressure, $p_a = 101.3 \ KPa$, is closed at both ends and then submerged in a water tank.

The tank is rigid and has a diameter, $D = 1.5 \ m$, and length, $L = 3.65 \ m$. Figures 5.5 and 5.6a show the experiment setup and the schematic view of the test, respectively. Pressure sensors are placed at a radial distance, $d = 10.16 \ cm$, from the center of the tube (Figure 5.5). The aluminum cylinder is maintained at the center of the tank by a set of rigid bars attached to the tank. Water pressure inside the tank is atmospheric at the beginning and the initial velocity is zero everywhere.

Hydrostatic loading is accomplished by activating a water pump to slowly raise the water pressure. Following the experiment the aluminum cylinder collapses flat, but does not crack open, when the external pressure reaches $p_w = 6.99 \ Mpa$.

Figure 5.8a and Figure 5.8b show the collapsed view of the cylinder at the end of the experiment and the simulation, respectively.

The time histories of pressure captured by the sensors reveal a drop of roughly 1.2 *MPa* in water pressure after 0.6 *ms* from the beginning of the experiment. This drop reaches its maximum just before contact occurs and is followed by an instant pressure increase of around 1.1 *MPa* as the result of the first contact. The main signature of the pressure time history captured in the sensors appears as a pressure peak that varies between 9.6 *Mpa* and 10.3 *MPa* at $t = 6.5 \ ms$. The pressure then starts to fluctuate around the initial value (Figure 5.9).

The full model was considered for simulating this experiment (Figure 5.6b). The aluminum cylinder is assumed to have elasto-plastic behavior with a Young modulus $E = 68.9 \ GPa$, a Poisson ratio $\nu = 0.3$, a density $\rho = 2700 \ kg/m^3$ and a yield stress $\sigma_Y = 275 \ MPa$. As no crack appears in the final collapsed tube in the experiment, no
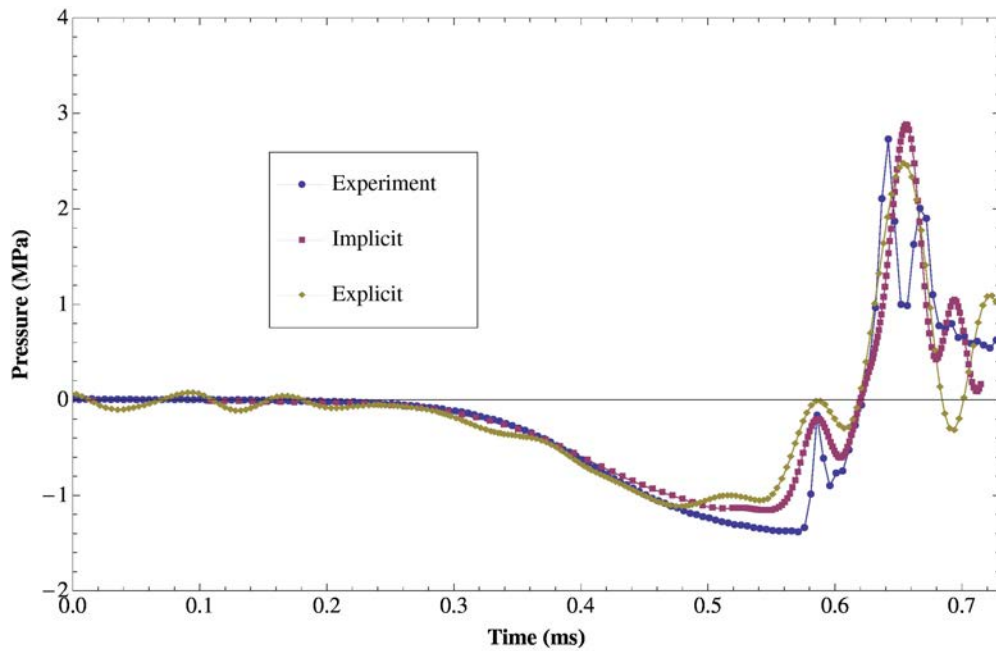
Figure 5.9: Time history of pressure in one of the sensors compared with implicit and explicit results. Zero pressure corresponds to the initial pressure of *6.99 MPA*.

rupture model is considered here. The tube is discretized by 24000 three-noded EBST shell elements (Figure 5.11a).

The contact algorithm is the one presented and tested along with the EBST element in chapter **??**. *Potential contact elements* that descritize the contact domain inside the cylinder are shown in Figure 5.11b at time t = 0.7ms during the contact phase. Among these elements, those that satisfy the contact criterion and therefore are activated, *active contact elements*, are shown in Figure 5.11c at the same instance.

The geometrical properties of the cylinder, the L/D ratio, and the final collapsed shape of the tube, Figure 5.8a, suggest a second mode collapse and therefore the initial geometry of the tube is perturbed as,

$$r = r_0 \left(1 - 0.01 \, \text{Cos}(2\theta)\right)$$

Here (r, θ) is the cylindrical coordinate of a point on the section of the cylinder and a perturbation equal to 1% of the initial radius, r_0, is considered.

The air inside the cylinder is discretized using an initial mesh of 100000 four-noded tetrahedra (Figure 5.7). 3.5 million tetrahedra are used to discretize the external water (Figure 5.6b).

The initial state of the air inside the cylinder is set to $\rho = 1 \, \text{kg/m}^3$ and $p = 101.3$ *KPa* at rest. For the external water we have $\rho = 1000 \, \text{kg/m}^3$ and the initial pressure is set to the value at which the collapse starts at the experiment ($p = 6.99 \, MPa$).

Figure 5.10 reports the evolution of an horizontal cut along the cylinder and a vertical cut at the mid section, from the beginning till the end of the simulation when the cylinder is completely collapsed. Note that contact occurs at the speed of 60 *m/s* and takes 0.1 *ms* from the first contact until the cylinder totally collapses.
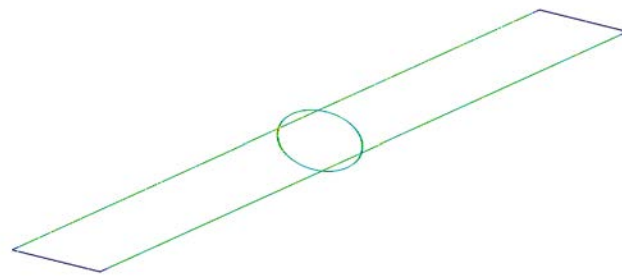
(a) 0.05 ms
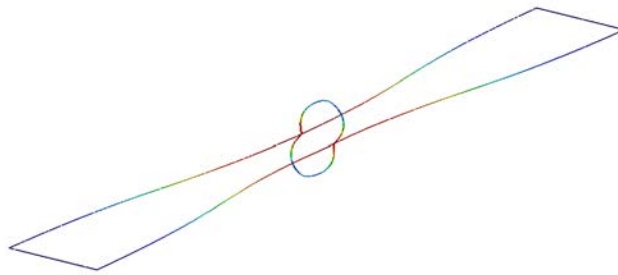
(b) 0.45 ms
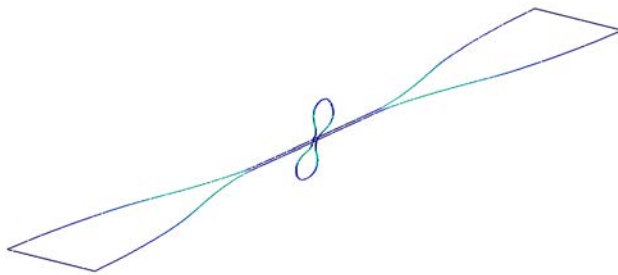
(c) 0.65 ms
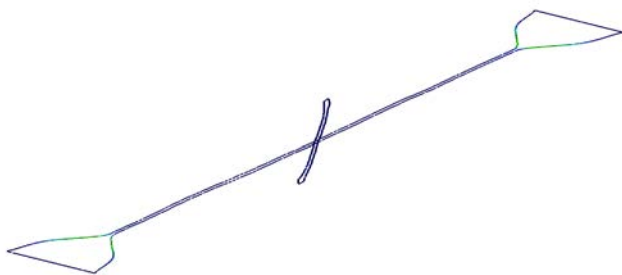
(d) 0.8 ms

Figure 5.10: Collapse of the cylinder visualized through the evolution of the cut planes.
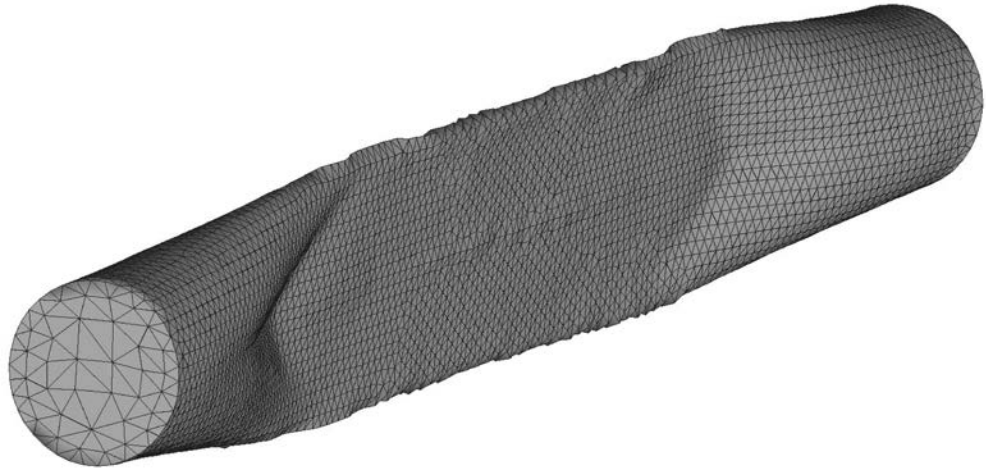
(a)
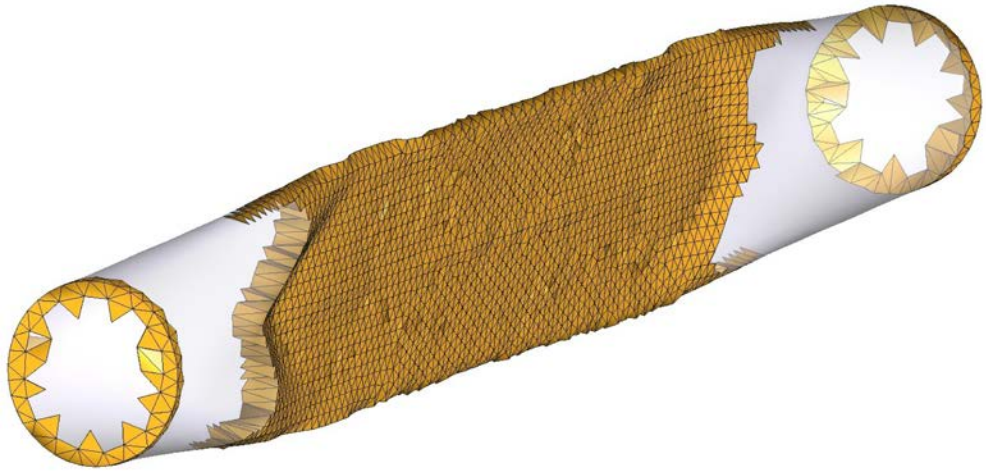
(b)

(c)

Figure 5.11: Mesh configuration of cylinder (a), *potential contact elements* (b) and *active contact elements* (c).

The time history of pressure, for the implicit and explicit time schemes, in one of the sensors is compared with its experimental measured counterpart in Figure 5.9. The overall signature of the pressure pulse including an initial drop in pressure followed by two pressure peaks as the result of contact is captured by the numerical simulation. More accurate results are obtained for the implicit solution due to the second order time scheme and the more intrinsic robustness of the implicit scheme. Numerical diffusion deteriorates somehow the sharpness of the pressure peaks, though peak values are captured well.

The time step for the implicit solver varies from 8.0×10^{-6} seconds for the first 0.3 *ms* of the simulation to 6.0×10^{-8} seconds during the contact. For the implicit solver the convergence is achieved approximately after 5 iterations. Each iteration of the implicit solver takes 1250 seconds.

For the explicit solver, on the other hand, a *CFL* = 0.5 leads to a time step of approximately 1.2×10^{-8} seconds. For each time step the "solve" module, that is practically a loop over elements and nodes, takes t = 8.7 seconds.

Large displacements of the mesh in the vicinity and inside the tube (Figures 5.12 and 5.8b) lead to regenerating the mesh. In this way a refined and undistorted mesh, as the one shown in Figure 5.7, at time t = 0.0, and Figure 5.12, at time t = 0.8ms, is guaranteed during the simulation.

Remeshing consists of saving the connectivities of the shell elements and creating a constrained tetrahedralization of the air and water domains that respects the shell connectivities. A distance function that has its zero on the tube is used to provide fine discretization near the tube. This function has the same form as the one proposed in chapter 3 for the implosion of cylindrical bubbles. It simply provides different level of resolution around the cylinder in order to provide a smooth transition form the fine mesh near the structure to the coarse one at the far zones.

Although the "build" and "solve" modules of the code are done in parallel, *remeshing* is a serial operation and needs to be avoided, as much as possible, to take the maximum benefits of the parallel computing. For the mentioned number of elements it takes 175 seconds to regenerate the mesh.

Here for the first phase, before collapse when the time step is large, *remeshing* is done at each step considering its relative small cost compared to the "solve" module. However, as the time step decreases remeshing is done at each 10 or 20 steps. It is observed that as the number of elements increase, the time efficiency improves by solving the first phase of the simulation, precisely before the collapse is initiated, using the implicit solver, while the rest of it, by the explicit solver.

5.7 CONCLUSIONS

The underwater implosion of a cylindrical cylinder has been successfully modeled using a fully Lagrangian monolithic FSI framework. Internal air and external water are modeled as compressible media and the shock hydrodynamics system of equations for both cases are stabilized using a variational multi-scale finite method. A free-rotation shell triangle, EBST, that best suited our monolithic FSI system along with a contact scheme based on the contact domain method [84] has been used to model the aluminum cylinder during the collapse. A detailed description of the matrices involved in the construction of the system are provided for two implicit and
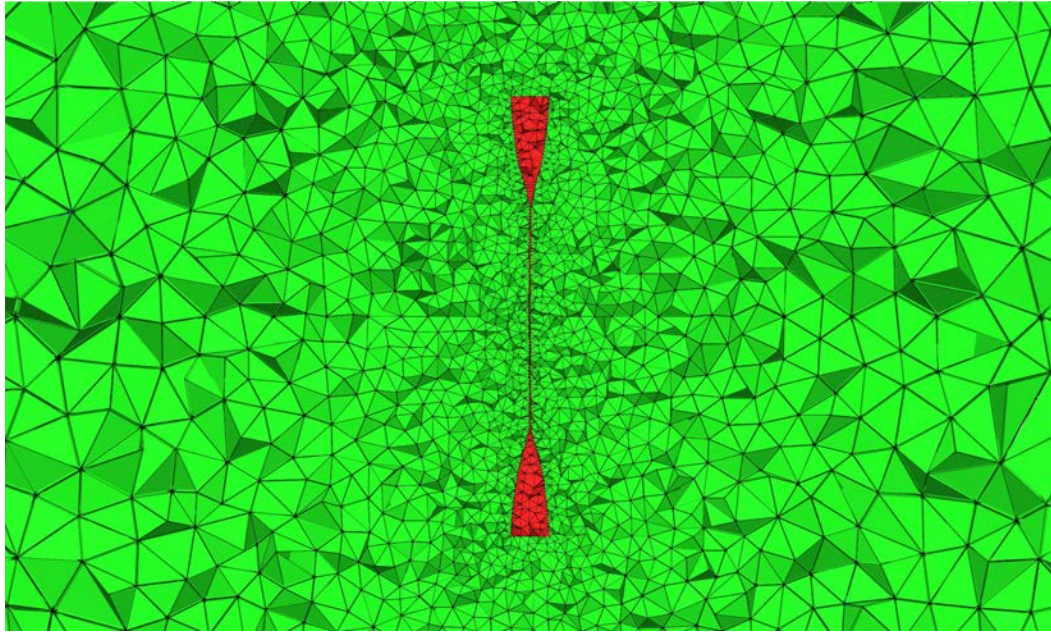
Figure 5.12: A view of the refined mesh near the cylinder at the final stage of the collapse.

explicit time integration schemes. Except for some elongation that can be seen in the time history of pressure during contact, both implicit and explicit results are quite successful in capturing the signature of the collapse and the pressure peak. A predictable superiority can be observed in the implicit solution due to its second-order accuracy. An important advantage of our method is to provide a refined and undistorted mesh configuration during the simulation. This is, however, quite costly, due to the unavailability of parallel mesh generators, especially at the final stage of the collapse when the time steps are reduced by several orders of magnitude. A more detailed study of the time consumption reveals that the favored scheme to solve this kind of problems with a large number of elements is to use an implicit time integration scheme at the beginning of the solution and before the initialization of the contact, and then switch to the explicit time integration scheme during the collapse phase. In this way, as the time needed for the build and solve of the system is greater than the remeshing time, it is convenient to remesh at each step. Then by switching to the explicit scheme and reducing significantly the build and update time, the remeshing can be performed once at each 10 or 20 steps, considering small deformations during each explicit step.

Future works in this field will focus, from one hand, on the study of the interaction between the shock waves and the nearby structures, and from the other hand, on the improvement of the time efficiency of the method by local regeneration of the mesh, instead of the global one, and on parallelization of the mesh generation module.

6

CONCLUSIONS AND FUTURE WORK

In this section we provide a summary of the achievements of this work and an outlook of the future work.

Conclusions

Concerning the main motivation of this work that is the simulation of underwater implosion of cylindrical cylinder, we first developped a compressible Lagrangian framework " a la PFEM" to simulate the multi-fluid compressible problems. To this end, we have taken advantage of a variationally stabilized form of the Euler equations proposed by Scovazzi and an interface tracking method proposed by Idelsohn. The extension to the multi-fluid modeling was then obtained by *discontinuous* treatment of the kinetic variables i.e. pressure, density at the interface , from one side, and interface-connectivity-preserving remeshing, from the other side. A geometrical adaptive mesh generation was added to our framework in order to provide enough resolution at the interface level.

At this point we tested our framework to simulate the underwater implosion of large, *cm* size, cylindrical bubble. Beside obtaining the essential signatures of the bubble dynamics, we have captured for the first time, up to our knowledge, the detailed generation of shape and surface instabilities for this size bubbles.

To later expand the mentioned framework for FSI problems, a new shell-to-shell contact method has been developed. This method belongs to the category of the contact domain methods and exploits the fact that shell's kinematics is described by the motion of its mid plane. Therefore, contact is detected as soon as the mid-planes reach a distance equivalent to the sum of the half-thicknesses of the contacting structures. Basing on this we discretize, by the Delaunay approach, the volume enclosed between the contacting surfaces (that will be guaranteed to have non-zero thickness). Such "virtual volume" is treated as elastic, with a suitably defined assumed strain, in all the areas in which the two shells are actually in contact.

A monolithic coupling between the shell structure, cylinder, the compressible air inside the cylinder and the compressible water outside it, has been considered to model the underwater implosion of an aluminum cylinder. The coupled system has been solved by an implicit second-order predictor multi-corrector scheme. Mesh quality is guaranteed during the simulaion by regenerating the mesh. An explicit forward Euler solution of this system is also provided. Both results, explicit and implicit ones, have been compared to experimental data and good agreement has been obtained.

A more detailed study of the time consumption reveals that the favored strategy to solve this kind of problems, with a large number of elements, is to use an implicit time integration scheme at the beginning of the simulation and before the initialization of

the contact, and then switch to the explicit one for the collapse phase.

Future work

One of the main advantages of the Lagrangian framework proposed, compared to the Eulerian ones [31] is its intrinsic property of regenerating the mesh at the presence of large deformations. This benefit is obtained at the cost of the *serial* process of remeshing that is quite time consuming compared to the rest of the code modules that are implemented for parallel computing. Therefore, for this specific class of applications for which the deformations are restricted to specific zones, a *local* remeshing process in which just the mesh in the vicinity of the large movement zones are regenerated, is suitable. Of course, a parallel remeshing technique, if available, is always a recommended alternative.

In view of above comments, the following developments can be performed for each of the sections of this thesis.

1. The compressible hydrocode can be improved by considering higher order elements instead of the actual simple elements in case that more resolution is needed at the shock zones.

2. The interface following technique for multi-fluids [57, 25] is just developed for 2D cases. The extension of this method to 3D is inevitable for real simulations of multi-fluid problems.

3. The structure is considered uncracked during the simulation, while in some implosion experiments cracks are initiated during the collapse phase. Apart from the crack simulation, the instantaneous mixture of high pressure air and water requires a more delicate treatment.

Considering the applications of the analysis framework proposed in this thesis, two different lines of research can be considered for future research work.

1. The interaction between the shock wave, produced by implosion of a single bubble or multiple bubbles, and the nearby objects can be of interest in various applications [20, 72, 96].

2. It is known that the high pressures produced at the final stage of collapse, specially for smaller bubbles of μm size, leads to excessively high temperatures i.e. some thousands of Kelvin [77]. Modeling of this effect requires more complex EOS's and also to consider the possible phase change effect. In this way, the analysis framework proposed in this thesis can be improved for the real modeling of acoustic cavitation and phenomena like SL (sonoluminescence) [138] or sonochemistry [118].

BIBLIOGRAPHY

[1] AJ Barlow. A compatible finite element multi-material ale hydrodynamics algorithm. *International Journal for Numerical Methods in Fluids*, 56(8):953–964, 2008. (Cited on pages 25 and 105.)

[2] T. Belytschko, Y.Y. Lu, and L. Gu. Element-free galerkin methods. *International journal for numerical methods in engineering*, 37(2):229–256, 1994. (Cited on page 18.)

[3] DJ Benson, Y. Bazilevs, MC Hsu, and TJR Hughes. Isogeometric shell analysis: the reissner-mindlin shell. *Computer Methods in Applied Mechanics and Engineering*, 199(5-8):276–289, 2010. (Cited on pages xvi, 85, and 86.)

[4] J. Hallquist G. Goudreau D. Benson. Sliding interfaces with contact-impact in large-scale lagrangian computations. *Comput. Methods Appl. Mech. Engrg.*, 51:107–137, 1985. (Cited on page 65.)

[5] C. Bernardi, N. Debit, and Y. Maday. Coupling finite element and spectral methods- First results. *mathematics of computation*, 54(189):21–39, 1990. (Cited on page 65.)

[6] G. Birkhoff. Note on taylor instability. *Quart. Appl. Math*, 12:306–309, 1954. (Cited on page 14.)

[7] V.A. Bogoyavlenskiy. Single-bubble sonoluminescence: Shape stability analysis of collapse dynamics in a semianalytical approach. *Physical Review E*, 62(2):2158, 2000. (Cited on pages 23, 24, 63, and 89.)

[8] J. Bonet and S. Kulasegaram. Correction and stabilization of smooth particle hydrodynamics methods with applications in metal forming simulations. *International Journal for Numerical Methods in Engineering*, 47(6):1189–1214, 2000. (Cited on page 18.)

[9] C.E. Brennen. *Cavitation and bubble dynamics*, volume 44. Oxford University Press, USA, 1995. (Cited on pages xiii, 1, 9, 12, 13, 15, 17, 23, and 89.)

[10] M.P. Brenner, S. Hilgenfeldt, D. Lohse, and R.R. Rosales. Acoustic energy storage in single bubble sonoluminescence. *Physical review letters*, 77(16):3467–3470, 1996. (Cited on page 59.)

[11] AN Brook and TJ Hughes. R. streamline upwind/petrov-galerkin formulations for convection dominated flows with particular emphasis on the incompressible navier-stokes equation. *Comp. Meth. Appl. Mech. Eng*, 32:199–259, 1982. (Cited on page 100.)

[12] J.C. Campbell and M.J. Shashkov. A compatible lagrangian hydrodynamics algorithm for unstructured grids. 2000. (Cited on pages 41 and 105.)

[13] EJ Caramana and MJ Shashkov. Elimination of artificial grid distortion and hourglass-type motions by means of lagrangian subzonal masses and pressures. *Journal of Computational Physics*, 142(2):521–561, 1998. (Cited on page 25.)

[14] J.M. Carbonell, E. Oñate, and B. Suárez. Modeling of ground excavation with the particle finite-element method. *Journal of engineering mechanics*, 136:455, 2010. (Cited on page 65.)

[15] R.P.R. Cardoso, J.W. Yoon, J.J. Grácio, F. Barlat, and J. Cesar de Sa. Development of a one point quadrature shell element for nonlinear applications with contact and anisotropy. *Computer methods in applied mechanics and engineering*, 191(45):5177–5206, 2002. (Cited on pages xv, 82, 83, and 84.)

[16] GL Chahine, KM Kalumuck, and R. Duraiswami. Fluid-structure interaction simulation of bubble dynamics by coupling fluid bem and structural fem codes. *ASME FLUIDS ENG DIV PUBL FED, ASME, NEW YORK, NY,(USA), 1993,*, 176:39–50, 1993. (Cited on page 90.)

[17] J. Chessa and T. Belytschko. An enriched finite element method and level sets for axisymmetric two-phase flow with surface tension. *International Journal for Numerical Methods in Engineering*, 58(13):2041–2064, 2003. (Cited on page 41.)

[18] R. Codina. Finite element approximation of the hyperbolic wave equation in mixed form. *Computer Methods in Applied Mechanics and Engineering*, 197(13):1305–1322, 2008. (Cited on pages 32 and 35.)

[19] AH Coppola-Owen and R. Codina. Improving eulerian two-phase flow finite element approximation with discontinuous gradient pressure shape functions. *International journal for numerical methods in fluids*, 49(12):1287–1304, 2005. (Cited on page 41.)

[20] JJ Cor and TF Miller. Theoretical analysis of hydrostatic implodable volumes with solid inner structures. *Journal of Fluids and Structures*, 25(2):284–303, 2009. (Cited on page 116.)

[21] JJ Cor and TF Miller. Theoretical analysis of hydrostatic implodable cylindrical volumes with solid inner structures. *Journal of Fluids and Structures*, 26(2):253–273, 2010. (Cited on page 90.)

[22] MA Crisfield. Re-visiting the contact patch test. *International Journal for Numerical Methods in Engineering*, 48(3):435–449, 2000. (Cited on page 77.)

[23] P. Dadvand, R. Rossi, M. Gil, X. Martorell, J. Cotela, E. Juanpere, S.R. Idelsohn, and E. Oñate. Migration of a generic multi-physics framework to hpc environments. *Computers and fluids*, 2012. (Cited on page 7.)

[24] P. Dadvand, R. Rossi, and E. Oñate. An object-oriented environment for developing finite element codes for multi-disciplinary applications. *Archives of computational methods in engineering*, 17(3):253–297, 2010. (Cited on page 7.)

[25] M. De Mier Torrecilla et al. *Numerical simulation of multi-fluid flows with the Particle Finite Element Method*. PhD thesis, Universitat Politècnica de Catalunya, 2010. (Cited on pages v, vi, xiii, 7, 20, 41, 42, 43, and 116.)

[26] G.A. Dilts. Moving-least-squares-particle hydrodynamicsâi. consistency and stability. *International Journal for Numerical Methods in Engineering*, 44(8):1115–1155, 1999. (Cited on page 18.)

[27] VA Dobrev, TE Ellis, T.V. Kolev, and RN Rieben. Curvilinear finite elements for lagrangian hydrodynamics. *International Journal for Numerical Methods in Fluids*, 65(11-12):1295–1310, 2011. (Cited on pages 25, 41, and 105.)

[28] S. R. Idelsohn M. A. Celigueta R. Rossi E. Oñate and Salvador Latorre. Possibilities of the particle finite element method in computational mechanics. *Computer Methods in Mechanics*, pages 271–310, 2010. (Cited on page 65.)

[29] H. Edelsbrunner and E.P. Mücke. Three-dimensional alpha shapes. In *Proceedings of the 1992 workshop on Volume visualization*, pages 75–82. ACM, 1992. (Cited on page 20.)

[30] N. El-Abbasi and K.J. Bathe. Stability and patch test performance of contact discretizations and a new solution algorithm. *Computers & Structures*, 79(16):1473–1486, 2001. (Cited on page 65.)

[31] C. Farhat, A. Rallu, and S. Shankaran. A higher-order generalized ghost fluid method for the poor for the three-dimensional two-phase flow computation of underwater implosions. *Journal of Computational Physics*, 227(16):7674–7700, 2008. (Cited on pages 24, 51, 58, 59, 90, and 116.)

[32] C. Farhat, A. Rallu, K. Wang, and T. Belytschko. Robust and provably second-order explicit–explicit and implicit–explicit staggered time-integrators for highly non-linear compressible fluid–structure interaction problems. *International Journal for Numerical Methods in Engineering*, 84(1):73–107, 2010. (Cited on pages 90 and 95.)

[33] D.J. Flannigan, S.D. Hopkins, C.G. Camara, S.J. Putterman, and K.S. Suslick. Measurement of pressure and density inside a single sonoluminescing bubble. *Physical review letters*, 96(20):204301, 2006. (Cited on pages xiii, 2, and 3.)

[34] F.G. Flores and E. Onate. Improvements in the membrane behaviour of the three node rotation-free bst shell triangle using an assumed strain approach. *Computer methods in applied mechanics and engineering*, 194(6-8):907–932, 2005. (Cited on pages 75, 76, 92, and 101.)

[35] F.G. Flores and E. Oñate. Rotation-free finite element for the non-linear analysis of beams and axisymmetric shells. *Computer methods in applied mechanics and engineering*, 195(41-43):5297–5315, 2006. (Cited on pages 90 and 92.)

[36] GID. the personal pre and postprocessor. *www.gidhome.com*, 11, 2012. (Cited on page 7.)

[37] F.R. Gilmore. The growth or collapse of a spherical bubble in a viscous compressible liquid. 1952. (Cited on pages xiii, 15, and 16.)

[38] R.A. Gingold and J.J. Monaghan. Smoothed particle hydrodynamics-theory and application to non-spherical stars. *Monthly Notices of the Royal Astronomical Society*, 181:375–389, 1977. (Cited on page 18.)

[39] NK Gupta, N. Mohamed Sheriff, and R. Velmurugan. Experimental and numerical investigations into collapse behaviour of thin spherical shells under drop hammer impact. *International journal of solids and structures*, 44(10):3136–3155, 2007. (Cited on pages xv, 80, and 81.)

[40] J.R. Haines, BW Riemer, D.K. Felde, J.D. Hunn, S.J. Pawel, and C.C. Tsai. Summary of cavitation erosion investigations for the sns mercury target. *Journal of Nuclear Materials*, 343(1):58–69, 2005. (Cited on page 2.)

[41] S. Hartmann, J. Oliver, R. Weyler, JC Cante, and JA Hernández. A contact domain method for large deformation frictional contact problems. part 2: Numerical aspects. *Computer Methods in Applied Mechanics and Engineering*, 198(33-36):2607–2631, 2009. (Cited on page 65.)

[42] G. Hauke and T.J.R. Hughes. A comparative study of different sets of variables for solving compressible and incompressible flows. *Computer methods in applied mechanics and engineering*, 153(1-2):1–44, 1998. (Cited on page 32.)

[43] G.J. Heard, M. McDonald, NR Chapman, and L. Jaschke. Underwater light bulb implosions: A useful acoustic source. In *OCEANS'97. MTS/IEEE Conference Proceedings*, volume 2, pages 755–762. IEEE, 1997. (Cited on page 90.)

[44] P. Heintz and P. Hansbo. Stabilized Lagrange multiplier methods for bilateral elastic contact with friction. *Computer methods in applied mechanics and engineering*, 195(33-36):4323–4333, 2006. (Cited on pages 65 and 66.)

[45] C. Herring. *Theory of the pulsations of the gas bubble produced by an underwater explosion*. Columbia Univ., Div. of National Defense Research, 1941. (Cited on pages xiii, 15, 16, and 23.)

[46] R. Hickling and M.S. Plesset. Collapse and rebound of a spherical bubble in water. *Physics of Fluids*, 7:7, 1964. (Cited on pages xiii, 16, 17, and 23.)

[47] P. Hild. Numerical implementation of two nonconforming finite element methods for unilateral contact. *Computer Methods in Applied Mechanics and Engineering*, 184(1):99–123, 2000. (Cited on page 65.)

[48] S. Hilgenfeldt, M.P. Brenner, S. Grossmann, and D. Lohse. Analysis of rayleigh–plesset dynamics for sonoluminescing bubbles. *Journal of fluid mechanics*, 365(1):171–204, 1998. (Cited on pages 23 and 89.)

[49] S. Hueber and B.I. Wohlmuth. A primal-dual active set strategy for non-linear multibody contact problems. *Computer Methods in Applied Mechanics and Engineering*, 194(27-29):3147–3166, 2005. (Cited on page 65.)

[50] T.J.R. Hughes. Multiscale phenomena: Green's functions, the dirichlet-to-neumann formulation, subgrid scale models, bubbles and the origins of stabilized methods. *Computer methods in applied mechanics and engineering*, 127(1-4):387–401, 1995. (Cited on pages 30 and 31.)

[51] T.J.R. Hughes. *The finite element method: linear static and dynamic finite element analysis*, volume 65. Dover Publications, 2000. (Cited on pages 99 and 100.)

[52] T.J.R. Hughes, G.R. Feijóo, L. Mazzei, and J.B. Quincy. The variational multiscale method–a paradigm for computational mechanics. *Computer methods in applied mechanics and engineering*, 166(1-2):3–24, 1998. (Cited on pages 30 and 31.)

[53] T.J.R. Hughes and TE Tezduyar. Finite element methods for first-order hyperbolic systems with particular emphasis on the compressible euler equations. *Computer Methods in Applied Mechanics and Engineering*, 45(1-3):217–284, 1984. (Cited on pages 35 and 100.)

[54] S. Iakovlev. Submerged fluid-filled cylindrical shell subjected to a shock wave: fluid–structure interaction effects. *Journal of fluids and structures*, 23(1):117–142, 2007. (Cited on page 90.)

[55] S. Idelsohn, N. Nigro, A. Limache, and E. Oñate. Large time-step explicit integration method for solving problems with dominant convection. *Computer Methods in Applied Mechanics and Engineering*, 2012. (Cited on page 18.)

[56] S.R. Idelsohn, M. Mier-Torrecilla, N. Nigro, and E. Oñate. On the analysis of heterogeneous fluids with jumps in the viscosity using a discontinuous pressure field. *Computational Mechanics*, 46(1):115–124, 2010. (Cited on pages 23, 25, 40, 41, 46, and 105.)

[57] S.R. Idelsohn, M. Mier-Torrecilla, and E. Oñate. Multi-fluid flows with the particle finite element method. *Computer Methods in Applied Mechanics and Engineering*, 198(33-36):2750–2767, 2009. (Cited on pages v, vi, 7, 23, 25, 40, 41, 46, 90, 95, 105, and 116.)

[58] S.R. Idelsohn, E. Onate, N. Calvo, and F. Del Pin. The meshless finite element method. *International Journal for Numerical Methods in Engineering*, 58(6):893–912, 2003. (Cited on page 18.)

[59] S.R. Idelsohn, E. Oñate, and F.D. Pin. The particle finite element method: a powerful tool to solve incompressible flows with free-surfaces and breaking waves. *International Journal for Numerical Methods in Engineering*, 61(7):964–989, 2004. (Cited on pages 25, 41, 65, and 89.)

[60] Idelsohn, SR and Del Pin, F. and Rossi, R. and Oñate, E. Fluid–structure interaction problems with strong added-mass effect. *International journal for numerical methods in engineering*, 80(10):1261–1294, 2009. (Cited on page 95.)

[61] RD Ivany and F.G. Hammitt. Cavitation bubble collapse in viscous, compressible liquidsânumerical analysis. *Journal of Basic Engineering*, 87:977, 1965. (Cited on page 16.)

[62] K.E. Jansen, C.H. Whiting, and G.M. Hulbert. A generalized α method for integrating the filtered navier–stokes equations with a stabilized finite element method. *Computer Methods in Applied Mechanics and Engineering*, 190(3):305–319, 2000. (Cited on page 99.)

[63] E. Johnsen and T. Colonius. Numerical simulations of non-spherical bubble collapse. *Journal of fluid mechanics*, 629(1):231–262, 2009. (Cited on pages xiii, 4, and 5.)

[64] A.A. Johnson and T.E. Tezduyar. Mesh update strategies in parallel finite element computations of flow problems with moving boundaries and interfaces. *Computer Methods in Applied Mechanics and Engineering*, 119(1-2):73–94, 1994. (Cited on page 106.)

[65] AA Johnson and TE Tezduyar. 3d simulation of fluid-particle interactions with the number of particles reaching 100. *Computer Methods in Applied Mechanics and Engineering*, 145(3):301–321, 1997. (Cited on page 106.)

[66] J.R. Kamm. Evaluation of the sedov-von neumann-taylor blast wave solution. *Astrophys. J. Suppl.(submitted)*, 2000. (Cited on pages 46 and 49.)

[67] K. Kamran, R. Rossi, and E. Oñate. A contact algorithm for shell problems via the particle finite element method (pfem). *Computational Mechanics*, 10.1007/s00466-012-0791-x, 2012. (Cited on pages 65 and 95.)

[68] K. Kamran, R. Rossi, E. Oñate, and S.R. Idelsohn. A compressible lagrangian framework for the simulation of the underwater implosion of large air bubbles. *Computer Methods in Applied Mechanics and Engineering*, 225:210–225, 2013. (Cited on pages 23, 35, 105, and 106.)

[69] J.B. Keller and I.I. Kolodner. Damping of underwater explosion bubble oscillations. *Journal of applied physics*, 27(10):1152–1161, 1956. (Cited on pages 16 and 23.)

[70] E. Klaseboer, BC Khoo, and KC Hung. Dynamics of an oscillating bubble near a floating structure. *Journal of Fluids and Structures*, 21(4):395–412, 2005. (Cited on page 90.)

[71] G.J. Le Beau, SE Ray, SK Aliabadi, and TE Tezduyar. Supg finite element computation of compressible flows with the entropy and conservation variables formulations. *Computer Methods in Applied Mechanics and Engineering*, 104(3):397–422, 1993. (Cited on page 35.)

[72] SC Li. *Cavitation of hydraulic machinery*, volume 277. Imperial College Press, 2000. (Cited on pages 1 and 116.)

[73] D. Lohse. Cavitation hots up. *Nature*, 434(7029):33–34, 2005. (Cited on pages xiii and 3.)

[74] J.F.M. Manual. Vol. 5, partiii. *Quality Maintenance, Submarine Maintenance Engineering, US Navy, Portsmouth, NH*, 2006. (Cited on page 89.)

[75] B.E. McDonald and C. Holland. Decay of large underwater bubble oscillations. *The Journal of the Acoustical Society of America*, 107:3084, 2000. (Cited on pages 24 and 89.)

[76] R. Menikoff and B.J. Plohr. The riemann problem for fluid flow of real materials. *Reviews of modern physics*, 61(1):75, 1989. (Cited on pages 27, 29, and 96.)

[77] S. Nagrath, K. Jansen, R.T. Lahey, et al. Hydrodynamic simulation of air bubble implosion using a level set approach. *Journal of Computational Physics*, 215(1):98–132, 2006. (Cited on pages 23, 24, 59, 62, 89, and 116.)

[78] US Navy. The navy unmanned undersea vehicle (uuv) master plan. *US Navy, November*, 9, 2004. (Cited on page 90.)

[79] B. Nayroles, G. Touzot, and P. Villon. Generalizing the finite element method: diffuse approximation and diffuse elements. *Computational mechanics*, 10(5):307–318, 1992. (Cited on page 18.)

[80] J. Nitsche. Uber ein variationsprinzip zur losung von dirichlet-problemen bei verwendung von teilraumen, die keinen randbedingungen unterworfen sind. In *Abhandlungen aus dem Mathematischen Seminar der Universitat Hamburg*, volume 36, pages 9–15. Springer, 1971. (Cited on page 65.)

[81] WF Noh. Errors for calculations of strong shocks using an artificial viscosity and an artificial heat flux. *Journal of Computational Physics*, 72(1):78–120, 1987. (Cited on pages 46 and 47.)

[82] B.E. Noltingk and E.A. Neppiras. Cavitation produced by ultrasonics. *Proceedings of the Physical Society. Section B*, 63:674, 1950. (Cited on page 12.)

[83] J.T. Oden and L. Demkowicz. *Applied functional analysis*. Chapman & Hall/CRC, 2009. (Cited on page 31.)

[84] J. Oliver, S. Hartmann, JC Cante, R. Weyler, and JA Hernández. A contact domain method for large deformation frictional contact problems. Part 1: Theoretical basis. *Computer Methods in Applied Mechanics and Engineering*, 198(33-36):2591–2606, 2009. (Cited on pages 65 and 113.)

[85] E. Oñate. Derivation of stabilized equations for numerical solution of advective-diffusive transport and fluid flow problems. *Computer Methods in Applied Mechanics and Engineering*, 151(1-2):233–265, 1998. (Cited on page 32.)

[86] E. Oñate. Possibilities of finite calculus in computational mechanics. *International journal for numerical methods in engineering*, 60(1):255–281, 2004. (Cited on page 32.)

[87] E. Oñate, M.A. Celigueta, S.R. Idelsohn, F. Salazar, and B. Suárez. Possibilities of the particle finite element method for fluid–soil–structure interaction problems. *Computational Mechanics*, pages 1–12, 2011. (Cited on page 65.)

[88] E. Onate and M. Cervera. Derivation of thin plate bending elements with one degree of freedom per node: a simple three node triangle. *Engineering Computations: Int J for Computer-Aided Engineering*, 10(6):543–561, 1993. (Cited on page 76.)

[89] E. Onate and F.G. Flores. Advances in the formulation of the rotation-free basic shell triangle. *Computer methods in applied mechanics and engineering*, 194(21-24):2406–2443, 2005. (Cited on pages 75, 76, and 92.)

[90] E. Onate, S. Idelsohn, OC Zienkiewicz, and RL Taylor. A finite point method in computational mechanics. applications to convective transport and fluid flow. *International Journal for Numerical Methods in Engineering*, 39(22):3839–3866, 1996. (Cited on page 18.)

[91] E. Oñate, S.R. Idelsohn, M.A. Celigueta, and R. Rossi. Advances in the particle finite element method for the analysis of fluid–multibody interaction and bed erosion in free surface flows. *Computer Methods in Applied Mechanics and Engineering*, 197(19):1777–1800, 2008. (Cited on page 65.)

[92] E. Oñate, S.R. Idelsohn, F. Del Pin, and R. Aubry. The particle finite element method. an overview. *International Journal of Computational Methods*, 1(2):267–307, 2004. (Cited on pages xiii, 19, 25, 41, 65, and 89.)

[93] E. Onate and F. Zarate. Rotation-free triangular plate and shell elements. *International Journal for Numerical Methods in Engineering*, 47(1-3):557–603, 2000. (Cited on pages 75 and 76.)

[94] M. Orr and M. Schoenberg. Acoustic signatures from deep water implosions of spherical cavities. *The Journal of the Acoustical Society of America*, 59:1155, 1976. (Cited on pages 24, 89, and 90.)

[95] M. Packer, W.J. Fishkind, I.H. Fine, B.S. Seibel, and R.S. Hoffman. The physics of phaco: a review. *Journal of Cataract & Refractive Surgery*, 31(2):424–431, 2005. (Cited on page 3.)

[96] M.S. Pearle. Shock-wave lithotripsy for renal calculi. *New England Journal of Medicine*, 367(1):50–57, 2012. (Cited on pages xiii, 4, and 116.)

[97] M.S. Plesset. The dynamics of cavitation bubbles. *ASME J. Appl.Mech.*, 16:228–231, 1949. (Cited on page 11.)

[98] MS Plesset and TP Mitchell. On the stability of the spherical shape of a vapor cavity in a liquid. Technical report, DTIC Document, 1954. (Cited on pages 14 and 62.)

[99] M.S. Plesset and A. Prosperetti. Bubble dynamics and cavitation. *Annual Review of Fluid Mechanics*, 9(1):145–185, 1977. (Cited on pages 24, 62, and 89.)

[100] H. Poritsky. The collapse or growth of a spherical bubble or cavity in a viscous fluid. *Proc. First Nat. Cong. in Appl. Math*, pages 813–821, 1952. (Cited on page 12.)

[101] A. Prosperetti and A. Lezzi. Bubble dynamics in a compressible liquid. part 1. first-order theory. *J. FLUID MECH., 1986*, 168:457–478, 1986. (Cited on pages 16, 23, and 89.)

[102] L. Rayleigh. On the pressure developed in a liquid during the collapse of a spherical cavity. *Phil. Mag*, 34(200):94–98, 1917. (Cited on pages 11, 23, and 89.)

[103] AB Reynolds and G. Berthoud. Analysis of excobulle two-phase expansion tests. *Nuclear Engineering and Design*, 67(1):83–100, 1981. (Cited on page 15.)

[104] W.J. Rider. Revisiting wall heating. *Journal of Computational Physics*, 162(2):395–410, 2000. (Cited on page 48.)

[105] Rossi, R. and Oñate, E. Analysis of some partitioned algorithms for fluid-structure interaction. *Engineering Computations: Int J for Computer-Aided Engineering*, 27(1):20–56, 2010. (Cited on page 95.)

[106] Ryzhakov, PB and Rossi, R. and Idelsohn, SR and Oñate, E. A monolithic Lagrangian approach for fluid–structure interaction problems. *Computational Mechanics*, 46(6):883–899, 2010. (Cited on page 95.)

[107] S. Sathe and T.E. Tezduyar. Modeling of fluid–structure interactions with the space–time finite elements: contact problems. *Computational Mechanics*, 43(1):51–60, 2008. (Cited on page 95.)

[108] A.J.R. Schneider. *Some compressibility effects in cavitation bubble dynamics*. PhD thesis, California Institute of Technology, 1949. (Cited on pages xiii, 15, and 16.)

[109] G. Scovazzi, JN Shadid, E. Love, and WJ Rider. A conservative nodal variational multiscale method for lagrangian shock hydrodynamics. *Computer Methods in Applied Mechanics and Engineering*, 2010. (Cited on pages v, 7, 23, 25, 27, 33, 34, 35, 36, 37, 41, 96, and 105.)

[110] L.I. Sedov. *Similarity and dimensional methods in mechanics*. CRC, 1993. (Cited on pages 46 and 49.)

[111] S.B. Segletes. Thermodynamic stability of the mie–grüneisen equation of state, and its relevance to hydrocode computations. *Journal of applied physics*, 70(5):2489–2499, 1991. (Cited on page 27.)

[112] J.R. Shewchuk. Delaunay refinement algorithms for triangular mesh generation. *Computational geometry*, 22(1):21–74, 2002. (Cited on page 44.)

[113] K.M. Shyue. A fluid-mixture type algorithm for compressible multicomponent flow with mie–grüneisen equation of state. *Journal of Computational Physics*, 171(2):678–707, 2001. (Cited on page 27.)

[114] H. Si. Tetgen: A quality tetrahedral mesh generator and a 3d delaunay triangulator. *Weierstrass Institute for Applied Analysis and Stochastics, available from http://tetgen. berlios. de Haber, E., Ascher, UM, Aruliah, DM, & Oldenberg, D*, pages 150–171, 2000. (Cited on pages 69, 73, and 106.)

[115] K.Kamran R.Rossi S.Idelsohn and E.Oñate. Underwater implosion using the particle finite element method. *CIMNE research report*, PI-371, 2012. (Cited on pages 59, 74, 84, and 89.)

[116] K. Stein, T. Tezduyar, and R. Benney. Mesh moving techniques for fluid-structure interactions with large displacements. *Journal of Applied Mechanics*, 70:58, 2003. (Cited on page 106.)

[117] K. Stein, T.E. Tezduyar, and R. Benney. Automatic mesh update with the solid-extension mesh moving technique. *Computer Methods in Applied Mechanics and Engineering*, 193(21):2019–2032, 2004. (Cited on page 106.)

[118] K.S. Suslick. Sonochemistry. *Science*, 247(4949):1439–1445, 1990. (Cited on pages 3 and 116.)

[119] K. Takizawa, T. Spielman, and T.E. Tezduyar. Space–time fsi modeling and dynamical analysis of spacecraft parachutes and parachute clusters. *Computational Mechanics*, pages 1–20, 2011. (Cited on pages 95 and 106.)

[120] K. Takizawa and T.E. Tezduyar. Computational methods for parachute fluid–structure interactions. *Archives of computational methods in engineering*, 19(1):125–169, 2012. (Cited on page 95.)

[121] M. Tanguay. *Computation of bubbly cavitating flow in shock wave lithotripsy*. California Institute of Technology, 2005. (Cited on page 4.)

[122] M. Senga T.E. Tezduyar and D. Vicker. Computation of inviscid supersonic flows around cylinders and spheres with the supg formulation and yzβ shock-capturing. *Computational Mechanics*, 38:469–481, 2006. (Cited on page 35.)

[123] T. Tezduyar, S. Aliabadi, M. Behr, A. Johnson, and S. Mittal. Parallel finite-element computation of 3d flows. *Computer*, 26(10):27–36, 1993. (Cited on page 106.)

[124] T.E. Tezduyar, S. Sathe, T. Cragin, B. Nanna, B.S. Conklin, J. Pausewang, and M. Schwaab. Modelling of fluid–structure interactions with the space–time finite elements: Arterial fluid mechanics. *International Journal for Numerical Methods in Fluids*, 54(6-8):901–922, 2007. (Cited on page 95.)

[125] T.E. Tezduyar, S. Sathe, R. Keedy, and K. Stein. Space–time finite element techniques for computation of fluid–structure interactions. *Computer Methods in Applied Mechanics and Engineering*, 195(17):2002–2027, 2006. (Cited on page 95.)

[126] T.E. Tezduyar and M. Senga. Stabilization and shock-capturing parameters in supg formulation of compressible flows. *Computer methods in applied mechanics and engineering*, 195(13):1621–1632, 2006. (Cited on page 35.)

[127] T.E. Tezduyar and M. Senga. Supg finite element computation of inviscid supersonic flows with yzβ shock-capturing. *Computers & fluids*, 36(1):147–159, 2007. (Cited on page 35.)

[128] N. TS500-AU-SPN. Us navy general specification for the design, construction, and repair of diving and hyperbaric equipment revision 1 august 23, 2006. 2006. (Cited on page 5.)

[129] S.E. Turner. Underwater implosion of glass spheres. *The Journal of the Acoustical Society of America*, 121:844, 2007. (Cited on pages 24, 47, 58, 59, and 90.)

[130] DP Updike. On the large deformation of a rigid plastic spherical shell compressed by a rigid plate. *Journal of Engineering for Industry*, 94(3):949–955, 1972. (Cited on page 81.)

[131] J. VonNeumann and RD Richtmyer. A method for the numerical calculation of hydrodynamic shocks. *Journal of Applied Physics*, 21(3):232–237, 1950. (Cited on page 36.)

[132] GM Ward and DI Pullin. A study of planar richtmyer-meshkov instability in fluids with mie-grüneisen equations of state. *Physics of Fluids*, 23:076101, 2011. (Cited on page 27.)

[133] A.B. Wardlaw Jr and J.A. Luton. Fluid-structure interaction mechanisms for close-in explosions. *Shock and Vibration*, 7(5):265–275, 2000. (Cited on page 5.)

[134] P. Wriggers and G. Zavarise. *Computational contact mechanics*. Wiley Online Library, 2004. (Cited on page 65.)

[135] CC Wu and P.H. Roberts. Shock-wave propagation in a sonoluminescing gas bubble. *Physical review letters*, 70(22):3424–3427, 1993. (Cited on page 59.)

[136] X. Xi and P. Zhong. Dynamic photoelastic study of the transient stress field in solids during shock wave lithotripsy. *The Journal of the Acoustical Society of America*, 109:1226, 2001. (Cited on page 4.)

[137] A.P. Yoganathan, Z. He, and S. Casey Jones. Fluid mechanics of heart valves. *Annu. Rev. Biomed. Eng.*, 6:331–362, 2004. (Cited on page 2.)

[138] F.R. Young. *Sonoluminescence*. CRC press, 2004. (Cited on pages 63 and 116.)

[139] Z.H. Zhong. *Finite element procedures for contact-impact problems*, volume 7. Oxford University Press, 1993. (Cited on page 83.)

[140] S. Zhu, F.H. Cocks, G.M. Preminger, and P. Zhong. The role of stress waves and cavitation in stone comminution in shock wave lithotripsy. *Ultrasound in medicine & biology*, 28(5):661–671, 2002. (Cited on page 4.)

[141] Z. Zong. A hydroplastic analysis of a free–free beam floating on water subjected to an underwater bubble. *Journal of fluids and structures*, 20(3):359–372, 2005. (Cited on page 90.)